
**Structural, chemical, and magnetic
investigation of a
graphene/cobalt/platinum multilayer
system on silicon carbide**

—

**About the formation of magnetic structures in 2D cobalt
layers**

Dissertation

submitted in partial fulfillment of the requirements
for the degree of

doctor rerum naturalium

(Dr. rer. nat.)

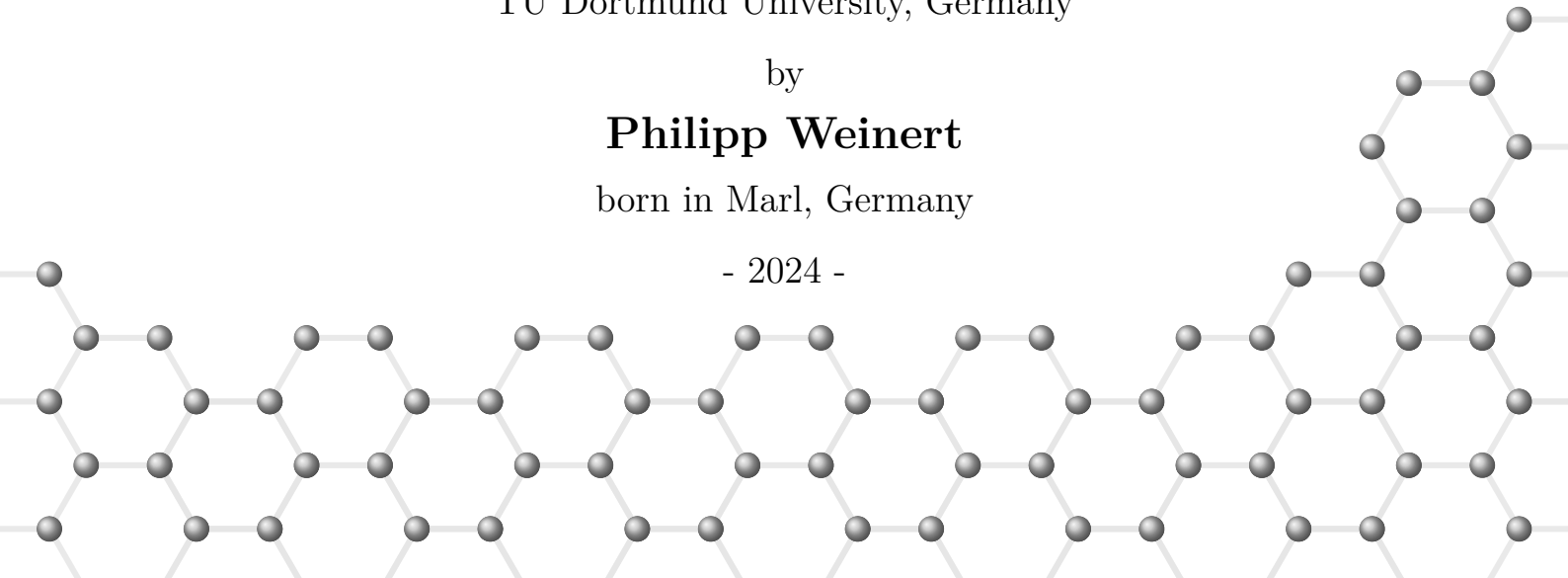
of the Department of Physics
TU Dortmund University, Germany

by

Philipp Weinert

born in Marl, Germany

- 2024 -



A dissertation submitted to the department of physics of TU Dortmund University
in partial fulfillment of the requirements for the degree of doctor of science.

First corrector:	Prof. Dr. Carsten Westphal
Second corrector:	Prof. Dr. Dr. Wolfgang Rhode
Head of commission:	Prof. Dr. Marc Aßmann
Representative of scientific staff:	Dr. Gerald Schmidt
Date of submission:	30.01.2024
Date of disputation:	15.03.2024

Abstract

Spintronics offers huge potential for data storage and processing and, thus, for overcoming the challenges arising from the ever-increasing demands in the field of electronics. To fully utilize this potential in real-world applications, appropriate materials are required. Graphene-ferromagnetic interfaces show great promise in this context. Combining graphene with a ferromagnet, such as cobalt, results in a system with many advantageous effects, such as Dzyaloshinskii–Moriya interaction (DMI). These effects allow for the formation of useful spin structures with high stability. Furthermore, such structures can also be induced in cobalt by combining it with a heavy non-magnetic metal such as platinum.

In this study, the magnetic interlayer coupling and domain structure of ultra-thin ferromagnetic cobalt (Co) layers embedded between a graphene (G) layer and a platinum (Pt) layer on a silicon carbide (SiC) substrate (G/Co/Pt on SiC) were investigated. The $(6\sqrt{3} \times 6\sqrt{3})$ R30°-reconstruction was prepared on SiC and served as a precursor for graphene. It was prepared using two techniques, namely confinement controlled sublimation (CCS) and polymer assisted sublimation growth (PASG). Consequently, the sample properties varied slightly. Following this, the metal layers were prepared by intercalation.

Experimentally, a combination of x-ray photoemission electron microscopy (X-PEEM) with x-ray magnetic circular dichroism (XMCD) was carried out at the Co L-edge to study the system's magnetic structure. Furthermore, structural and chemical properties of the system were investigated using low-energy electron diffraction (LEED) and x-ray photoelectron spectroscopy (XPS). *In-situ* LEED patterns revealed the crystalline structure of each layer within the system. Moreover, XPS confirmed the presence of quasi-freestanding graphene and the absence of cobalt silicide. These characteristics of a clean and homogeneous Co-layer provide an excellent foundation for magnetic features to form. The magnetic structure of all samples exhibited numerous spin vortices and anti-vortices. In spintronics, these can be used as data carriers. The general magnetic structure of the material is heavily influenced by the preparation method. Different aspects were identified, which enhance or impede the formation of vortices. [1]

Kurzfassung

Die Spintronik bietet enormes Potenzial im Bereich der Datenspeicherung und -verarbeitung und zur Überwindung der immer weiter steigenden Anforderungen im Bereich der Elektronik. Um dieses Potenzial zu nutzen, werden geeignete Materialien benötigt. Diesbezüglich sind Graphen-Ferromagnet-Grenzschichten besonders vielversprechend. Wird Graphen mit einem Ferromagneten, wie Kobalt, kombiniert, ergibt sich ein System mit vielen vorteilhaften Eigenschaften, wie Dzyaloshinskii–Moriya Wechselwirkung (DMI). Diese ermöglichen die Bildung von stabilen, nützlichen Spin-Strukturen. Solche Strukturen können ebenfalls in Kobalt hervorgerufen werden, wenn es mit einem schweren, nicht magnetischen Metall, wie Platin, in Verbindung steht.

In dieser Arbeit wurde die magnetische Grenzschicht-Kopplung und Domänenstruktur von ultradünnen ferromagnetischen Kobaltschichten zwischen Graphen und Platinschichten auf einem Siliziumcarbidsubstrat (SiC) untersucht. Die $(6\sqrt{3} \times 6\sqrt{3})$ R30°-Rekonstruktion von SiC diente als Vorstufe für Graphen. Sie wurde mit zwei Methoden präpariert, der Raumbegrenzten-Sublimation (CCS) und der Polymere-unterstützten Sublimation (PASG). Diese führten zu leicht verschiedenen Probeneigenschaften. Anschließend wurden die Metallschichten mittels Interkalation präpariert.

Die magnetische Struktur des Systems wurde mittels Synchrotronstrahlung angeregter Photoemissions-Elektronenmikroskopie (X-PEEM) an der Kobalt-L-Kante unter Nutzung des zirkularen magnetischen Röntgendiffraktionsmikroskops (XMCD) untersucht. Strukturelle Eigenschaften wurden mittels niederenergetischer Elektronenbeugung (LEED) und chemische mittels Röntgen-Photoelektronenspektroskopie (XPS) analysiert. *In-situ* LEED-Messungen zeigten die kristalline Struktur jeder Schicht im System. Mittels XPS wurde quasi-freistehendes Graphen und die Abwesenheit von Kobaltsiliziden nachgewiesen. Die somit reine und homogene Kobaltschicht bildet eine hervorragende Grundlage für die Ausbildung von Spin-Strukturen. Die magnetische Struktur aller Proben zeigte eine Vielzahl von Spinwirbeln und -antiwirbeln. In der Spintronik können diese als Datenträger genutzt werden. Die generelle magnetische Struktur wurde stark von der verwendeten Präparationsmethode beeinflusst. Verschiedene Aspekte wurden entdeckt, die die Bildung von Spinwirbeln begünstigen oder erschweren. [1]

Chapter

Contents

Contents	vii
1 Introduction	1
2 Background	5
2.1 Graphene: Introduction and preparation	5
2.1.1 Discovery, Structure, and Properties	5
2.1.2 Silicon Carbide: Composition and Structure	7
2.1.3 Graphene on Silicon Carbide: Growth and Properties	8
2.1.4 Intercalation of Graphene on Silicon Carbide	10
2.2 Magnetism: Fundamentals and structures	11
2.2.1 Spontaneous magnetization	11
2.2.2 Band model of ferromagnetism	12
2.2.3 Magnetic Domains	13
2.2.4 Magnetic Anisotropy	14
2.2.5 Magnetic skyrmions	15
3 Theoretical background	19
3.1 Fundamentals	19
3.1.1 Inelastic Mean Free Path of electrons in solids	19
3.1.2 The Photoelectric Effect	21
3.2 Photoelectron spectroscopy (PES)	23
3.3 Photoemission electron microscopy (PEEM)	31
3.3.1 Excitation with ultraviolet light	31
3.3.2 Excitation with synchrotron radiation	33
3.4 Low-energy electron diffraction (LEED)	38

4	Experimental setup	41
4.1	Ultra-high vacuum (UHV)	41
4.2	Setups for the silicon carbide preparation	42
4.3	Analytic equipment	45
4.3.1	UV-PEEM at TU Dortmund	45
4.3.2	XPS setup at DELTA	49
4.3.3	X-PEEM setup at BESSY II	52
5	Sample Preparation	55
5.1	Silicon carbide preparation	55
5.2	Sample coating and intercalation	57
6	Results and Discussion	59
6.1	Ultraviolet photoemission electron microscopy	60
6.2	Low-energy electron diffraction	62
6.3	X-ray photoelectron spectroscopy	66
6.3.1	Carbon 1s signal	67
6.3.2	Silicon 2p signal	70
6.3.3	Platinum 4f single	73
6.3.4	Carbon 3p signal	75
6.3.5	Summary	77
6.4	X-ray photoemission electron microscopy	78
6.4.1	Data processing	78
6.4.2	Magnetic structure of the embedded Co-layers	82
6.4.3	Out-of-plane magnetization	90
6.4.4	Summary	94
7	Conclusion	97
A	XPS fit parameters	101
A.1	Carbon 1s	101
A.2	Silicon 2p	104
A.3	Platinum 4f	107
A.4	Cobalt 3p	109

B Solution to the equation system used to calculate the surface magnetization components using X-PEEM data	111
C Overview of the X-PEEM images	117
Bibliography	121
Publications	143
Acknowledgments	145

List of Acronyms

ARPES	Angle-resolved photoelectron spectroscopy	28
BESSY II	Berliner Elektronenspeicherring-Gesellschaft für Synchrotronstrahlung (Berlin, Germany)	54
BL11	Beamline 11 at DELTA	51
CCS	Confinement controlled sublimation	9
CEM	Channel electron multiplier	53
DELTA	Dortmunder Elektronen-Speicherring-Anlage (Dortmund, Germany)	51
DMI	Dzyaloshinskii–Moriya interactions	2, 18
HEA	Hemispherical energy analyzer	52
IMFP	Inelastic mean free path	19
LEED	Low-energy electron diffraction	4, 39
PASG	Polymer assisted sublimation growth	9
PEEM	Photoemission electron microscopy	4, 31
PES	Photoelectron spectroscopy	22
PMA	Perpendicular magnetic anisotropy	2, 14
SOC	Spin-orbit coupling	26

List of Acronyms

U55	Undulator 55 of DELTA	51
UHV	Ultra-high vacuum	2, 43
UPS	Ultraviolet photoelectron spectroscopy	25
UV-PEEM	Ultraviolet photoemission electron microscopy	4, 31
X-PEEM	X-ray photoemission electron microscopy	4, 33
XAS	X-ray absorption spectrum	34
XMCD	X-ray magnetic circular dichroism	4, 35
XPS	X-ray photoelectron spectroscopy	4, 25

List of Symbols

α	Asymmetry parameter	26
c	Winding type of a skyrmion	15
χ^{2*}	Reduced chi-squared	30
$d_{\text{ef.}}$	Effective escape depth	28
Δ	Exchange splitting	12
ΔE	Energy resolution of the hemispherical energy analyzer	53
E_{bin}	Binding energy	22
E_{Fermi}	Fermi energy, Fermi edge, Fermi level	12
E_{vac}	Vacuum level of a solid	22
E_{kin}	Kinetic energy	19
E_{p}	Plasmon energy	19
E_{pass}	Pass energy of the hemispherical energy analyzer	53
E_{SOC}	Spin-orbit splitting	27
γ	Helicity of a skyrmion	16
h	Planck constant	22
$h\nu$	Photon energy: Planck constant times frequency of light	22
I_{edge}	PEEM intensity taken at an absorption edge	34

$I^-(E)$	PEEM intensity taken with light with negative helicity	36
$I^+(E)$	PEEM intensity taken with light with positive helicity	36
I_{pre}	PEEM intensity taken a few eV below an absorption edge	34
I_{XMCD}	XMCD or asymmetry intensity	36
λ	Inelastic mean free path IMFP	19
j	Total angular momentum quantum number	27
\mathbf{k}	Wavevector	36
l	Orbital angular momentum number	26
λ_{Brog}	De Broglie wavelength	38
\mathbf{m}	Sample magnetization direction (at the Surface)	35
m_{\parallel}	In-plane component of the local surface magnetization	37
m_{\perp}	Out-of-plane component of the local surface magnetization	37
μ_{B}	Bohr magneton	11
n	Principle quantum number	26
N_{A}	Avogadro constant	20
N_{Sk}	Topological charge of a skyrmion	15
p	Out-of-plane magnetization direction of a skyrmion host	15
P_{circ}	Degree of circular polarization	36
ϕ	Azimuthal angle of sample rotation around its surface normal	37
Φ	Work funktion	22
ϕ_{p}	Position vector of a skyrmion	16

$\rho_{\mathbf{md}}$	Magnetization density	15
s	Spin	26
T_C	Curie temperature	11
Θ	PES emission angle/polar angle regarding the surface normal	28
Θ_{HEA}	Acceptance angle of the hemispherical energy analyzer	52
Θ_{mpa}	In-plane magnetization polar angle of a skyrmion	16

List of Figures

1.1	Sketch of the G/Co/Pt sample system on SiC.	3
2.1	Schematic sketch of the graphene structure and representation of graphene's orbital configuration.	6
2.2	Schematic sketches of a silicon carbide double layer and the two possible silicon carbide double layer stacking types.	7
2.3	Representation of the partially bonded ($6\sqrt{3} \times 6\sqrt{3}$) R30°-reconstruction, also called buffer layer, on SiC.	8
2.4	Illustration of the four steps of the PASG method.	10
2.5	Illustration of the Stoner model for the 3d shell.	13
2.6	Magnetic anisotropies in a bulk and in a layered system.	14
2.7	Overview of different skyrmion types, including various helicities, vorticities, and combinations of skyrmions.	16
2.8	Simple Bloch-type merons with different polarities and vorticities.	17
3.1	Experimental data of the IMFP, the universal curve, and TPP-2M of different elements.	21
3.2	Schematic representation of the photoemission, the Auger-Meitner effect, and fluorescence.	24
3.3	Illustration of spin-orbit coupling.	27
3.4	Illustration of the principle of angle-resolved photoelectron spectroscopy.	28
3.5	Photoelectron spectrum model of the C 1s core level of ethyl-trifluoroacetate as an example of chemical shift.	29
3.6	Illustration of the yield of secondary electrons in PEEM.	31
3.7	Schematic representation of the topographic and work function contrast mechanism in PEEM.	33

3.8	Example of the chemical contrast of X-PEEM, showing an X-PEEM image, corresponding XAS spectra, and a difference image.	35
3.9	Illustration of the XMCD effect and the resulting XAS and XMCD spectra.	37
3.10	Geometry of the experimental X-PEEM setup.	38
3.11	Ewald construction for two dimensional scattering.	40
4.1	Setup for the CCS preparation of the silicon carbide at TU University	43
4.2	Schematic representation of the setup used for the PASG preparation located at the PTB Braunschweig.	44
4.3	UV-PEEM chamber at the TU University	45
4.4	Sketch of the UV-PEEM system.	47
4.5	Sample holder used for UV-PEEM measurements.	47
4.6	Schematic representation of the LEED system used.	48
4.7	Schematic representation of the XPS setup at DELTA.	49
4.8	Sample holder used for XPS measurements.	50
4.9	Schematic representation of the XPS spectrometer.	51
4.10	Sample holder used X-PEEM measurements.	52
4.11	Sketch and photo of the X-PEEM system used.	53
5.1	Image of an electron beam evaporator and schematic of the cooling cylinder and its inner parts.	58
6.1	UV-PEEM images of the sample system in all preparation states. . .	60
6.2	UV-PEEM image of a sample after Pt deposition and subsequent annealing and sketch illustrating wetting of the Pt.	61
6.3	LEED pattern of a pristine sample, showing the $(6\sqrt{3} \times 6\sqrt{3})$ R30°-reconstruction on SiC.	62
6.4	LEED pattern of the sample system after intercalation of 4 Å Pt. . .	63
6.5	CLSM image of a sample after intercalation of 8 Å Pt.	64
6.6	LEED pattern of the sample system after intercalation of 2.4 nm Co. . .	65
6.7	XPS survey spectra of the initial SiC surface reconstruction and after intercalation of 4 Å Pt + 3 nm Co.	66
6.8	High resolution C 1s XPS spectra of the sample system in all preparation states.	69

6.9	High resolution Si 2p XPS spectra of the sample system in all preparation states.	72
6.10	High resolution Pt 4f XPS spectra of the sample system in all corresponding preparation states.	74
6.11	High resolution Co 3p XPS spectra of the sample system in all corresponding preparation states.	75
6.12	Intensity ratios of normalized XPS intensities after to before annealing of the Co 3p and C 1s signals as a function of polar angle.	76
6.13	Illustration of the correction process for X-PEEM images.	80
6.14	Illustration of the determination of the magnetization components using X-PEEM images.	81
6.15	X-PEEM images with chemical contrast (XAS images) and in-plane magnetization angle of the embedded Co-layer.	83
6.16	XAS image of a sample of type A after intercalation of 2.6 nm Co and 4 Å Pt.	85
6.17	XAS intensities of the three different areas of sample A	86
6.18	Close-up of the in-plane magnetization angle of sample A	87
6.19	Magnetic hysteresis curve from MOKE measurements of sample A taken with light polarization in transversal direction.	88
6.20	Close-up of the in-plane magnetization angle of sample B	89
6.21	Close-up of the in-plane magnetization angle of sample C	90
6.22	Magnetic out-of-plane component of sample A	91
6.23	Magnetic out-of-plane component of sample B	92
6.24	Magnetic out-of-plane component of sample C	93
C.1	Overview of the X-PEEM images and close-ups of sample A	117
C.2	Overview of the X-PEEM images and close-ups of sample B	118
C.3	Overview of the X-PEEM images and close-ups of sample C	119

Chapter

List of Tables

6.1	Sequence of images taken using X-PEEM at each sample position and azimuth angle.	78
A.1	Parameters for fitting the C 1s XPS spectra shown in Figures 6.8. . .	103
A.2	Parameters for fitting the Si 2p XPS spectra shown in Figures 6.9. . .	106
A.3	Parameters for fitting the Pt 4f XPS spectra shown in Figures 6.10. .	108
A.4	Parameters for fitting the Co 3p XPS spectra shown in Figures 6.11.	109

Chapter Introduction

1

The ongoing tremendous progress of electronic devices towards further miniaturization and enhanced performance poses a number of significant and further growing challenges. Among these challenges are the requirements for decreased power consumption and improved heat dissipation [2]. The field of spintronics [3] offers solutions to these challenges, as it provides enormous potential for high-density data storage, high processing speed, and low power requirements [4–7]. Within this research field, effects such as giant magnetoresistance (GMR) [8–10] and tunnel magnetoresistance (TMR) [11–13] enable a wide variety of applications. For instance, magnetoresistive random access memories (MRAM), MRAMs with spin-transfer torque (STT-MRAM), and magnetic field sensors are the subject of current research [14, 15].

In order to use the great potential of spintronic applications, there is a requirement for suitable spin transport channels, topologically stable spin textures, and fast motion of chiral textures [16]. One highly promising candidate in this context is graphene since it is known for its long spin-lifetime and diffusion-length of several micrometers even at room temperature. These features make it extremely interesting for applications such as in lateral spin-transport devices [17]. Graphene is a 2D material composed of a single layer of carbon atoms arranged in a hexagonal structure. Its first successful production in isolated form in 2004 was followed by numerous studies demonstrating its remarkable properties, including its immense potential in spintronics [17–19]. In 2010, Geim and Novoselov were awarded the Nobel Prize for their pioneering work in preparing and investigating of this groundbreaking material [20, 21]. The original preparation method was a process of detaching graphene flakes from graphite using adhesive tape. While this method is straightforward, other techniques are needed to produce larger sheets of graphene in a reproducible and reliable manner.

In addition to chemical vapor deposition, which can be used for preparation on conduction substrates, graphene can also be grown by sublimating silicon atoms from a silicon carbide (SiC) wafer. Initially, the growth of graphene on SiC was conducted in ultra-high vacuum (UHV). This variant suffered from an inhomogeneity of the graphene layers due to the too-high sublimation rate. Preparation in an inert gas atmosphere overcame this issue and paved the way for high-quality, single domain graphene on SiC as a foundation for many different sample systems [22, 23].

Combining graphene with a ferromagnet like cobalt (Co) results in several advantageous effects, such as Dzyaloshinskii–Moriya interaction (DMI), a strong Rashba effect, and spin filtering [24, 25]. Moreover, it enhances perpendicular magnetic anisotropy (PMA) in cobalt and other transition metals [16, 26–28], which stabilizes magnetization states over a long time [29–36]. Another method that has been recently used to induce PMA in cobalt is combining it with a heavy non-magnetic metal such as platinum (Pt) [37, 38]. A Co/Pt system also offers the possibility of spin-based high-density memory storage as well as high domain-wall velocities due to the presence of chiral Néel-type magnetic domain walls [16]. This feature may enable faster processing speed in future applications [39].

In this thesis, the combined G/Co/Pt system prepared on SiC was investigated. Combining the G/Co and Co/Pt systems aims to unite the respective mentioned beneficial properties. Figure 1.1 shows a schematic sketch of the system. Next to the magnetic structure, its chemical and general structural properties were studied as a foundation for future spintronic applications. In addition to all advantageous characteristics mentioned, the inert properties of graphene protect the sample surface from oxidation [40]. Moreover, the Pt-layer is effective as a diffusion barrier up to certain temperatures, which prevents the formation of cobalt silicide beneath the surface [41]. Cobalt silicides are suspected of weakening the Co-layer’s magnetic order [38, 42–44].

DMI and PMA were reported in a G/Co/Pt system prepared on MgO(111) [16]. In that study, a rather thick Pt-layer of 300 Å reduced the influence of the substrate. One purpose of the present study was to experimentally investigate the influence of the substrate. Thus thin films of platinum were studied, ranging from 2 Å to 8 Å. The SiC-substrate offers several decisive advantages. Most importantly, the film quality of graphene grown on SiC is of utmost quality. For instance, single-crystallographic

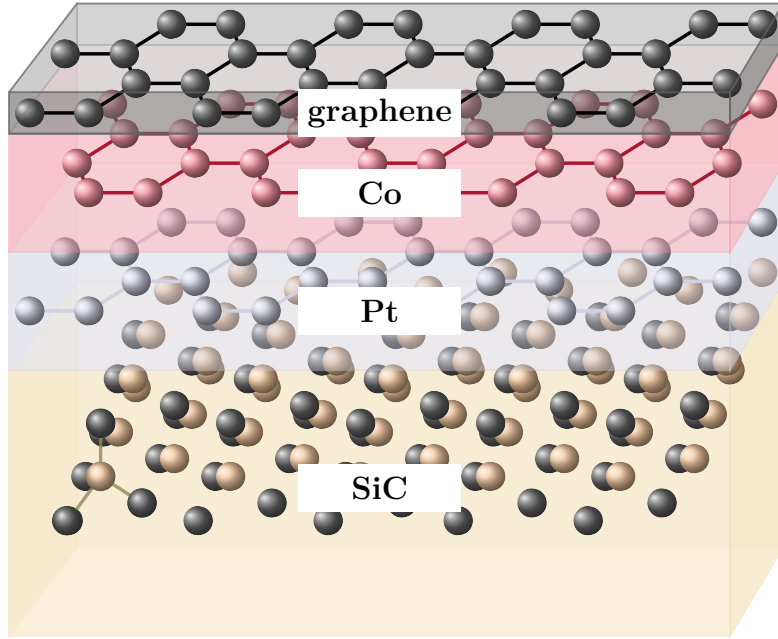


Figure 1.1: Sketch of the G/Co/Pt sample system on SiC.

graphene domains have been reported over exceptionally large areas on this substrate, in contrast to others [16, 40]. Furthermore, it has been observed that graphene grown on SiC exhibits a very high spin injection efficiency [45]. In contrast, graphene grown on metal or metal oxide substrates usually leads to multiple domains over the whole sample surface [16]. Multiple domains might impair the formation of magnetic structures.

To incorporate the platinum and cobalt layers within the sample system, intercalation was utilized. Intercalation originated from chemistry and describes the insertion of so-called guest species into a lamellar host structure [46]. In the context of graphene grown on SiC, it means the insertion of atoms between the graphene layer and the SiC substrate by penetrating the graphene. Thus, the preparation of ultra-thin metal layers beneath graphene is enabled. This method is well-established for many different materials, such as H₂ [47], Au [48, 49], and in addition to cobalt [38], further 3d-metals like Fe [50] and Cu [51]. A range of distinct properties of the resulting system can be tailored by selecting the material to be intercalated and specifying its thickness beneath graphene [47, 52, 53]. Moreover, bonds between the first carbon layer on SiC, referred to as $(6\sqrt{3} \times 6\sqrt{3})$ R30°-reconstruction, and the substrate

impair this layer's properties in comparison to freestanding graphene. Intercalating a material underneath the reconstruction results in the release of the bonds and the transformation of the reconstruction into quasi-freestanding graphene [47].

This work employs three main techniques to offer a comprehensive study. These are photoemission electron microscopy (PEEM), low energy electron diffraction (LEED), and x-ray photoelectron spectroscopy (XPS). Intercalation is induced by sample annealing up to a temperature determined by the material to be intercalated. Insights into the intercalation process and determination of the required temperatures for both platinum and cobalt intercalation will be gained using ultraviolet PEEM (UV-PEEM). Structural and chemical properties of the system in each state of the preparation will be revealed by LEED and XPS, respectively. This includes investigating the crystalline structure of each layer of the sample system and showing which types of silicide compounds form. Finally, the morphology of the embedded Co-layer and, especially, the magnetic domain structure will be analyzed by means of x-ray PEEM (X-PEEM) in combination with x-ray magnetic circular dichroism (XMCD). This investigation will show the presence of numerous spin vortices of different sizes and types, indicating strong DMI and offering potential use in spintronics. [1]

This thesis is structured in 7 chapters. Following this introduction, Chapter 2 will introduce the topics of graphene and magnetism, while Chapter 3 will present the theoretical background of the measurement techniques used. Subsequently, all experimental setups will be presented in Chapter 4 and the steps for sample preparation will be reviewed in Chapter 5.

Chapter 6 will provide the results of each measurement technique, which are UV-PEEM in Section 6.1, LEED in Section 6.2, XPS in Section 6.3, and X-PEEM in Section 6.4. Lastly, a conclusion of the results, provided in Chapter 7, will complete this thesis.

Chapter Background | 2

In this chapter, the foundation for this work is set. It begins by introducing graphene, covering aspects such as its atomic structure, the substrate silicon, the growth methods used, and the interaction of graphene with silicon carbide. Subsequently, ferromagnetism and magnetic structures like skyrmions and merons are explained as a basis for analyzing photoemission electron microscopy images with magnetic contrast.

2.1 Graphene: Introduction and preparation

2.1.1 Discovery, Structure, and Properties

Graphene is a two-dimensional material composed of a single layer of carbon atoms arranged in a hexagonal lattice. It captures significant attention due to its exceptional mechanical and electronic properties and potential applications, for example, in electronic and spintronic devices [4–7, 17]. In this chapter, graphene’s discovery, structure, and electronic properties are introduced, highlighting its relevance to surface science and beyond.

In 2004, single-layer graphene was successfully isolated and characterized by Novoselov and Geim using the “Scotch tape” method [20]. This groundbreaking research, honored with the Nobel Prize in Physics in 2010, paved the way for extensive exploration of graphene’s properties and applications. Before this, it was controversial whether isolated graphene could exist since it was assumed to be strictly two-dimensional, and theoretical physics states that two-dimensional crystalline structures

are unstable at finite temperatures [54]. Later studies have resolved this inconsistency by showing that the atoms in graphene do indeed exhibit slight buckling [55].

Graphene's atomic structure and orbital configuration are shown in Figure 2.1. It consists of planar-arranged carbon atoms connected in a honeycomb lattice. Neighboring atoms in this lattice have a distance of 1.42 \AA and the lattice constant is 2.46 \AA . With this structure, graphene can be described as a single graphite layer [56]. The atoms in graphene are sp^2 -hybridized. Consequently, each carbon atom forms three in-plane σ -bonds with its three nearest neighbors, resulting in a highly stable lattice. The remaining electron of each carbon atom contributes to an out-of-plane π -bond orbital. These orbital formations are responsible for many of graphene's unique characteristics, like the linear energy dispersion of the band structure near the Dirac point or its extraordinarily high carrier mobility and mechanical strength [57–60].

For graphene to truly possess these outstanding properties, it requires high-quality preparation. There are various methods to prepare graphene [61]. The one used in this work is the epitaxial growth on silicon carbide [22, 23, 62].

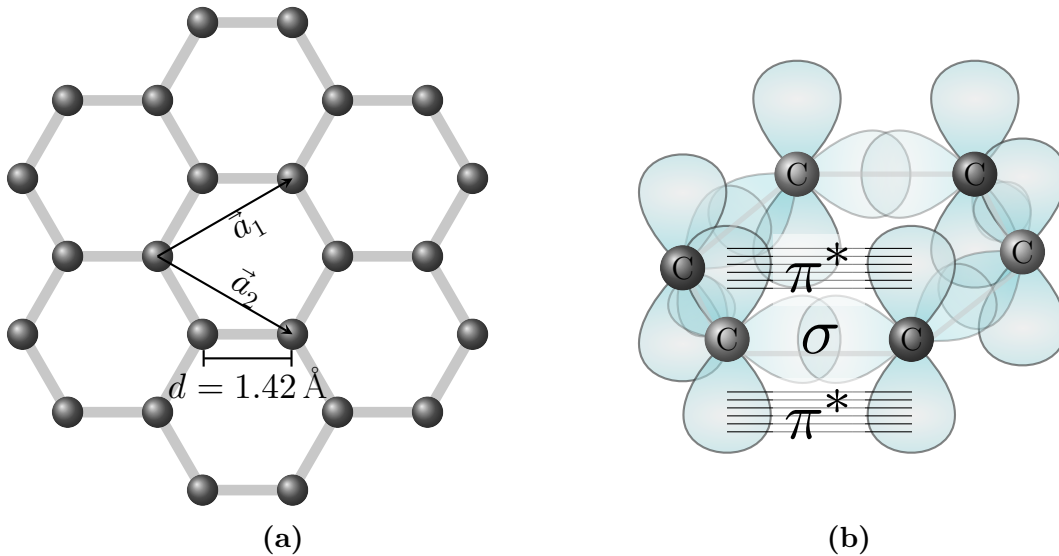


Figure 2.1: (a) Schematic sketch of the graphene structure. Lattice vectors \vec{a}_1 and \vec{a}_2 , with $|\vec{a}_i| = 2.46 \text{ \AA}$, and the next-neighbor distance d are shown. (b) Representation of graphene's orbital configuration. Exemplary, some σ - and π^* -bonds are marked.

2.1.2 Silicon Carbide: Composition and Structure

Silicon carbide (SiC) has a wide bandgap, a high thermal conductivity, and is chemically inert, making it suitable for a variety of applications in the field of electronics [63, 64]. To prepare graphene, silicon carbide can be used as a substrate for epitaxial growth. This section introduces the composition and structure of silicon carbide. This provides the basis for the explanation of graphene preparation in the next section.

Silicon carbide is a compound semiconductor consisting of silicon (Si) and carbon (C) atoms in a 1 : 1 ratio. The silicon and carbon atoms form covalent bonds in a tetrahedral structure, resulting in Si-C double layers. These double layers can be stacked congruently or being rotated by 60° , as shown in Figure 2.2. Due to these options, SiC exists in various stacking sequences. These so-called polytypes are named by the number of layers in one unit cell and the crystal symmetry: H: hexagonal, C: cubic, and R: rhombohedral. Different polytypes differ in their properties. For example, the band gap ranges from 2.3 eV for 3C-SiC up to 3.3 eV for 6H-SiC [65]. In this study, the polytypes 4H-SiC and 6H-SiC were used. For preparation, it is important whether the surface is silicon or carbon terminated. For hexagonal SiC, these surfaces are referred to as the (0001) -surface and the $(000\bar{1})$ -surface, respectively. Referring to the termination, the surfaces are also called silicon side and carbon side. In this study, only the silicon terminated side was used for preparation, since preparation on the carbon side is much less reproducible.

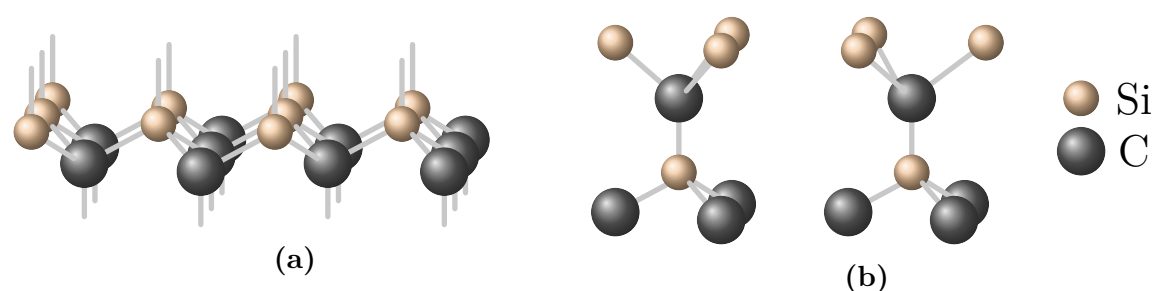


Figure 2.2: Schematic sketches of a silicon carbide double layer (a) and the two possible silicon carbide double layer stacking types, which differ in that the upper Si-layer is rotated by 60° (b). (Based on [66])

2.1.3 Graphene on Silicon Carbide: Growth and Properties

Graphene can be grown on silicon carbide substrates by annealing in a vacuum or inert gas atmosphere. When silicon carbide is heated to high temperatures, silicon atoms from the top layers sublime while the carbon atoms remain on the surface. This is due to the vapor pressure of carbon being negligible compared to that of silicon [23]. Under proper preparation conditions, the remaining carbon atoms self-assemble into well-ordered 2D layers. Annealing above 1000 °C leads to the $(\sqrt{3} \times \sqrt{3})$ R30°-reconstruction of silicon carbide. This converts into the desired $(6\sqrt{3} \times 6\sqrt{3})$ R30°-reconstruction for temperatures above 1100 °C [66]. The crystal structure of the underlying SiC substrate is retained in this layer. It already has the structure of graphene, but its properties are attenuated due to covalent bonds to the substrate. For this reason, this layer is called buffer layer. Figure 2.3 illustrates this state. Continuing annealing leads to the growth of additional graphene layers underneath. Unfortunately, it is usually unavoidable that one layer starts growing while the previous layer is still forming.

Proper preparation conditions are crucial to control this and other effects, thus obtaining high-quality graphene, characterized by single-domain layers and low defect densities. The two distinct methods to prepare such high-quality samples are explained in the following.

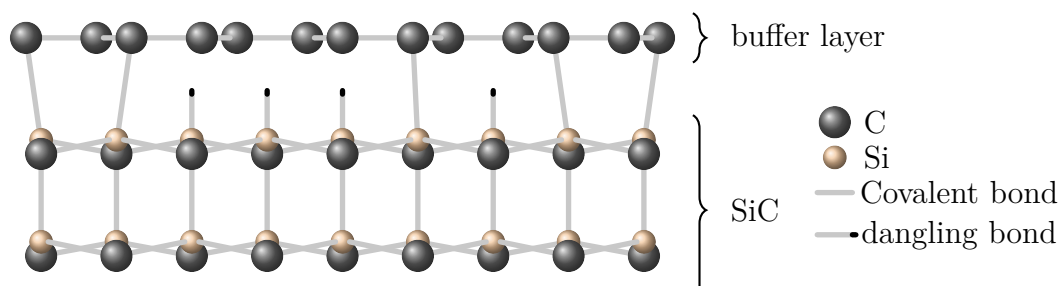


Figure 2.3: Representation of the partially bonded $(6\sqrt{3} \times 6\sqrt{3})$ R30°-reconstruction, also called buffer layer, on SiC. (Based on [40])

Confinement controlled sublimation (CCS)

The sublimation rate of the silicon atoms and the mobility of the carbon atoms forming the graphene layers are crucial to the quality of the resulting sample. A low sublimation rate increases the time available for the carbon atoms to form the reconstruction, while a high temperature increases their mobility in this process [22]. Both of these properties are desirable. Unfortunately, since a high temperature leads to a high sublimation rate, it is a challenge to tune both. The confinement controlled sublimation method (CCS) and preparation in inert gas keep the sublimation rate low even for high preparation temperatures [23]. The pressure of the gas acts as a barrier, making it less likely for a silicon atom to leave the surface. Confinement controlled means closing the sample in a confined small volume. Due to the small confinement, the local partial pressure further increases during the sublimation of the silicon atoms because they cannot easily leave the vicinity of the sample. This makes the sublimation rate self-limiting. A small leak is used to tailor this effect.

Unfortunately, when preparing buffer layer on silicon carbide, step-bunching and monolayer growth of graphene over the buffer layer is unavoidable if a complete reconstruction layer is to be prepared [23, 67]. Both these effects are undesirable. Step-bunching describes the merging of several terraces into a single large one with a huge step-height. This reduces the structural and magnetic homogeneity of the system and thus hinders the formation of magnetic features in a final sample system, for instance. Monolayer growth also reduces the system's homogeneity, as the monolayer is only present in some regions. Completing this layer would result in another layer starting to form. Elements added to form further layers can avoid monolayer regions, resulting in these layers being incomplete [22, 38].

Polymer assisted sublimation growth (PASG)

The flatness of the buffer layer can be improved using the polymer-assisted sublimation growth (PASG) method, which comprises four steps. First, the substrate surface is coated with a polymer consisting mainly of carbon. Subsequent annealing leads to the decomposition of the polymer. The remaining carbon atoms form disordered carbon networks. In the third step, the temperature is increased. This initiates

sublimation growth and causes the networks to combine and convert into buffer layer. In the fourth step, the temperature is increased even further. As a result, more silicon atoms sublime and the buffer layer grows over the step edges into one continuous layer.

Due to the additional carbon from the polymer, step-bunching is avoided. Therefore, samples prepared using this method are ultra-smooth with ultra-small terrace heights of only one or two SiC layers [68]. This is the most important criterion for a good quality buffer and graphene layer, resulting in enhanced electron mobility and increased charge carrier densities [69].

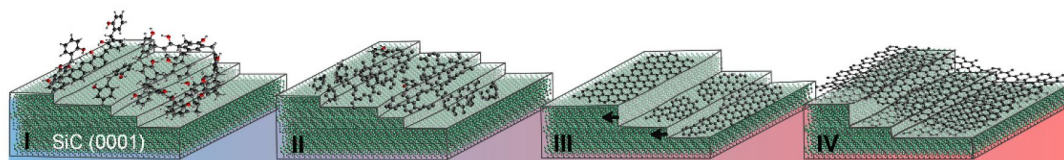


Figure 2.4: Illustration of the four steps of the PASG method. (I) Coverage (II) Polymer decomposition (III) Sublimation growth and buffer layer formation (IV) Connecting individual domains. [70]

2.1.4 Intercalation of Graphene on Silicon Carbide

To release the covalent bonds between silicon carbide and the buffer layer, intercalation can be performed. Intercalation is the insertion of additional atoms, called intercalant, between the buffer layer and the substrate. This is done by first coating the buffer layer with the intercalant, which can then intercalate if the system is annealed to a sufficient temperature. The temperature needed for intercalation depends on the material and ranges from room temperature to several hundred degrees Celsius [71, 72]. As a result, the covalent bonds of the substrate are saturated by the intercalant and the buffer layer is lifted and becomes quasi-free standing graphene.

The intercalated atoms can modify the properties of the graphene and vice versa, leading to new possible applications, like high-performance field effect transistors (FETs) [73], gas sensing applications [74], and quantum Hall devices [75]. In this work, first platinum and then cobalt is intercalated. Due to the interaction of the individual resulting layers, the magnetic structure of Co-layer is of great interest.

2.2 Magnetism: Fundamentals and structures

Materials can be paramagnetic, diamagnetic, or ferromagnetic. While paramagnetic and diamagnetic materials usually do not influence a magnetic field noticeably, ferromagnetic materials do. This magnetism primarily originates from the electrons' orbits and spins and is characterized by the Bohr magneton μ_B .

In this section, we introduce fundamental aspects of magnetism, including ferromagnetism concerning spontaneous magnetization and the band model, as well as resulting effects and structures, like magnetic domains, anisotropies, and skyrmions. This serves as a theoretical basis for both the investigated magnetic properties of the sample system and the techniques used to study them.

2.2.1 Spontaneous magnetization

Spontaneous magnetization is the alignment of magnetic moments in individual domains, even without an external field. This characterizes ferromagnetic materials.

Spontaneous magnetization is made possible as a result of Pauli's exclusion principle and Hund's rules [76, 77]. These show that it is energetically more favorable if electrons have the same spin due to a lower coulomb repulsion. Consequently, the energy resulting from the coulomb repulsion is minimized for electrons with the same spin [78]. The difference between parallel and anti-parallel aligned spins is called exchange interaction [79]. This interaction causes the ferromagnetic character of 3d metals since these metals contain unpaired electrons, which can align accordingly.

However, magnetic order is disturbed by thermal fluctuations. Moreover, if the material specific so-called Curie temperature T_C is exceeded, no stable magnetic order is possible. To describe the Curie temperature, the exchange interaction can be defined by an effective field, called the exchange field, molecular field, or Weiss field. This field only acts on the electron spin, not on its orbital magnetic moment. It is the origin of long-range inter-atomic magnetic order. Consequently its value determines the Curie temperature. The only elements for which a Curie temperature is significantly above room temperature are iron, cobalt, and nickel. For this reason, they are called ferromagnets.

2.2.2 Band model of ferromagnetism

Simple calculations of the atomic moments of iron, cobalt, and nickel under Hund's rules unexpectedly led to odd fractions of the Bohr magneton. An explanation for this was found by assuming that the 3d electrons in these atoms are not strictly localized, followed by the development of the band theory. A suitable description for ferromagnetic materials in this context was found with the Stoner model. [80, 81] It derives from the Hartree-Fock approximation of the Hubbard model [82].

The model assumes that the bonding interaction between the 3d electrons causes smearing of their energy states into a band [83–85]. In a lattice, the periodically arranged atoms cause a periodic variation of the individual energy states. This increases the bandwidth with the inverse lattice constant. In a simple approximation, the resulting bands can be described as semicircles. Considering the exchange interaction and exchange field, the bands for spin-up and spin-down electrons are shifted relative to each other by the exchange splitting $\Delta \simeq 1$ eV [86]. The Fermi level is the same for both spin configurations, resulting in such a rearrangement of the electrons that one band is filled more than the other. In the ground state, states below the Fermi energy E_{Fermi} are filled and called electron states. Those above are empty, these are called hole states. The spin states with the larger number of electrons are called *majority spins* and the corresponding band is the *majority band*. Vice versa, the terms *minority spins* and *minority band* describe the spin states with the smaller number of electron states and the corresponding band. An illustration of the electronic band structure of a ferromagnetic 3d metal near the Fermi energy is shown in Figure 2.5.

In this image, an external field $H_{\text{ext}} \parallel M$ is used to align the magnetization M . The difference in the number of majority and minority states determines the magnetic moment $|m|$, which is given in units of μ_{B} .

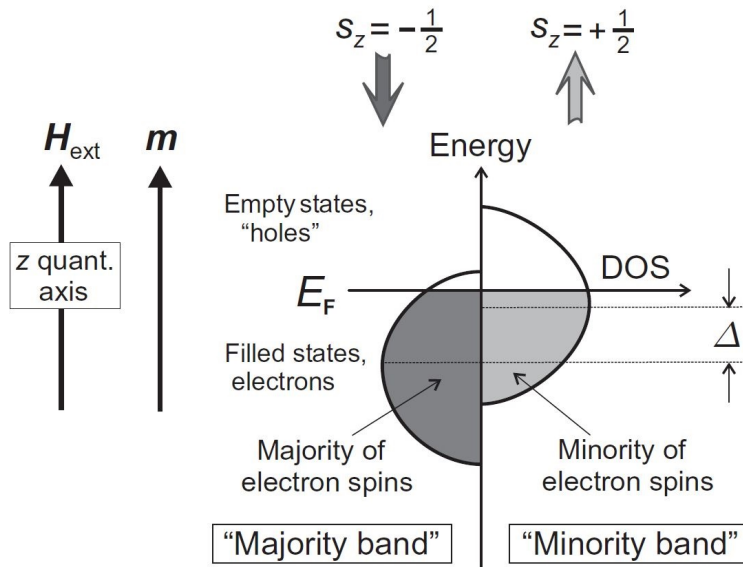


Figure 2.5: Illustration of the Stoner model for the 3d shell. Occupied states, called electron states, are filled in gray, unoccupied ones, called holes, are unfilled. The density of states is simplified by semicircles. [80]

2.2.3 Magnetic Domains

As spontaneous magnetization occurs, areas with collective magnetization direction form. These are called magnetic domains or Weiss domains. They orient themselves in different directions to minimize the resulting stray field and, thus, the total magnetization [87]. Individual domains are separated by so-called domain walls. Within these the magnetization direction rotates from the direction of one domain to that of the other. Since the magnetization direction of the domain walls is not aligned with that of the domains, the total energy is increased. For that reason, spontaneous magnetization can lead to a single domain state if the stray field energy of such a state is lower than the domain wall energy. Specific ultra-thin films and nano-sized particles are known to exhibit such behavior [87].

The domain width is determined by the exchange energy and the anisotropy energy, explained in the next section. A wide domain wall with slowly rotating magnetization minimizes the exchange energy. In contrast, the anisotropy energy is minimized for a domain wall with zero width and a sharp change in direction. [88]

2.2.4 Magnetic Anisotropy

To align individual magnetic domains of a sample, an external field can be applied. For crystalline samples, the strength of the applied field needed for full alignment depends on its direction relative to the orientation of the crystal lattice. Directions in which minimum strength is required are called easy axes and those with maximum strength required are called hard axes. Multiple easy and hard axes can exist for one crystal lattice. This directional dependence is aligned with the magnetic anisotropy.

Magnetic anisotropy is mainly determined by the shape anisotropy and the magnetocrystalline anisotropy. The film thickness of the magnetic layer strongly influences which of these anisotropies dominates. Normally the magnetisation is parallel to the surface of the material, which is called in-plane magnetization and is caused by the shape anisotropy. Shape anisotropy results from the energy reduction associated with the magnetic stray field outside the lattice and is related to dipole-dipole interaction. In thin films, magnetocrystalline anisotropy may predominate. This leads to perpendicular magnetic anisotropy (PMA), where the magnetization direction is perpendicular to the surface normal. This type of anisotropy is essential for certain applications like spintronic devices. It arises from the coupling of an electron's spin moment to its orbital moment, which in turn is linked to the lattice. Thus, the magnetization direction is aligned with the crystal axis. Both types of anisotropies are depicted in Figure 2.6. [80]

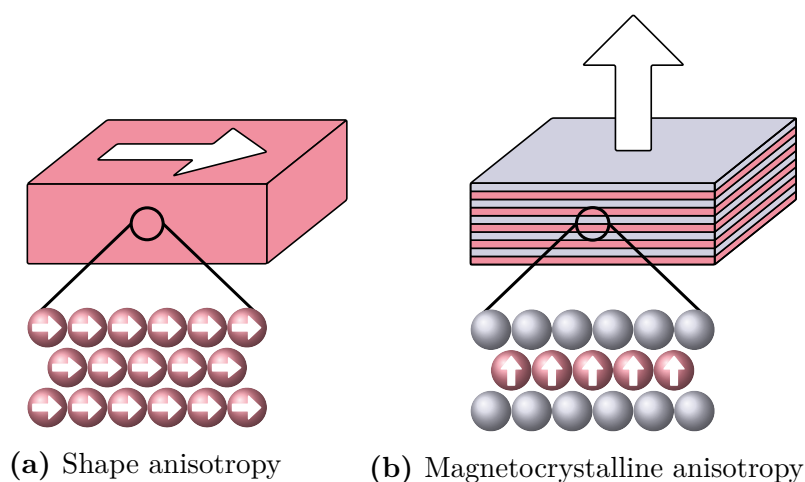


Figure 2.6: Magnetic anisotropies in a bulk and in a layered system. (Based on [80])

Furthermore, the substrate and other layers in a system can also influence or change the magnetic easy axis by interdiffusion, its roughness, or steps [89]. Since easy axis directions are aligned with the direction of spontaneously formed domains, experimental methods can directly determine the easy axis. A suitable method for this purpose is X-PEEM, introduced in section 3.3.

2.2.5 Magnetic skyrmions

Magnetic skyrmions are nano-sized vortex configurations of spins in a thin magnetic layer, initially predicted by Tony Skyrme in the context of particle physics [90, 91]. They are topologically protected, which makes them extremely stable even at small scales [92]. Therefore, they are promising candidates in spintronics as information carriers in data storage devices, such as racetrack memory devices [93, 94], and in logic devices [95].

Skyrmions exist in ferromagnetic environments with magnetic anisotropy. They can be described by a continuously changing magnetization density $\rho_{\mathbf{md}}(\mathbf{r})$ which in its center is oriented opposite to the confinement. This structure leads to a non-trivial real-space topology [96, 97]. Different types of skyrmion are primarily determined by two parameters:

1. **polarity** $p = \pm 1$: Out-of-plane magnetization direction of the skyrmion host ("down/up")
2. **vorticity** $c \in (0, \pm 1, \pm 2, \dots)$: Also, but not as precisely, called chirality ("anti-clockwise/clockwise"). Describes the winding type of the skyrmion and results from the polar angle, which can only wrap around the center in multiples of 2π . Skyrmions with negative c are called antiskyrmions.

Combined, these lead to the **topological charge** $N_{\text{Sk}} = c \cdot p = 0, \pm 1, \pm 2, \dots$. For positive/negative values, skyrmions are called right-handed/left-handed.

Some basic skyrmion types are depicted in Figure 2.7. Another characteristic is the in-plane magnetization polar angle Θ_{mpa} , which depends on the position vector ϕ_{p} and the magnetization density ρ_{md} . It is given by $\Theta_{\text{mpa}} = \rho_{\text{md}}\phi_{\text{p}} + \gamma$. Its offset γ , called helicity, is the distinguishing parameter between Néel-type skyrmions with $\gamma = 0$ and Bloch-type skyrmions with $\gamma = \pm\pi/2$. Intermediate versions are also possible, as shown in Figure 2.7b. Special types are ferrimagnetic and synthetic antiferromagnetic skyrmion, shown in Figures 2.7g and 2.7h, for which the topological charges of the two subskyrmions compensate each other.

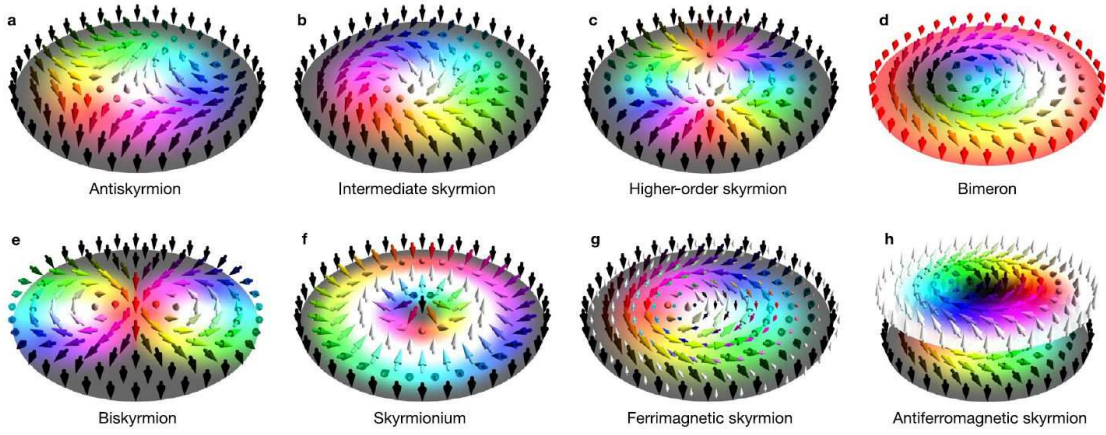


Figure 2.7: Overview of different skyrmion types. The first row shows skyrmions with various helicities and vorticities: (a) antiskyrmion ($c = -1$, $N_{\text{Sk}} = -1$), (b) intermediate skyrmion ($\gamma = \pi/4$, $N_{\text{Sk}} = 1$), (c) higher-order skyrmion ($N_{\text{Sk}} = 2$), and (d) bimeron ($N_{\text{Sk}} = -1$).

The second row shows combinations of two skyrmions: (e) biskyrmion ($N_{\text{Sk}} = 2$), (f) skyrmionium ($N_{\text{Sk}} = 0$), and (g) ferrimagnetic and synthetic antiferromagnetic skyrmion.

The arrow color and direction represent the orientation of the local magnetic moment. [96]

Merons

This work focuses on merons, which are skyrmionic formations in an in-plane magnetized system. They can be described as half-skyrmions and possess properties of both skyrmions and domain walls. Equivalent to antiskyrmions, merons with $N_{\text{Sk}} = -1$ are called antimerons. The combination of two merons, as shown in Figure 2.7d, or of a meron and an antimeron is called a bimeron. Merons also differ in polarity and vorticity. Four types of Bloch-type merons with $p = \pm 1$ and $c = \pm 1$ are depicted in Figure 2.8. [98–100]

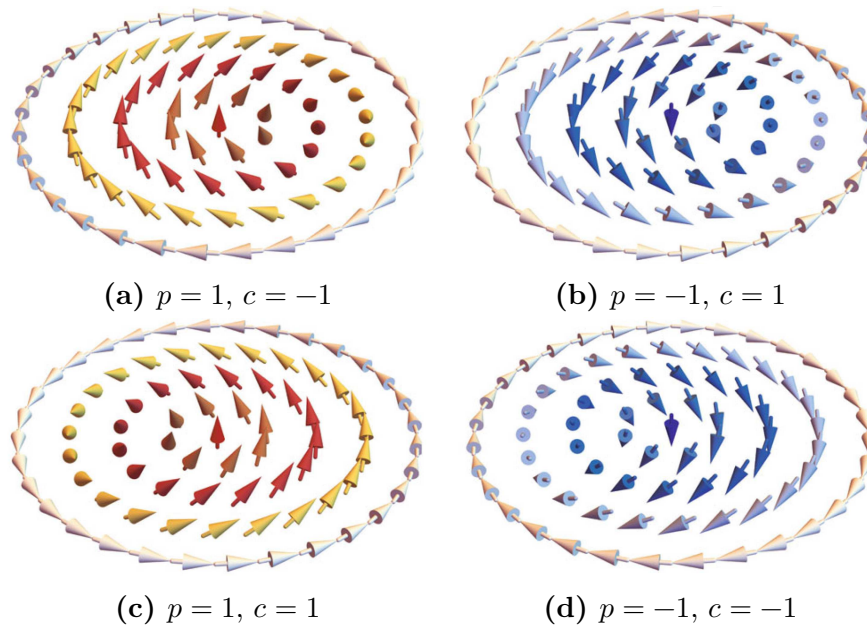


Figure 2.8: Simple Bloch-type merons with different polarities and vorticities. [101]

Stabilizing mechanisms - Dzyaloshinskii–Moriya interactions (DMI)

A crucial property of skyrmions is their stability. If the stability is high enough, not only do single skyrmions appear, but they can also form periodic lattices over large surfaces [102, 103].

If the magnetic moment describing a skyrmion would be continuously in space, they would be stable due to the topological protection preventing their transformation into a uniform ferromagnet. However, since real skyrmions consist of magnetic moments at

discrete positions, this protection is not strict [104]. Consequently, further stabilizing interactions are necessary. The most important ones in this context are the exchange interaction [105], the dipole–dipole interaction [106], and the Dzyaloshinskii–Moriya interaction (DMI) [95]. While the dipole–dipole interaction can stabilize larger objects up to several micrometers in diameter, the DMI is crucial for objects down to sizes in the sub-nanometer range [95].

Concerning the sample system investigated, DMI is known to play the most important role [16, 107]. This chiral interaction, given by:

$$H_{\text{DMI}} = \frac{1}{2} \sum_{ij} D_{ij} \cdot (s_i \times s_j), \quad (2.1)$$

acts as an antisymmetric exchange interaction, with DMI vectors $D_{ij} = -D_{ji}$. It is an energy correction due to spin–orbital coupling in a system with broken inversion symmetry [108]. Depending on the exact properties of the system, the DMI favors different types of skyrmions [102, 109, 110]. In addition, its strength significantly affects the size and stability of a skyrmion [111, 112].

At an interface of a magnet and a heavy metal, like the investigated Co/Pt interface, the DMI vectors are perpendicular to the bonds of the magnet’s atoms and parallel to the interfacial plane [96]. As a result, skyrmionic formations are stabilized. [107]

Chapter Theoretical background

3

All the methods used in this work are based on the detection of electrons emitted by a sample. Such emission is explained by the photoelectric effect. In addition, the depth from which electrons can leave a sample without losing energy is of great importance. It defines the surface sensitivity of a method and is determined by the inelastic mean free path. In this chapter, these two fundamentals, the photoelectric effect and the inelastic mean free path, are first introduced. Then the measurement methods are described. These are photoelectron spectroscopy, photoemission electron microscopy, and low energy electron diffraction. [113]

3.1 Fundamentals

3.1.1 Inelastic Mean Free Path of electrons in solids

The inelastic mean free path λ (IMFP) quantifies the average distance an electron travels within a material before undergoing inelastic scattering. When electrons move through matter, they can undergo different scattering processes. Elastic scattering results solely in a change in the electron's direction of motion without any energy loss. In contrast, inelastic scattering involves energy exchange between the electrons and the matter. In a solid, energy can be exchanged with the lattice vibrations (phonons) or with the electrons of the solid. The electron-electron interaction strongly dominates the resulting energy exchange due to its higher probability. Depending on whether the electron's kinetic energy E_{kin} is smaller or greater than the plasmon energy E_{p} , electron-electron interaction leads to single-electron scattering or plasmon excitations, respectively. [88, 114]

The initial intensity I_0 of unscattered electrons traveling through a solid is exponentially reduced as a function of the travel depth d and the IMFP:

$$I(d) = I_0 \exp\left(-\frac{d}{\lambda(E)}\right). \quad (3.1)$$

Thus, the IMFP quantifies the distance electrons can travel in matter without losing energy, which influences the depth sensitivity of various microscopy and spectroscopy techniques used in surface science [115].

Within the kinetic energy range used for most surface science techniques, electrons behave similarly to a free-electron gas. Consequently, the plasma frequency primarily determines the energy loss function, which is approximately the same for all materials [116]. For this reason, the IMFP within this energy range can be described by the so-called universal curve, which depends only on the energy of the incident electrons:

$$\lambda_{\text{UC}}(E_{\text{kin}}) = \frac{538a}{E_{\text{kin}}^2} + 0.41\sqrt{a^3 E_{\text{kin}}}. \quad (3.2)$$

The parameters of this equation were determined by fitting experimental data. The thickness of a monolayer a is given by:

$$a = \left(\frac{A}{\rho n N_{\text{A}}}\right)^{1/3}. \quad (3.3)$$

Here A is the molecular weight, ρ is the density, n is the number of atoms in one molecule, and N_{A} is the Avogadro constant. The universal curve applies to elements, inorganic compounds, organic compounds, and adsorbed gases, while its parameters differ for all of them. For elements, it has its minimum at $\lambda \approx 0.4$ nm with $E_{\text{kin}} \approx 40$ eV [117]. It describes the experimental data well for kinetic energies up to about 50 eV. Beyond this range, the theoretical TPP-2M formula provides a better description:

$$\lambda_{\text{TPP-2M}} = \frac{E_{\text{kin}}}{E_{\text{p}}^2 (\beta \ln(\gamma E_{\text{kin}}) - (C/E_{\text{kin}}) + (D/E_{\text{kin}}^2))}. \quad (3.4)$$

The parameters β , γ , C , and D are empirically determined, and E_p is the material-dependent plasmon energy of the free electron gas [118]. Figure 3.1 shows data of measured IMFP of different materials, the universal curve and the calculated TPP-2M function for the elements relevant in this work.

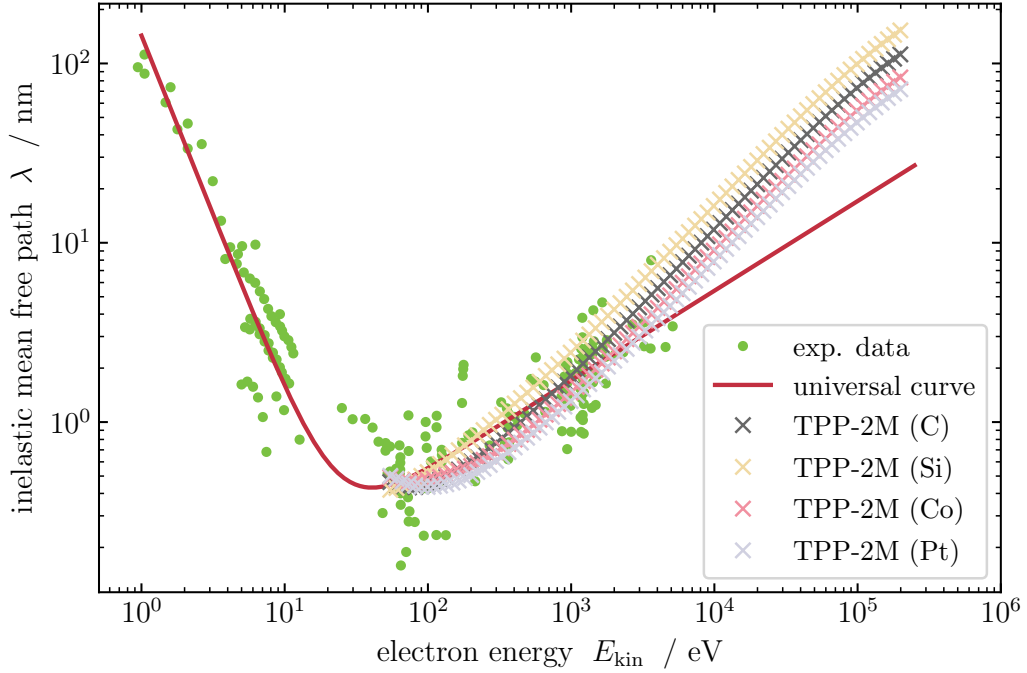


Figure 3.1: Experimental data of the IMFP, the universal curve, and the TPP-2M function for C, Si, Co, and Pt. [117, 118]

Experimentally, the IMFP can be determined using techniques such as low-energy electron diffraction (LEED) and elastic peak electron spectroscopy (EPES) [119, 120].

3.1.2 The Photoelectric Effect

When electromagnetic radiation, such as a photon, interacts with matter, a bonded electron within the matter can absorb the photon's energy and be emitted as a result. This phenomenon is called the photoelectric effect and an electron emitted this way is referred to as a photoelectron. The effect was first reported in 1887 by Heinrich Hertz, who exposed a metal cathode to ultraviolet light, resulting in electric

sparks [121]. His student Wilhelm Hallwachs continued his work by isolating the phenomenon and studying it quantitatively [122]. However, the dependence on the frequency of the light was not determined until 1902 by Philipp Lenard [123]. Still, the question remained as to why a minimum frequency is required to cause the effect. In 1905, Albert Einstein answered this by describing light as particles, photons, with an energy of $E_{\text{Photon}} = h\nu$, with ν being the frequency of the photons [124].

During photon-electron interaction, this energy is completely transferred to the electron. If the energy of a photon exceeds the sum of the binding energy E_{bin} with respect to the Fermi level and the materials work function $\Phi = E_{\text{vac}} - E_{\text{F}}$, it may induce the emission of an electron with the kinetic energy:

$$E_{\text{kin}} = h\nu - E_{\text{bin}} - \Phi. \quad (3.5)$$

This is called the Einstein equation [124] and its validity was proven in 1916 by Robert A. Millikan in his study about the "determination of the Plank's h" [125]. The work function is defined by the vacuum level E_{vac} and the Fermi level E_{F} .

In a simple model, the photoelectric effect can be described in three steps. First, a photon excites a bonded electron. Second, this photoelectron propagates through the solid. And third, if the photon's energy was sufficient, the electron can escape the solid [116, 126]. A more detailed description would require to include quantum mechanical processes [127–129].

Even though there are other interactions, such as the Compton effect or pair production, the photoelectric effect strongly dominates at photon energies for typical measurements. Typical energies are below 1000 eV, as are all those used in this work. [130]

The photoelectric effect is applied in a wide variety of techniques. The ones used in this work are presented in the following sections.

3.2 Photoelectron spectroscopy (PES)

Photoelectron spectroscopy (PES) is a powerful analytical technique to explore a sample's chemical properties. Based on the fundamental principles of the photoelectric effect and the Einstein equation 3.5, samples are irradiated with photons of a defined frequency and spectra of the number of electrons emitted are obtained as a function of their kinetic energy. These spectra provide an insight into the energy levels, electronic states, composition, and many other properties of a sample's surface.

The emission of photoelectrons and a resulting PES spectrum are sketched on the left side of Figure 3.2. In PES, the photon energy is fixed and the work function is constant. Therefore, there is a direct correlation between the kinetic energy and the binding energy. This allows the peaks in a spectrum to be assigned to individual core levels. In the case of strongly pronounced core level signals, additional quantized energy-loss peaks, e.g., plasmon peaks, may also occur. Furthermore, electrons originating from the valence band also cause a peak. In addition to these signals, there is a background caused by inelastically scattered electrons and a signal increase at low energies due to secondary electrons. [131]

Moreover, the photoelectric effect can induce further processes that can cause signals in PES spectra and in other investigative methods. If the electron emitted was a core level electron, an unoccupied hole-state remains. At the end of the lifetime of such a state, an electron with a lower binding energy fills up this state to lower the total energy of the atom [132]. During this transition, the electron releases energy, leading to either of two processes. In the first process, the energy is transferred to another core level electron and causes it to leave its bonded state, which is referred to as the Auger-Meitner effect [133, 134]. In the second process, the energy is emitted as a fluorescence photon [135, 136]. The Auger-Meitner process is depicted in Figure 3.2b. It dominates for atomic numbers $Z \lesssim 30$. The fluorescence process, shown in Figure 3.2c, dominates for $Z \gtrsim 90$. [137]

The kinetic energy of an Auger electron is defined as

$$E_{\text{kin}}([\text{Auger}]) = E_f - E_i - E_{\text{state, Auger}}, \quad (3.6)$$

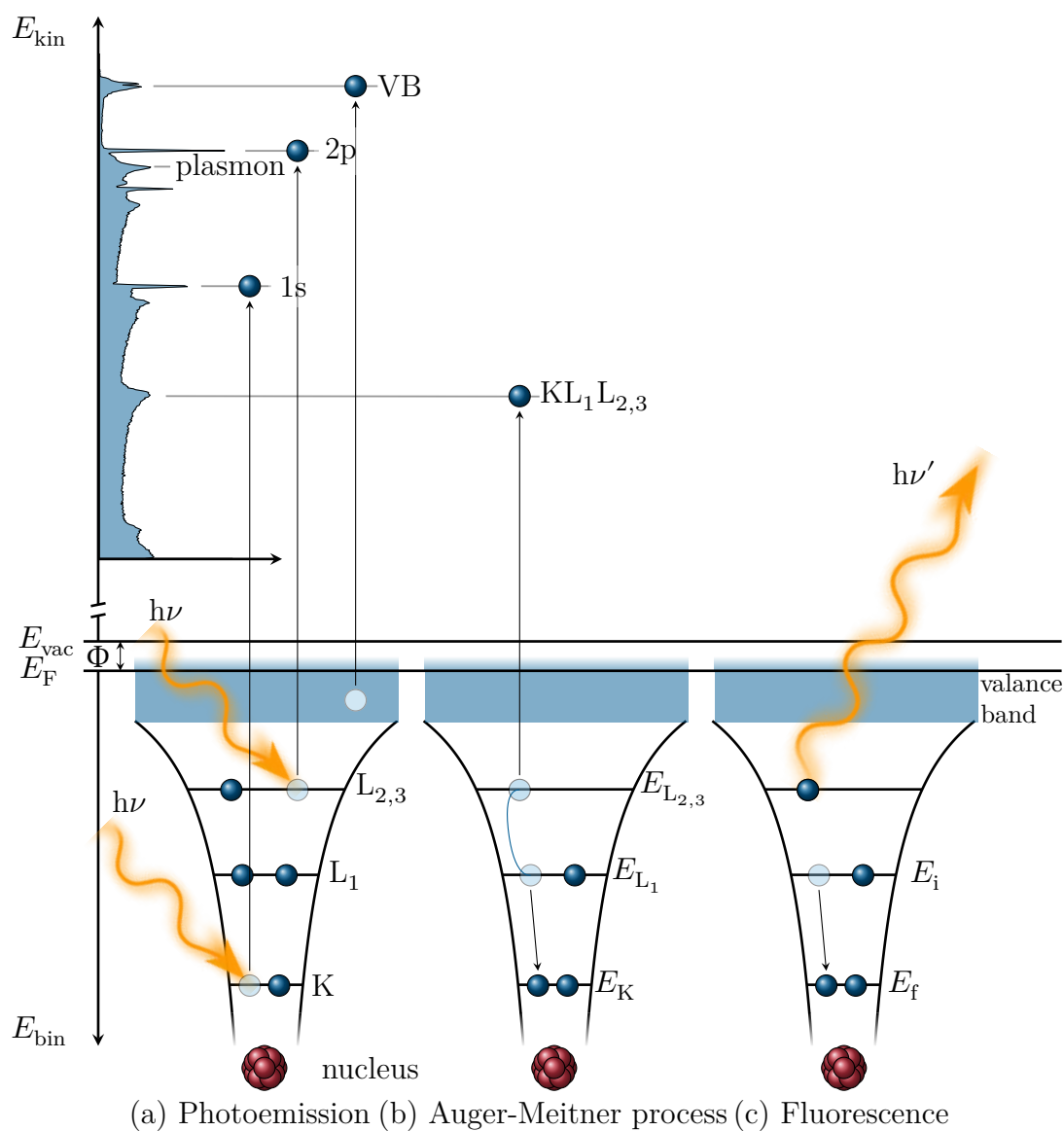


Figure 3.2: Schematic representation of the photoemission (a), the Auger-Meitner effect (b), and fluorescence (c). Incoming photons, represented by wavy orange arrows, excite electrons, indicated by blue spheres, of different energetic levels. A corresponding XPS survey spectrum is depicted on the upper left. (Based on [138, 139])

where E_f , E_i , and $E_{\text{state, Auger}}$ are the energies of the relaxed final state, the initially excited state, and the initial state of the Auger electron, respectively. Thus, the kinetic energy of the Auger electron E_{kin} ([Auger]) is independent of the energy of the incident photon and depends only on the energies of the atomic states. Consequently, the spectral lines of Auger electrons in a PES spectrum can be distinguished from core level signals by varying the photon energy.

Fluorescence photons do not cause any signals in a PES spectrum. Their energy is given by

$$h\nu = E_f - E_i. \quad (3.7)$$

Depending on the radiation's frequency range, a distinction is made between two types of PES, ultraviolet photoelectron spectroscopy (UPS) and x-ray photoelectron spectroscopy (XPS). In the 1950s, XPS was developed independently by the groups of Steinhardt et al. [140] and Siegbahn et al. [141] for general chemical analysis and surface analysis. Since the late 1950s, UPS has become established in solid state research, e.g., for band gap measurements [142].

In UPS, ultraviolet light, e.g., provided by ultraviolet lamps, is used for excitation. It is particularly sensitive to the valence electronic structure, providing information about the density of states and the band structure near the Fermi level.

In XPS, x-rays generated by x-ray tubes are used. The energy distribution in the resulting spectra is suitable for determining the binding energies of electrons in a sample. This enables the identification of chemical elements, their chemical states, and bonds in a sample. Later, synchrotrons became the dominant light source because they provide monochromatic light with tunable frequency, high intensity, and brilliance. A tunable frequency allows the depth sensitivity to be varied and the cross-section to be optimized [138]. In addition, synchrotrons cover most of the frequency range for both XPS and UPS. Because of these advantages, the use of synchrotron radiation has become the standard for producing high-quality XPS spectra. In this work, only XPS was performed, utilizing synchrotron radiation as the sole light source.

Line shape

Theoretically, the well-defined energy levels of electrons in atoms would lead to δ -peaks. However, there are two main reasons why real XPS peaks do have a non-zero width.

The first reason is experimental imperfections, such as the non-zero linewidth of the exciting light, the non-zero angular acceptance of the spectrometer, and temperature effects, as well as structural imperfections of the sample. In XPS spectra, this is visible as a convolution of the initial δ -peak with a Gaussian [143–145].

The second reason for a non-zero width of XPS signals is that core holes have a finite lifetime. After this, such a state is filled by an electron with lower binding energy. The lifetime and the uncertainty in energy Γ are linked by the Heisenberg uncertainty relation. For a typical lifetime in the order of $\tau \approx 1$ fs, this leads to a lifetime broadening of 0.1 eV [132]. In XPS spectra, this is visible as a Lorentzian broadening [146]. To describe the resulting signal, the Lorentzian and Gaussian functions have to be convoluted, leading to the so-called Voigt profile. [147]

Moreover, XPS peaks of metals have an asymmetric line shape with an increased width on the side of lower kinetic energies. This is a consequence of the formation of electron-hole pairs due to core holes being screened by conduction band electrons shortly after they have been generated [116]. A corresponding spectrum can be described by a power law diverging at the position of the initial δ -distribution. Its convolution with a Lorentzian is called Doniach-Šunjić profile. It is characterized by the asymmetry parameter α [148].

Spin-orbit coupling

Spin-orbit coupling (SOC) is the interaction between the spin and the orbital angular momentum of an electron bonded to a nucleus. An atomic state is characterized by the quantum numbers n : principle quantum number, l : orbital angular momentum numbers, and s : spin. In the case of $l > 0$, the spin \vec{s} and orbital momentum \vec{l} are no constants of motion, which is why the total angular momentum $\vec{j} = \vec{l} + \vec{s}$ is introduced. The spin and orbital momentum can be aligned parallel or antiparallel

resulting in $j = l \pm 1/2$ for the total angular momentum quantum number. These two different values cause the splitting of a single level (singlet) into two levels (doublet). The amount of shift in the energy levels, called spin-orbit separation E_{SOC} , mainly depends on the atomic number Z [149]:

$$E_{\text{SOC}} \propto \frac{Z^4}{n^3 l(l+1)}. \quad (3.8)$$

To illustrate the splitting, an artificial Si 2p spectrum is shown in Figure 3.3. For a p-orbital, the quantum numbers $j \in \{1/2, 3/2\}$ exist, corresponding to the levels $p_{1/2}$ and $p_{3/2}$. The ratio of the peak area of split levels is determined by the order of their degeneration. The angular momentum takes values between $-j$ and j in steps of $1/2$, which degenerates each level $2j + 1$ times. As a result, the $p_{1/2}$ level is degenerated 2 times and the $p_{3/2}$ level 4 times, leading to a ratio of $A(p_{3/2})/A(p_{1/2}) = 2$.

The amount of shift between the split levels is quantified by j . Higher values lead to lower binding energies or higher kinetic energies. For the Si 2p doublet, the $p_{1/2}$ level is shifted by $E_{\text{SOC}} = 0.608 \text{ eV}$ in its binding energy with respect to the $p_{3/2}$ level.

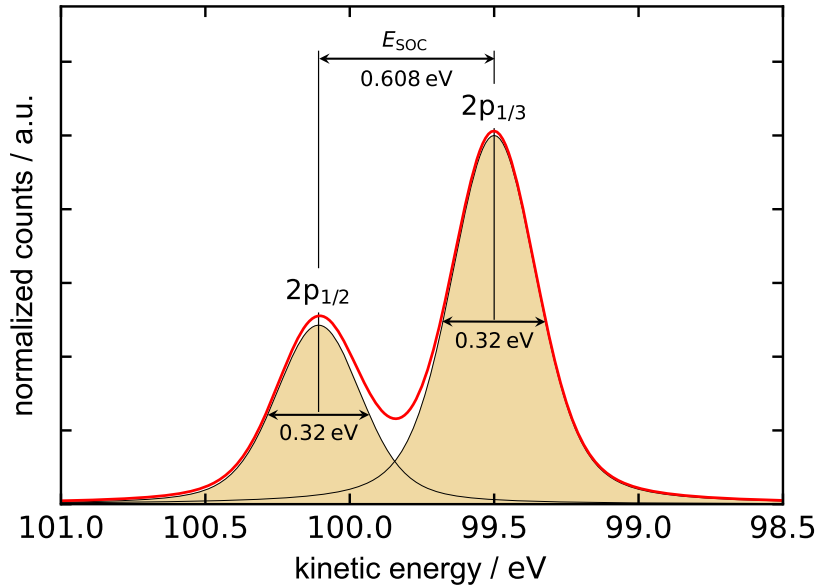


Figure 3.3: Illustration of spin-orbit coupling on the example of an artificial Si 2p spectrum with its split levels $p_{1/2}$ and $p_{3/2}$. (Based on [150])

Angle-Resolved Photoelectron Spectroscopy (ARPES)

To gain additional structural information about a system, angle-resolved photoelectron spectroscopy (ARPES) can be performed. In an experiment, the energy-dependent IMFP also defines the maximum depth from which electrons can leave a sample unscattered, called escape depth. The corresponding depth regarding the surface normal, termed effective depth d_{ef} , determines an experiment's depth sensitivity. It can be adjusted, e.g., by changing the angle between the spectrometer and the sample surface normal, called the polar angle Θ :

$$d_{\text{ef}} = \lambda \cos(\Theta). \quad (3.9)$$

By increasing this angle, the electrons have to travel farther to come from the same depth, making the measurement more surface sensitive. This is depicted in Figure 3.4. Thus, by comparing spectra taken at different angles Θ , the arrangement of layers and elements within a sample can be determined.

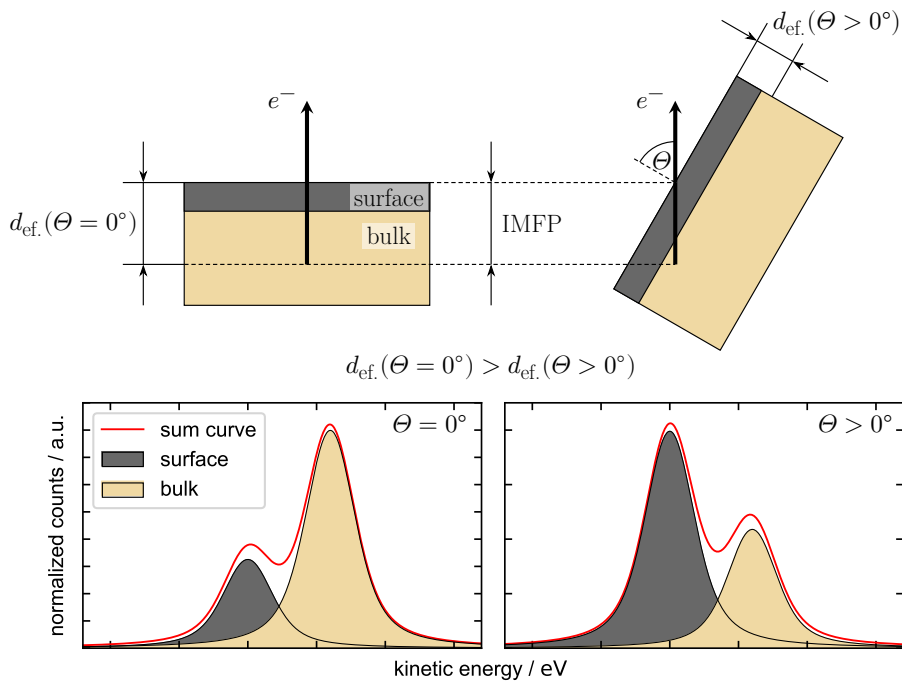


Figure 3.4: Illustration of the principle of angle-resolved photoelectron spectroscopy. On the left side, the angle of measurement is $\Theta = 0^\circ$. A larger angle, as shown on the right, reduces the effective escape depth, resulting in increased surface sensitivity.

Chemical sensitivity

If one atom is bonded to another which has a different binding energy, a shift of the corresponding PES peaks proportional to the relative electronegativity of the bonding partners occurs [151]. This shift is called chemical shift. This effect makes it possible to gain information about the chemical environment of an atom by analyzing its core level signals recorded at high resolution.

Figure 3.5 shows the C 1s spectrum of ethyl-trifluoroacetate as an example. Each carbon atom in this molecule is bonded to different atoms with different electronegativities. Hydrogen has the lowest at 2.1 and fluorine the highest at 4.0 [152]. As a result, four chemically shifted components appear in the corresponding spectrum.

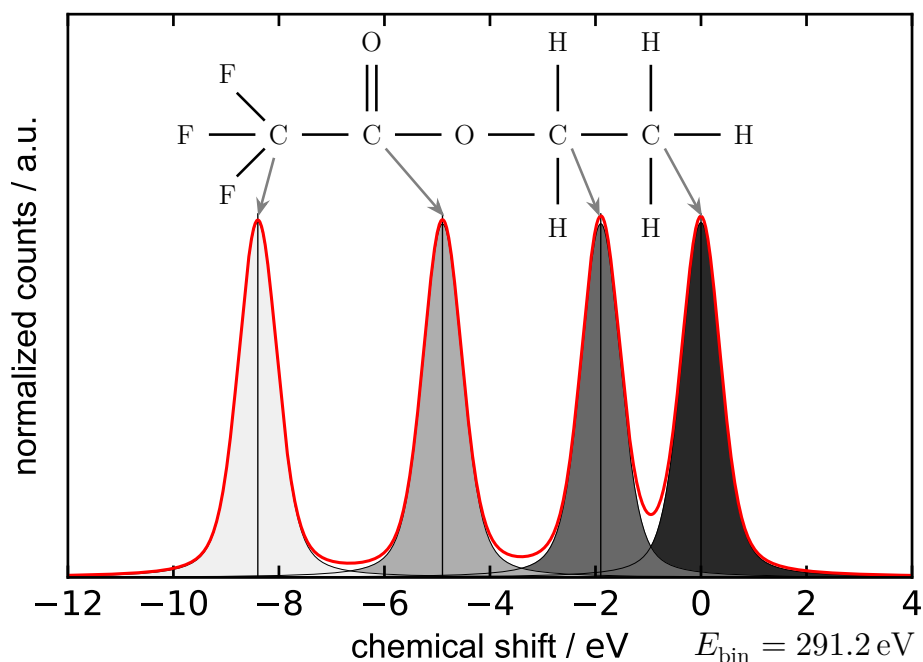


Figure 3.5: Photoelectron spectrum model of the C 1s core level of ethyl-trifluoroacetate. The different chemical environments of the carbon atoms lead to chemically shifted components. [151, 153]

XPS-Data analysis

A full XPS analysis includes survey spectra and high resolution spectra. Survey spectra show a large energy range of several hundred electronvolts. They give an overview of the chemical elements present in a sample, identified by using a suitable database such as that of NIST [154]. Survey spectra can be used, e.g., for rough quantity estimations and to prove a sample's cleanliness by checking for contaminants. High resolution spectra, showing a range of only a few electronvolts, enable an in-depth analysis of individual core level signals regarding chemical bonds. Combined with ARPES, these bonds can be assigned to individual layers.

To identify all components present in a high resolution peak, it must be modeled using a fitting-procedure. Prior to this, the spectrum's continuous background, caused by inelastically scattered electrons and secondary electrons, must be fitted and removed. The simplest estimation of this background is low-order polynomial [155]. However, this is only appropriate for small backgrounds. A better approximation is given by the Shirley- and by the Tougaard-background [156, 157].

The Shirley-background assumes a uniform energy loss function making it suitable for symmetric signals. For asymmetric signals, the Tougaard-background is a convenient approach. It connects the energy loss to the electron's energy and path length traveled in the solid [155]. In practice, a combination of the Shirley- or Tougaard-background with a polynomial one has proved to be a good approach to describe a spectrum's background [158, 159].

For fitting, the LG4X-V2 software was used [160]. It fits both the background and a freely selectable number of profiles. It uses the Marquardt-Levenberg algorithm and performs a least-square fit weighted by the squared count-rate. The quality of the fit is optimized regarding the reduced chi-squared χ^2 . This is given by the sum of the squared differences between the point of the data and the fit divided by the number of free parameters. [161, 162]

3.3 Photoemission electron microscopy (PEEM)

Photoemission electron microscopy (PEEM) is a powerful technique that enables the acquisition of structural, chemical, and magnetic contrast images on a μm -scale in real-time. It is based on mapping the spatially resolved yield of secondary electrons emitted by a sample. These secondary electrons are released by the scattering of photoelectrons. Their high number and low energy compared to primary photoelectrons improve the intensity and quality of PEEM images. The image quality is improved in terms of a lowered aberration and a high immersion factor. To filter for secondary electrons, an aperture is used. Figure 3.6 sketches the part of the electron spectrum transmitted after filtering. This aperture is placed inside an electron-optical lens system that realizes the magnification of the microscope. The different contrast mechanisms of the technique are achieved by using exiting light of a certain energy range, namely ultraviolet light or x-ray light. These two variations are presented below, along with their respective contrast mechanisms. [163]

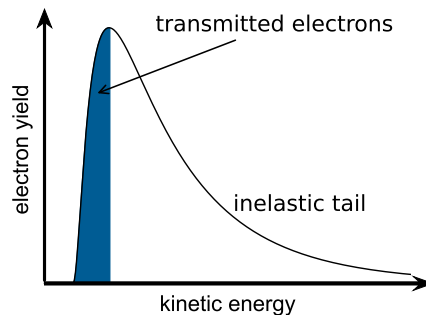


Figure 3.6: Illustration of the yield of secondary electrons in PEEM transmitted by an energetic low-pass filter, usually an aperture. (Based on [113, 164])

3.3.1 Excitation with ultraviolet light

Using ultraviolet light for excitation enables ultraviolet photoemission electron microscopy (UV-PEEM). Typical UV light sources provide photons with an energy only slightly above the work function of many elements. Therefore, only valence band electrons near the Fermi energy are emitted. The small energy dispersion of this variant leads to a particularly good spatial resolution.

Topographic contrast

UV-PEEM provides two contrast mechanisms. The first originates from the sample topography. Electrons leaving the sample surface are accelerated towards the microscope due to a transfer voltage between the sample and the objective lens. This field gets distorted by height differences on the surface. This affects the trajectory of the electrons, which is visible as topographic contrast. In addition, structures on the surface can cause shadowing of surrounding regions. These are not irradiated by the exciting light and appear black in PEEM images. By rotating the sample, shadowing can be distinguished from other effects. An illustration of the topographic contrast is shown on the left of Figure 3.7.

Work function contrast

The second and dominating contrast mechanism for UV-PEEM is the work function contrast. UV-PEEM mainly probes electrons originating from the atoms' valence bands. For these, the rate of emitted electrons, called photocurrent i follows

$$i \propto (h\nu - \Phi)^x, \quad (3.10)$$

with $x = 2$ for metals and $x \in [1, 2.5]$ for semiconductors [146]. Consequently, lower work functions result in higher photocurrents, corresponding to brighter PEEM images. This allows distinguishing regions of a sample surface with different work functions, with the greatest contrast difference for work functions near the photon energy. Different work functions can originate from different chemical elements, different structural features like surface orientation or reconstruction. For example, in the case of SiC, different polytypes and surface reconstructions can be distinguished in PEEM images this way [38, 165]. In this work, this is used, for example, to distinguish between different numbers of graphene layers [166].

This mechanism is sketched on the right of Figure 3.7. If the work function is above the photon energy $\Phi > h\nu$, no electrons are emitted resulting in a dark PEEM image.

In UV-PEEM, the work function contrast is the dominant mechanism. The low electron energy associated with this contrast causes a large IMFP, which would reduce the surface sensitivity. However, since the work function is very sensitive to the surface's properties, UV-PEEM is also very surface sensitive [167].

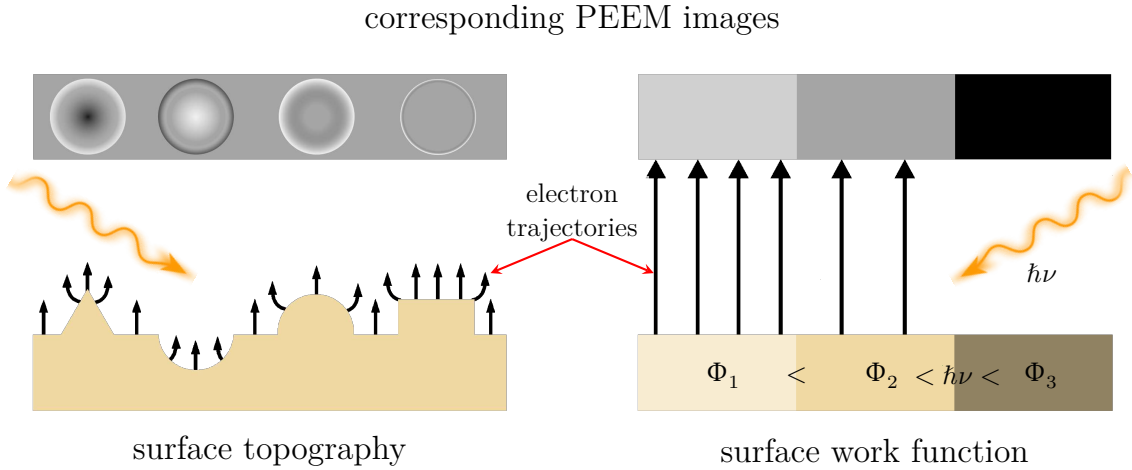


Figure 3.7: Schematic representation of the topographic (left) and work function (right) contrast mechanism in PEEM. The sample's topography leads to altered electron trajectories, resulting in contrast changes in the corresponding regions. The local work function of the sample determines the number of emitted electrons and, thus, the brightness of the associated image region. (Based on [164])

3.3.2 Excitation with synchrotron radiation

Using monochromatic synchrotron radiation during PEEM is called x-ray photoemission electron microscopy (X-PEEM). Depending on the density of states at the Fermi level, here the IMFP is typically in the range of 1 – 10 nm [168]. In addition to topographical contrast, this variant also provides chemical contrast, which is made possible by the excitation of core level electrons. When polarized synchrotron radiation is used, it also provides magnetic contrast. These two additional contrast mechanisms are explained in the following.

Chemical contrast

Chemical contrast can be obtained by exciting core level electrons to empty states near the Fermi energy by x-ray absorption. Subsequently, the generated core level holes are filled by electrons from states with lower binding energy, accompanied by the emission of Auger electrons. Inelastic scattering of these Auger electrons causes cascades of secondary electrons that are imaged by the microscope. The advantage of imaging secondary electrons is, again, their much higher intensity compared to that of the Auger electrons themselves. The chemical contrast is enabled due to the yield of secondary electrons being proportional to the x-ray absorption cross section [169]. Thus, the contrast of X-PEEM images represents the relative local amount of the element emitting Auger electrons at the energy used for the excitation light [163].

A series of X-PEEM images taken at different photon energies can thus be described as a spatially resolved x-ray absorption spectrum (XAS). Summing the number of electrons of either the whole field of view or of specific regions of interest for each of these images and plotting the sums against the photon energies represent XAS spectra. Figure 3.8a shows such spectra of two regions in the X-PEEM image shown in Figure 3.8b. The corresponding sample is a Si substrate covered with an Fe-Ni alloy deposited in squares. While the spectrum of the uncovered substrate has no characteristic features, the one of the covered area clearly reveals the Ni and Fe L_3 absorption edges. However, due to a higher cross section the overall signal intensity of the uncovered area is higher than that of the covered areas. To remove this effect and increase the visibility of the chemical contrast, an image taken at an absorption edge with intensity I_{edge} and one taken a few eV below I_{pre} can be combined like:

$$I = I_{\text{edge}} - I_{\text{pre}}. \quad (3.11)$$

This is done for each image pixel. In the resulting image, the surface concentration of the investigated element is shown isolated, since all other contrast mechanisms are removed. Optionally, the result can further be divided by I_{pre} to remove the effects of possible unequal sample irradiation. This is particularly beneficial due to the striking angle of incoming photons and in case of a large field of view. Figure 3.8c shows a difference image of the Ni L_3 -edge for the previously described sample. [168, 170]

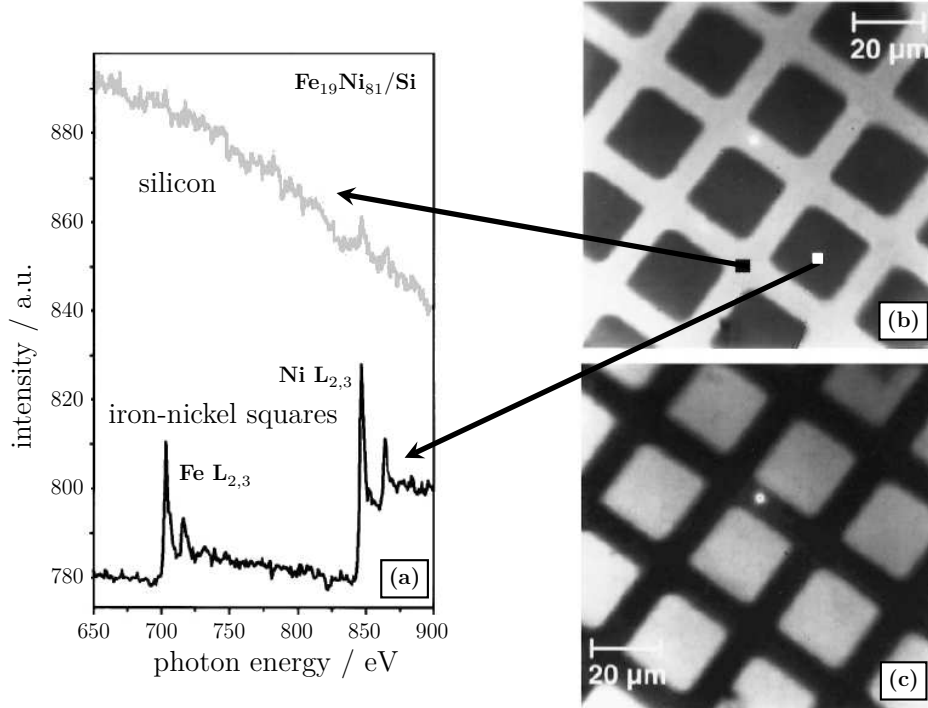


Figure 3.8: XAS spectra (a) of two regions marked in the corresponding X-PEEM image of an iron-nickel alloy deposited in squares on a silicon substrate (b). Difference image for the L_3 -edge calculated after Equation 3.11 (c). [170]

Magnetic contrast

The absorption cross section of a ferromagnetic system irradiated with circularly polarized x-rays depends on the orientation of the system's surface magnetization direction \mathbf{m} with respect to the direction of the photon angular momentum \mathbf{L}_{PH} . This effect is called x-ray magnetic circular dichroism (XMCD) and it enables the magnetic contrast in X-PEEM. [80, 171]

It can be explained by a two-step model sketched in Figure 3.9a for the $L_{2,3}$ transition of a 3d transition metal. In the first step, photoelectrons are excited from the initial states, here the $2p_{3/2}$ (L_3) and $2p_{1/2}$ (L_2) states. Due to the conservation of angular momentum, the photon angular momentum is transferred to the spin of the excited electron, resulting in a spin-polarized photoelectron [172]. For the $2p_{3/2}$ state, left circularly polarized light ($+\hbar$, spin-up photons) preferentially excites spin-up

photoelectrons and right circularly polarized light ($-\hbar$, spin-down photons) prefers the excitation of spin-down photoelectrons. This is reversed for the $2p_{1/2}$ state because of the opposite spin-orbit coupling.

In the second step, the photoelectrons occupy empty 3d states if those with matching quantum numbers are available. As explained in Section 2.2.2, the net magnetic moment in a ferromagnetic material arises from an unequal number of empty states near the Fermi energy regarding their spin. As a result, photoelectrons with opposite spin can occupy different numbers of states. Thus, the final state acts as a "spin-detector" of the spin-polarized photoelectrons. If the sample magnetization \mathbf{m} is parallel to the wave vector \mathbf{k} , there are more empty spin-up states than empty spin-down states. Due to the spin-conservation, photoelectrons originating from the $2p_{3/2}$ ($2p_{1/2}$) state excited by spin-up photons mostly occupy spin-up (spin-down) states above the Fermi edge. Consequently, the absorption of left (right) circularly polarized light is enhanced (reduced) at the L_3 edge and reduced (enhanced) at the L_2 edge. This links the XAS intensity to the sample's magnetization. In summary, the usage of polarized light with an energy corresponding to the absorption edge of a specific element makes X-PEEM an element-specific, magnetic, and surface sensitive technique. [171, 173]

To isolate the magnetic contrast, the difference between two intensity images acquired with opposite helicity, $I^+(E)$ (left) and $I^-(E)$ (right), can be calculated. This results is the so-called XMCD or asymmetry intensity:

$$I_{\text{XMCD}} = I^-(E) - I^+(E). \quad (3.12)$$

Since all other contrast mechanisms, like the topographic contrast, are unaffected by the light's helicity, they are subtracted this way. Normalization by $I^+(E) + I^-(E)$ can further be used, to eliminate the effect of a potential uneven irradiation. The XMCD intensity is proportional to the degree of circular polarization P_{circ} , the strength of the surface magnetization $|\mathbf{m}|$ and to the cosine of the angle between the surface magnetization \mathbf{m} and the incident photons \mathbf{p} , given by $\Theta = \angle(\mathbf{m}, \mathbf{p})$ [80, 175]:

$$I_{\text{XMCD}} \propto P_{\text{circ}} |\mathbf{m}| \cos \Theta. \quad (3.13)$$

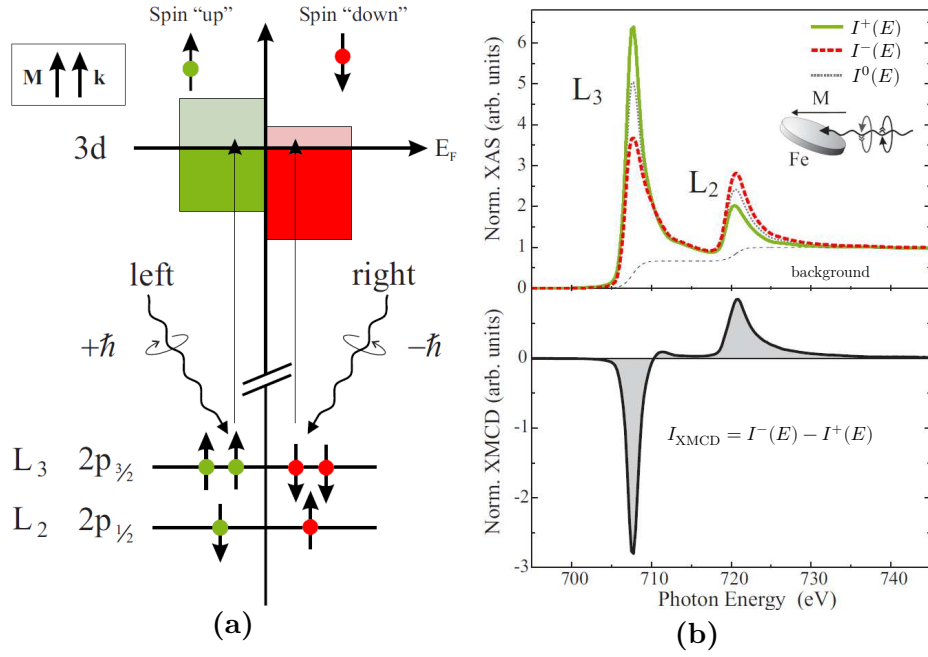


Figure 3.9: Illustration of the XMCD effect at the $L_{2,3}$ edges for a 3d transition metal (a) and the corresponding experimental XAS and XMCD spectra for Fe (b). (Based on [174])

The geometry of the experiment is shown in Figure 3.10. The sample surface represents the xy -plane. The photon direction is fixed and lies in the xz -plane. The angle between the sample surface and the incident photon beam is $16^\circ = 90^\circ - \alpha$. The in-plane and out-of-plane components of the local surface magnetization are represented by m_{\parallel} and m_{\perp} , respectively. The initial azimuthal angle between \mathbf{m} and \mathbf{p} is given by ϕ_0 . For the measurements, the sample was rotated around its normal by ϕ . Therefore, the resulting azimuthal angle of the magnetization direction is $\phi_0 + \phi$. Thus, the vectors are given by:

$$\mathbf{m} = \begin{pmatrix} m_{\parallel} \cos(\phi + \phi_0) \\ m_{\parallel} \sin(\phi + \phi_0) \\ m_{\perp} \end{pmatrix}, \quad \mathbf{p} = \begin{pmatrix} -p \sin(\alpha) \\ 0 \\ -p \cos(\alpha) \end{pmatrix}. \quad (3.14)$$

It follows that:

$$|\mathbf{m}| \cos \Theta = |\mathbf{m}| \frac{\mathbf{m} \cdot \mathbf{p}}{|\mathbf{m}| \cdot |\mathbf{p}|} = -m_{\parallel} \cos(\phi + \phi_0) \sin(\alpha) - m_{\perp} \cos(\alpha). \quad (3.15)$$

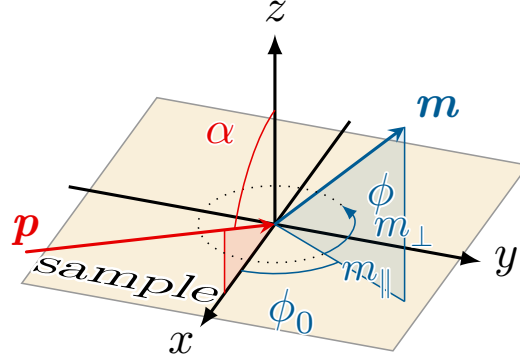


Figure 3.10: Geometry of the experimental setup. Note that \mathbf{p} is shifted in its position compared to Equation 3.14 for better visibility. However, only its orientation is relevant to the analysis.

Defining the proportionality constant in Equation 3.13 as $-k/[P_{\text{circ}} \sin(\alpha)]$ and introducing $\tilde{m}_{\parallel} := km_{\parallel}$ and $\tilde{m}_{\perp} := km_{\perp}$ finally results in:

$$I_{\text{XMCD}} = \tilde{m}_{\parallel} \cos(\phi + \phi_0) + \tilde{m}_{\perp} / \tan(\alpha). \quad (3.16)$$

Combining images recorded at three equidistant angles ϕ , here 0° , 90° , and 180° , leads to an analytically solvable system of equations for \tilde{m}_{\parallel} , ϕ_0 , and \tilde{m}_{\perp} . This equation system is discussed and solved in Appendix B. As a result, \tilde{m}_{\parallel} , ϕ_0 , and \tilde{m}_{\perp} can be determined for each pixel of the field of view. The resulting images can be analyzed, e.g., for the relative strength of the in- and out-of-plane components and for structures.

3.4 Low-energy electron diffraction (LEED)

Louis de Broglie postulated in 1924 the wave nature of matter with its wavelength

$$\lambda_{\text{Brog}} = \frac{h}{p} = \frac{h}{mv} = \frac{h}{\sqrt{2mE_{\text{kin}}}}, \quad (3.17)$$

with the Planck constant h , the particle's mass m , velocity v , and kinetic energy E_{kin} [176]. In low-energy electron diffraction (LEED), this behavior is used to display

the reciprocal lattice of a sample's surface. For this purpose, an electron beam is directed at sample surface under normal incidence. In the case of a crystalline sample, elastically backscattered electrons can undergo constructive interference, which leads to a diffraction pattern, also called Bragg pattern. This pattern reveals the structural periodicity of the uppermost layers of a sample. Thus, LEED provided the first proof for de Broglie's theory in 1927 [177].

The ability to reveal the surface's symmetry in reciprocal space at one glance makes LEED a powerful and widely used technique in surface science. It is perfectly suited for examining sample surfaces for successful preparation.

Depending on the sample system, typical kinetic energies used in LEED are in a range $E_{\text{kin}} = 5 \text{ eV}$ to 200 eV . This corresponds to wavelengths of a few angstroms, making the technique ideal for resolving typical periodicities of crystalline systems [138].

For constructive interference to occur, the Laue condition needs to be fulfilled:

$$\vec{G} = \vec{k} - \vec{k}_0. \quad (3.18)$$

It states, that the momentum transfer, indicated by the difference between the scattered and the incident electron wave vectors $\vec{k} - \vec{k}_0$, needs to be equal to a vector of the reciprocal lattice \vec{G} . Due to the high surface sensitivity, it is sufficient to consider only the components parallel to the surface, given by \vec{k}_{\parallel} , $\vec{k}_{0,\parallel}$, and $\vec{G}_{\text{hk}} = h\vec{a}^* + k\vec{b}^*$. The vectors \vec{a}^* and \vec{b}^* are the reciprocal unit vectors, which correspond to the real space unit vectors \vec{a} and \vec{b} . Spots of a LEED pattern are named by the Miller-indices (h,k). [138]

The Laue condition can be illustrated by the Ewald construction, which can be displayed as a sphere in the reciprocal space intersecting the origin (00), as shown in Figure 3.11 [88, 178]. In three dimensions the reciprocal lattice is constructed by points. In two dimensions, the broken symmetry at the surface in z -direction leads to a degeneration of these points into rods. Where the sphere intersects these reciprocal lattice rods, constructive interference occurs.

The radius of the sphere is defined by $k = |\vec{k}_0| = |\vec{k}| = 2\pi/\lambda_{\text{Broglie}}$. In the case of backscattering, as present in LEED, this leads to the angle between the incident and

diffracted beam being proportional to λ_{Brog} and anti-proportional to E_{kin} . Therefore, the spots move towards the center when increasing E_{kin} . Only the (00) spot is fixed, since it originates from the direct reflection of the electron beam.

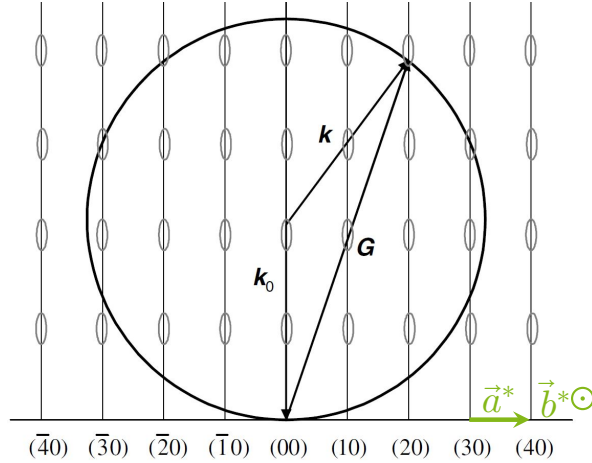


Figure 3.11: Ewald construction for two dimensional scattering. Energy and direction of the incident and the scattered electron are indicated by \vec{k}_0 and \vec{k} , respectively. As indicated by the reciprocal lattice vector \vec{G} , a (20) reflex results from this. The intensity modulation of the rods in real experiments is indicated by ellipsoids. [88]

Patterns of reconstructions or superstructures directly display the Brillouin zone of the reciprocal lattice. Therefore, the real space periodicity of the unit cell can be calculated from LEED images. To describe these pattern the Wood notation can be used. As an example, the description $(\sqrt{6} \times \sqrt{6}) R30^\circ$ is used for a structure that has a real space vector length of $\sqrt{6}$ times the length of the substrate's and which has a unit cell rotated by 30° with respect to the substrate. The relative position of the atoms of a reconstruction or superstructure compared to those of the substrate cannot be determined by the position of the diffraction spots. Therefore, their intensity modulation has to be used as predicted by scattering theory [179]. One reason for this modulation is, that in the real LEED experiment incoming electrons reach into the first few atomic layers of the solid. Because of that, it is not strictly two dimensional, but represents an intermediate situation between the two and three dimensional situation. This causes an intensity modulation in the rods of the Ewald construction. Together with multiple scattering effects, this is used for structural analysis during IV-LEED [178].

Chapter Experimental setup

4

This chapter introduces all experimental setups used for sample preparation and measurements in this study. These are the CCS and the UV-PEEM setup at TU University, the PASG setup at PTB Braunschweig, the XPS system at DELTA, and the X-PEEM system at BESSY, all located in Germany.

4.1 Ultra-high vacuum (UHV)

A high-quality vacuum is necessary to preserve the samples' surfaces from contamination and other changes on the one hand and to enable electron-based measurements on the other. According to the kinetic theory of gases, the rate of particles from the gas phase impinging on a surface is proportional to the pressure. Under simplified assumptions, it takes atoms from the gas phase approximately 1 h to form one monolayer on a surface at a pressure of 10^{-9} mbar. Since a typical measurement takes about that long, the need for good vacuum becomes clear. Such a good vacuum is called Ultra-high vacuum (UHV). It is defined as a pressure of $p < 10^{-8}$ mbar. The usage of low-energy electrons and soft x-rays also requires good vacuum conditions. Otherwise, their mean free path would be far too small for any practical applications. [138, 180]

To reach such low pressure, combinations of different pumps are used. Starting from atmospheric pressure, scroll pumps are used to lower the pressure to $p_{\text{FV}} = 10^{-3}$ mbar, which is called fore-vacuum. Subsequently, turbo-molecular pumps decrease the pressure to a high vacuum in the region of $p_{\text{HV}} = 10^{-7}$ mbar. From there, a back-out procedure is required to further reduce the pressure. For this, the complete chamber is heated up for several days in order to increase the vapor pressure of the adsorbates

on the inner walls of the setup. As a result, their desorption rate is increased and they can be evacuated by the pumps way faster [180]. Temperatures used in this work range from 150 – 180 °C, depending on the components' limitations. After this, pressures of about $p_{\text{UHV}} = 10^{-10}$ mbar are reached. Lastly, further pumps, like titanium sublimation pumps and getter pumps, help to increase the pumping rate even further and are also advantageous because they are vibration-free. For specific experiments, this can be crucial for focusing.

4.2 Setups for the silicon carbide preparation

In the following, the setups for CCS and PASG are introduced in sequence. The CCS setup is shown in Figure 4.1. Its vacuum system consists of a turbo-molecular pump connected to a scroll pump. With it, a pressure of 1×10^{-8} mbar is achieved after 16 h for pumping without bake-out. For preparation in inert gas, the pumps are sealed off from the rest of the chamber by a gate valve and argon is let in through an inlet valve. The sample is placed in a graphite crucible (CTG GmbH), which can be heated inductively by a water-cooled copper coil connected to a heating station. It has been shown that a low temperature gradient across the sample surface improves the resulting reconstruction quality. To achieve a low gradient, the crucible is centered regarding the coil while the sample is positioned in the middle of the crucible by placing it on a spacer with $h_{\text{S}} = 4.6$ mm height. Concerning the usage of inductive heating, only the crucible must be heated by the eddy currents. To prevent heating the rest of the chamber, a quartz dome, which is electrically insulating, is used as part of the vacuum chamber surrounding the crucible. However, since the maximum operating temperature of quartz is about 1000 – 1200 °C and annealing the crucible up to $T \approx 1500$ °C is necessary, there must be no contact between these two components. This is ensured by mounting the crucible on a binder-free hexagonal boron nitride (*P100*, Henze BNP) platform, which is electrically insulating and resistant far beyond the required temperatures. Further details on the design can be found in [113, 181].

The silicon atoms' sublimation rate strongly affects the prepared samples' quality. A low rate results in a more homogeneous reconstruction and can be accomplished

by sealing the crucible with a graphite cap that has a small bore with a diameter of $d = 1$ mm. This bore is the only way for evaporated silicon atoms to leave the crucible. Thereby, the silicon partial pressure around the sample is increased, resulting in the desired reduction in sublimation rate. [23]

The heating station (*HS-4*, Ultraflex) is a resonant circuit consisting of an induction coil as inductivity L , the so-called tank capacitor C , and the resistance R given by the crucible. The power supply (*SMT-5/200*, Ultraflex) provides an alternating current with a frequency of $f = 77$ kHz. Due to the skin effect, such a high frequency is required to achieve high efficiency regarding the power absorbed by the crucible [182, 183]. All samples were prepared with a maximum power of $p = 2$ kW, which heats the crucible to a temperature of $T \approx 1500$ °C. As a reference for preparation, the temperature of the graphite crucible was measured as a function of the heating power. For this purpose, a pyrometer (*IMPAC[®] IGA 6/23 Advanced*, LumaSense Technologies GmbH) was used.

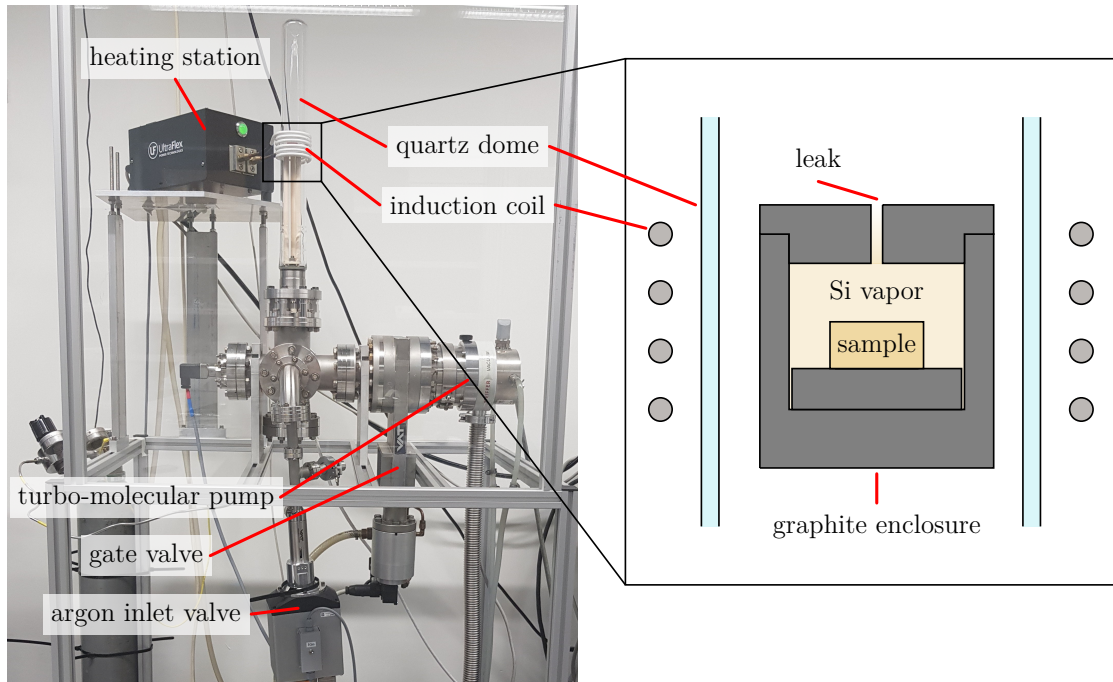


Figure 4.1: Setup for the CCS preparation of the silicon carbide at TU University (left) and schematic representation of the sample inside the graphite crucible, surrounding quartz dome, and inductive coil (right; based on [23]).

4 Experimental setup

The setup is mostly the same for the CCS and the PASG method. The setup used to conduct the PASG method is depicted in Figure 4.2. There are a few minor differences compared to the CCS method. First, the temperature is measured during each preparation and the heating power is adjusted to control it. Second, additional valves are connected for the inlet of different gases. These are necessary, e.g., for the hydrogen etching.

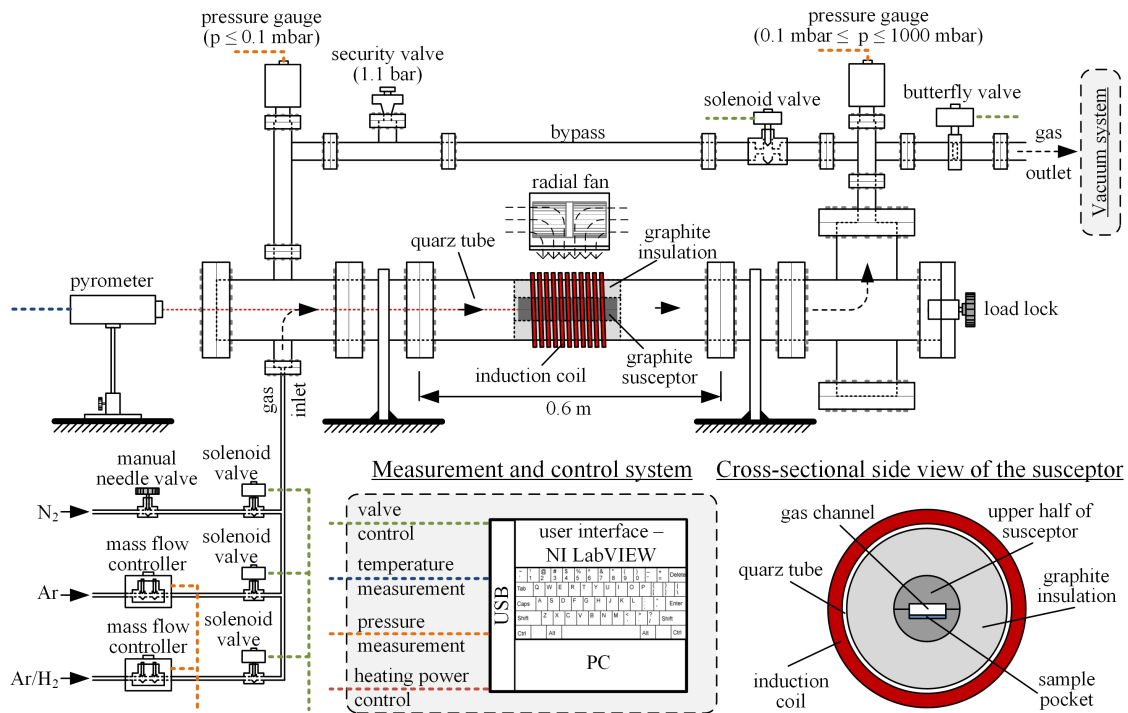


Figure 4.2: Schematic representation of the setup used for the PASG preparation located at the PTB Braunschweig [70].

4.3 Analytic equipment

Three different experimental setups were used for sample analysis. Those are a laboratory-based UV-PEEM at TU Dortmund University, Germany, the XPS endstation at beamline 11 at DELTA, Dortmund, Germany, and the X-PEEM system PEEM-III at the UE49-PGM beamline at BESSY II, Berlin, Germany. All measurements were carried out at room temperature.

4.3.1 UV-PEEM at TU Dortmund

The vacuum chamber containing the UV-PEEM at TU Dortmund University is shown in Figure 4.3. It consists of two parts: A preparation chamber and a PEEM chamber.

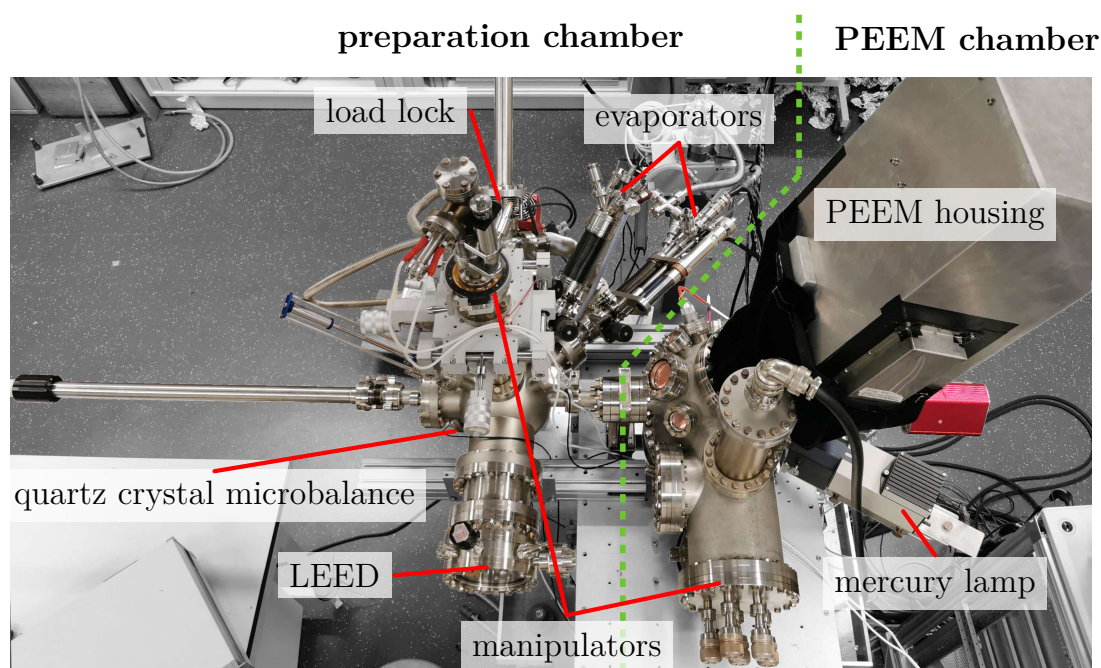


Figure 4.3: Vacuum chamber containing the UV-PEEM at the TU University. The system consists of two parts, visually separated by a green dashed line. The left part is equipped for sample preparation including a LEED system. The right part houses the PEEM and all further required components.

The UV-PEEM (*PEEM 350-20*, STAIB Instrumente GmbH) is combined with a mercury short arc lamp with a cut-off energy of $h\nu = 4.9\text{ eV}$, which illuminates the sample at an angle of 30° . This setup has a lateral resolution of $0.2\text{ }\mu\text{m}$ and provides work function and topographic contrast [164].

The microscope contains four electrostatic lenses, an objective lens, an intermediate lens, and two projective lenses. These are used for focusing, magnification, and adjusting the projected image's size, respectively [184]. Electrons leaving the sample surface are accelerated towards the microscope due to a transfer voltage of $U_{\text{Tr.}} = 11.4\text{ kV}$ between sample and objective lens. In the microscope, the trajectory of the electrons is affected by the fields of the lenses while passing through them. Each lens is constructed of three electrodes. The potential of the outer two is fixed to $U_{\text{Tr.}}$, which prevents strayfields. Especially for investigating magnetic samples, this is advantageous. The potential of the middle electrode can be varied to adjust the focal point of the corresponding lens. Furthermore, an aperture acts as an energetic low-pass filter. A stigmator consisting of octupole lenses is used to minimize axial astigmatism. At the end of the lens system, a micro-channel plate (MCP) amplifies the signal and a phosphorous screen converts it to a light optical image digitized by a CCD camera (*pixelfly QE*, PCO GmbH). The lens system is surrounded by a μ -metal shielding, shielding from the influence of external magnetic fields due to its high magnetic permeability. The setup is depicted in Figure 4.4. To minimize stray light, the microscope and the camera are covered by an aluminum housing. A five-axis manipulator enables exact positioning of the sample under the microscope.

The PEEM chamber is pumped by an ion pump, a titanium sublimation pump, and a turbomolecular pump backed with a scroll pump. Since the first two are vibration-free, only they are switched on during measurements to improve the image quality. With this pumping system, a base pressure of $1 \times 10^{-10}\text{ mbar}$ is reached.

The preparation chamber is equipped for sample annealing and coating. To achieve reproducible sample coating with platinum and cobalt, two electron beam evaporators (*EFM 3* and *EFM 3T*, FOCUS GmbH), a quartz crystal microbalance (*QO 40A1*, PREVAC sp. z.o.o.) with the corresponding thickness monitor (*TM14*, PREVAC sp. z.o.o.), and a precise four-axis manipulator were used. To reach the sample temperature necessary for intercalation, a sample holder was used that allowed direct resistive heating. It represents a modified version of the sample holder, described

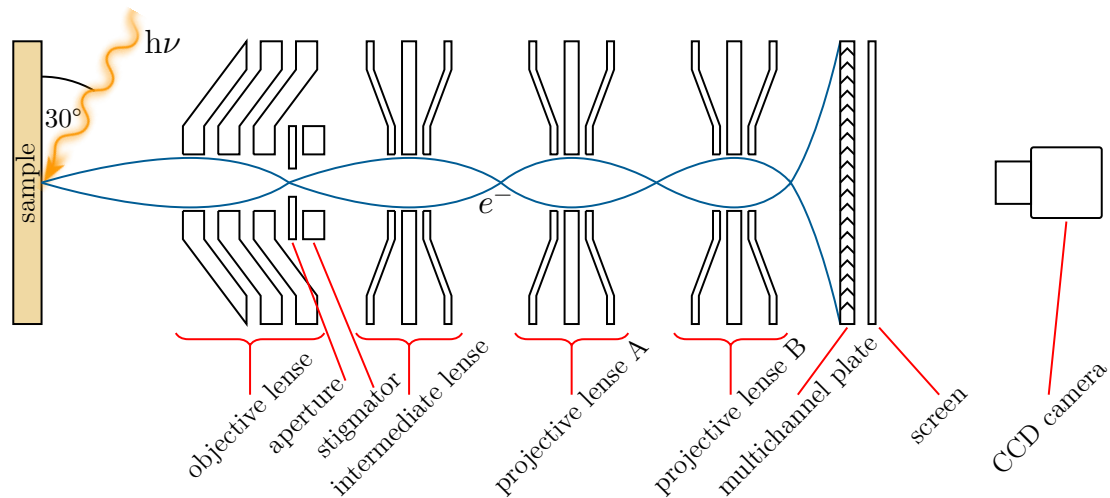


Figure 4.4: Sketch of the UV-PEEM system with the illuminated sample, the lens system influencing the electrons trajectory, and the components for image amplification, visualization, and digitization. (Based on [113, 164])

in detail in [185]. The sample is mounted with its left and right sides connected to one of the clamping contacts of the sample holder. A photo of the sample holder can be seen in Figure 4.5. In this work, it has been shown that direct resistive heating is a much more reliable method when compared with others, such as electron bombardment. This is most likely due to the lower pressure during the heating or the more controllable sample temperature or even both. The temperature was controlled using an infrared pyrometer (*IMPAC[®] IGA 6/23 Advanced*, LumaSense Technologies GmbH) calibrated with a type N thermocouple.

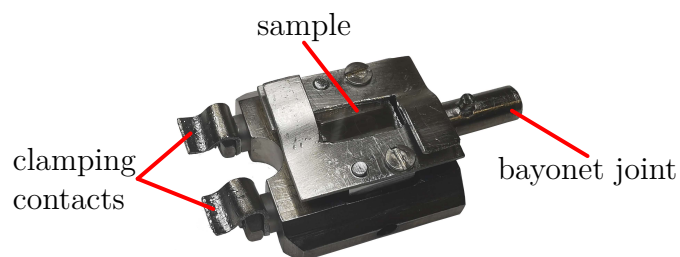


Figure 4.5: Sample holder used for UV-PEEM measurements.

A turbomolecular pump combined with a scroll pump is used for pumping the preparation chamber, thus achieving a base pressure of 1×10^{-10} mbar. In addition, this chamber is connected to a load lock and contains a LEED system.

LEED system

Structural investigations were carried out using a 4-grid LEED system (*ErLEED 150*, SPECS Surface Nano Analysis GmbH), sketched in Figure 4.6. It uses an electron gun with a thoria-coated iridium hairpin cathode. Inside this gun, electrons are accelerated to a defined energy E_{kin} , tunable in the range of 0 – 3000 eV. For focusing, a lens system and a Wehnelt cylinder are used [186]. After impacting the sample surface, the backscattered electrons have to pass through a grating system to be detected. This system acts as an energy filter so that inelastically scattered electrons cannot pass through it. Further, the two outer grids, as well as the sample, are grounded to shield the retarding field originating from the inner grids from the sample and from the fluorescent screen placed behind the grid system. The electrons that pass the grids are accelerated onto the screen due to it being at a potential of 6 kV. This amplifies the resulting optical image, which is digitized by a camera in the final step. The entire setup is surrounded by a μ -metal shielding.

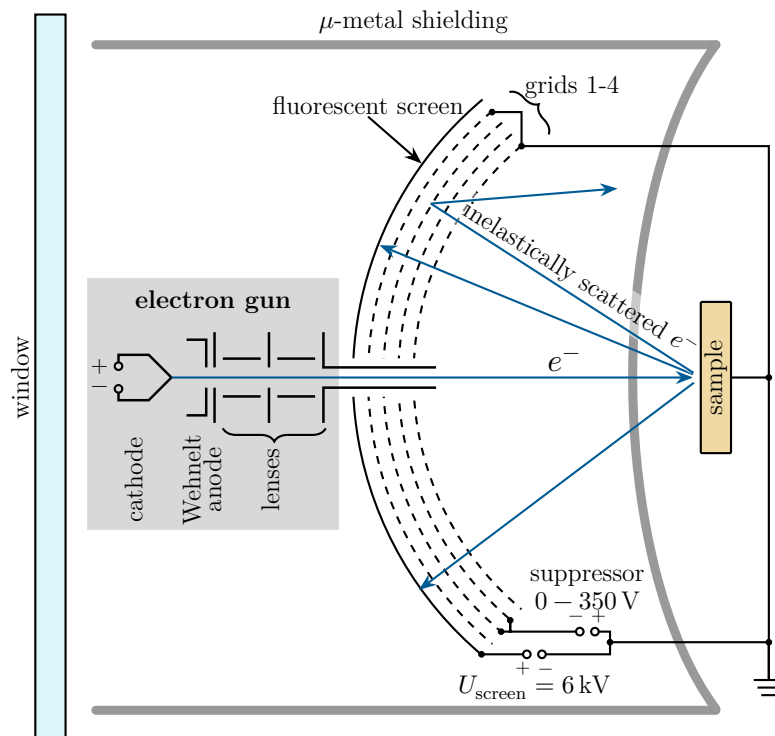


Figure 4.6: Schematic representation of the LEED system used. (Based on [187])

4.3.2 XPS setup at DELTA

The XPS setup used in this work is located at the endstation of beamline 11 (BL11) of the electron storage ring DELTA, Dortmund, Germany. The facility accelerates electrons up to an energy of 1.5 GeV and provides a maximum current of $I = 130$ mA. Beamline 11 is one of the soft x-ray beamlines at DELTA and uses the undulator U55. The alternately oriented magnets of the undulator continuously accelerate the electrons in such a way that they move on a wiggling trajectory and emit synchrotron light, also called Bremsstrahlung, in the direction of the electron beam. The energy of this radiation is freely tunable in the range of 50–1500 eV [188]. The radiation intensity is maximized by adjusting the strength of the undulator's magnetic field [189]. After being emitted, the radiation is filtered by energy by passing through a plane-grating monochromator. Subsequently, it is focused onto the sample with a spot size of $(70 \times 30) \mu\text{m}^2$.

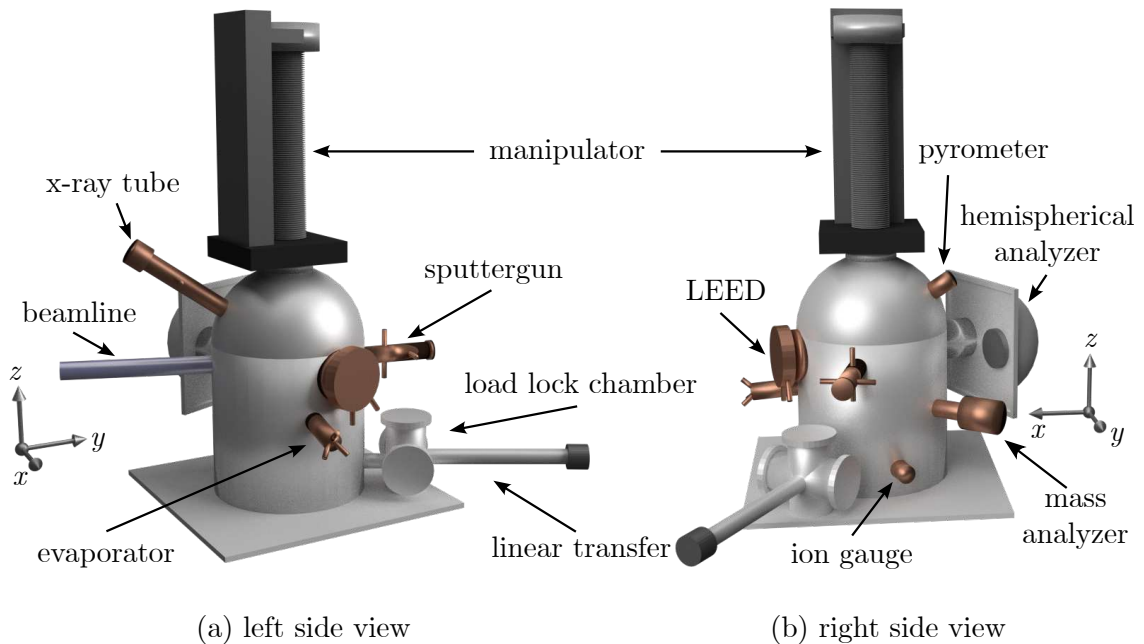


Figure 4.7: Schematic representation of the UHV chamber containing the setup for XPS, consisting of the beamline connection, the manipulator, and the hemispherical energy analyzer. [139]

The chamber housing the spectrometer is shown in Figure 4.7. It is made of μ -metal, preventing the influence of external magnetic fields, and is connected to a load lock for sample insertion. The setup is equipped with the same evaporators and

pyrometer as the UV-PEEM setup, ensuring easy preparation reproducibility. To verify successful preparation, LEED was performed using the same model used in the UV-PEEM chamber. A five-axis manipulator is used for sample positioning. With the chambers pumping system, a base pressure of $p = 5 \times 10^{-11}$ mbar is reached.

The sample holder used is shown in Figure 4.8. By mounting the sample between two tantalum half shells contacted to sliding copper contacts, direct resistive heating is enabled. In this application, one of the three contacts is redundant.

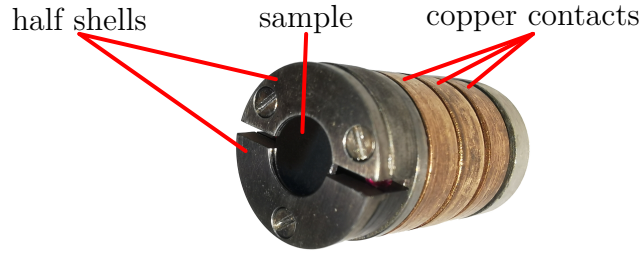


Figure 4.8: Sample holder used for XPS measurements.

During XPS measurements, the sample is grounded to avoid electrostatic charging. The spectrometer is grounded as well, whereby the measured kinetic energy is only affected by the work function of the analyzer Φ_A and not by that of the sample Φ_S :

$$\begin{aligned} E_{\text{kin}} &= h\nu - E_{\text{bin}} - \Phi_S + (\Phi_S - \Phi_A) \\ &= h\nu - E_{\text{bin}} - \Phi_A. \end{aligned} \quad (4.1)$$

To measure the energy-resolved XPS spectra, a hemispherical energy analyzer (*CLAM IV*, VG Microtech; HEA) is used. This spectrometer consists of an electrostatic lens system, an energy analyzer sphere, and a detector, as sketched in Figure 4.9. After the synchrotron radiation impinges on the sample surface, photoelectrons of different energies leave the surface in all directions. Those within a narrow cone of the acceptance angle Θ_{HEA} are accelerated into the spectrometer by a transition field provided by the first lens. After being focused, the electrons pass through an entrance slit, are decelerated by a retarding field, and enter the analyzer. Thereby, the field enables the energy selectivity of the instrument. During the measurement, its strength is varied to cover the desired energy range of the electrons. Inside

the analyzer, an electric field between its hemispheres influences the trajectory of the electrons. Consequently, only electrons with energy within a small specific range $E_{\text{pass}} \pm \Delta E$, around the so-called pass energy E_{pass} , will pass through the entire analyzer and be measured by the detector. The width of this energy range is defined by the energy resolution ΔE [126, 190, 191]. Variable exit slits with diameters of 0.5 – 5 mm allow to vary the energy resolution. However, it should be noted that a higher resolution leads to a lower signal intensity. A one-dimensional channeltron detector with nine channel electron multipliers (CEM) amplifies the passing electrons by a factor of $10^6 - 10^8$ [192].

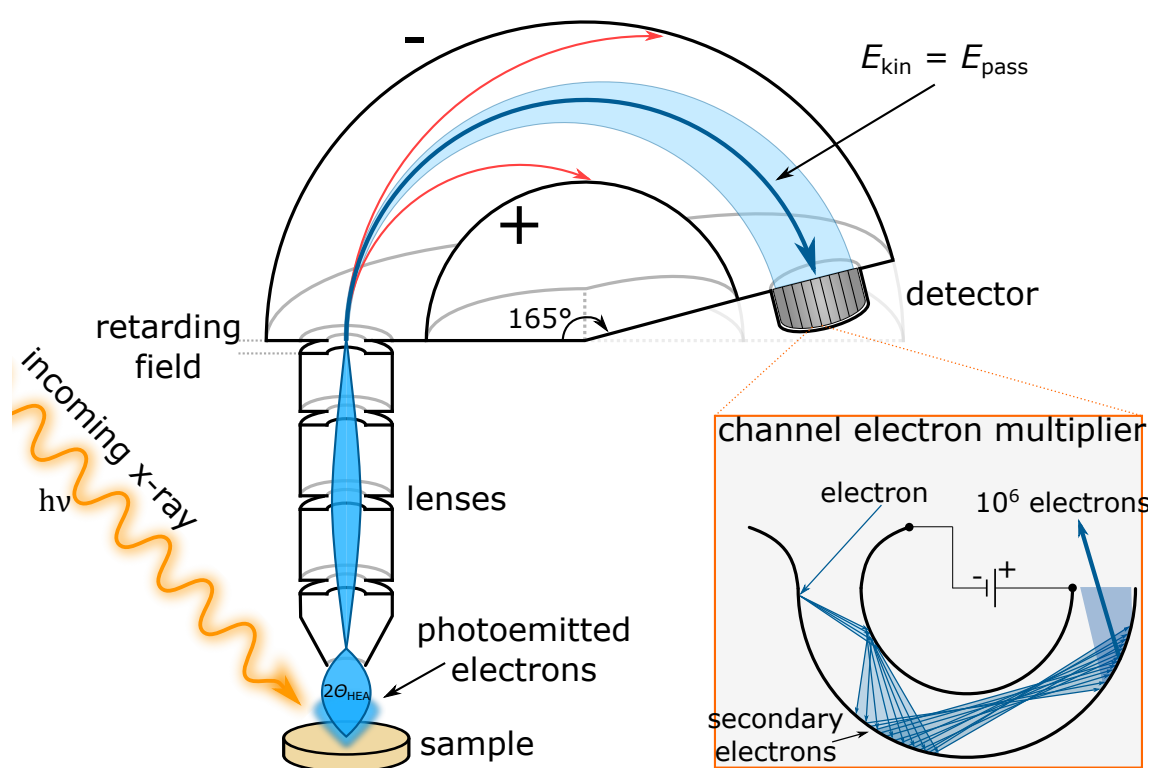


Figure 4.9: Schematic representation of the XPS spectrometer. [139, 190].

During measurements, polarization effects of the exciting radiation distort the measured counts of electrons. This effect is minimized by the instrument being mounted to the UHV chamber at approximately 54.7° relative to the synchrotron beam, which is the so-called magic angle α_{magic} [193].

4.3.3 X-PEEM setup at BESSY II

The magnetic contrast PEEM images were acquired with the X-PEEM (*PEEM-III energy microscope*, Elmitec Elektronenmikroskopie GmbH) equipped with an energy analyzer placed at the UE49-PGM beamline at the BESSY II, Berlin, Germany. This storage ring produces electrons with an energy of 1.7 GeV at a current of 300 mA. Operating in top-up mode, where the beam current is kept constant, enables easy combination and comparability of microscopy images. At beamline UE49, an Apple II-type undulator generates synchrotron radiation with full polarization control. A plane-grating monochromator filters the radiation by energy, which is freely tunable in the range of 80 – 1800 eV. The generated beam impacts the sample at a grazing angle of incidence of 16° and with a spot size of $(10 \times 20) \mu\text{m}^2$. [194]

The experimental chamber contains of two parts, a preparation chamber and a PEEM chamber, as shown in the lower panel of Figure 4.11. Using of several turbomolecular pumps backed with scroll pumps, a base pressure of 1×10^{-10} mbar is reached in both parts. The preparation chamber is connected to a load lock and equipped with electron beam evaporators, a quartz crystal microbalance, and a four-axis manipulator suited for sample annealing. A standard ELMITEC sample holder was used, shown in Figure 4.10. It allows sample temperatures of up to 600°C by applying electron bombardment. The temperature was measured with a pyrometer.

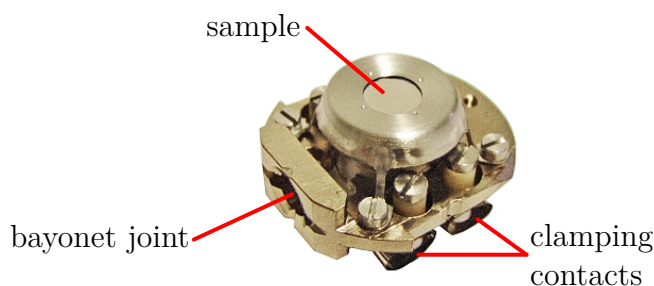


Figure 4.10: Sample holder used X-PEEM investigations. [195]

The second part contains the PEEM, which is optimized for synchrotron radiation, has a lateral resolution of 30 nm, and is combined with a suitable sample manipulator. This chamber part rests on a solid granite block and is spring-loaded to minimize vibrations. A sketch and a photo of the microscope are shown in the top and bottom

panels of Figure 4.11, respectively. Similar to the UV-PEEM, the microscope uses a lens system, an MCP, and a screen. In addition, a semicircular energy analyzer enables the energy sensitivity of the system, which, alongside PEEM, enables to perform XAS and XPS measurements with spatial resolution. In order to change the energy under investigation, a retarding field is used in front of the analyzer. A mercury short-arc lamp also allows for UV-PEEM images to be taken.

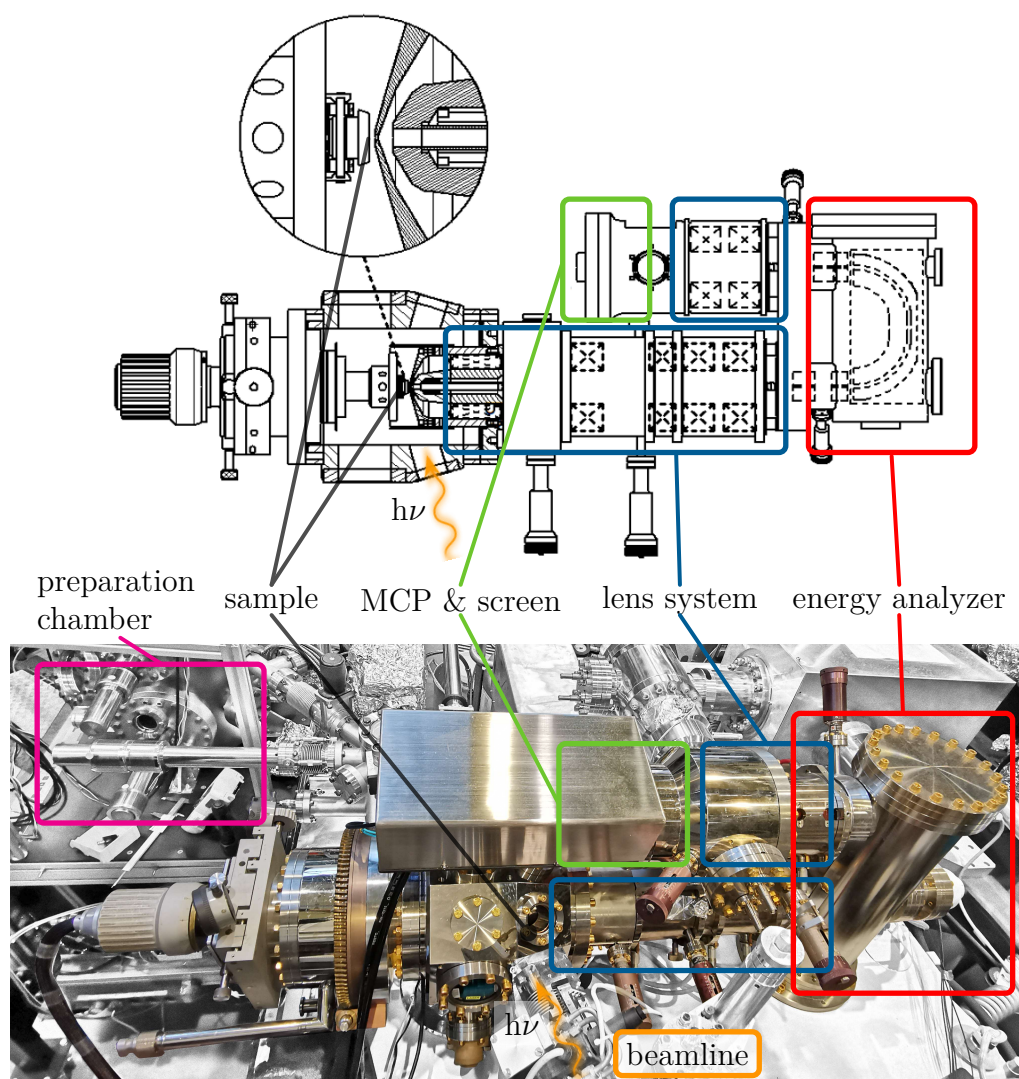


Figure 4.11: Sketch (upper panel; [195]) and photo (lower panel) of the X-PEEM system used, consisting of the lens system, energy analyzer, MCP, and screen. The sample is located in front of the lens system. To the left and right of it, the preparation chamber and beamline are respectively connected.

Chapter Sample Preparation

5

The following chapter presents the two steps of sample preparation. First, the preparation of the buffer layer reconstruction of SiC using the CCS as well as the PASG method is described. Second, the coating and intercalation of these samples, first with platinum and afterward with cobalt, is explained.

5.1 Silicon carbide preparation

Homogeneous large-area and single-domain growth of the ($6\sqrt{3} \times 6\sqrt{3}$) R30° surface reconstruction of SiC was achieved by applying the CCS method [23] as well as by applying a variation of it, a modified PASG technique [70]. The CCS and PASG methods were conducted at TU University, Dortmund, and at Physikalisch-Technische Bundesanstalt, Braunschweig, respectively.

All samples prepared by the CCS method were cut from on-axis 4H-SiC (n-type) wafers from Cree, NC, USA, which had been chemically-mechanically polished (cmp) and had an epi-ready (0001) surface. Samples prepared by the PASG method were cut from on-axis 6H-SiC (n-type) a small miscut wafer of -0.03° towards the primary flat was used.

Before sublimation, all wafers were cleaned and annealed. The cleaning process started with an ultrasonic bath in acetone, followed by isopropanol for 10 min each. In order to remove oxide contaminations from the surface, samples prepared by CCS and PASG were handled differently due to the different possibilities of the respective setups. For CCS-samples, a 5 min dip in 5% hydrofluoric acid (HF) was performed [196]. Samples prepared by PASG were cleaned by hydrogen etching [22].

The etching was carried out in the corresponding chamber with a gas mixture of 5 % hydrogen and 95 % argon at a pressure of 1 bar and a temperature of either 1200 °C or 1400 °C maintained for 15 min [70].

In the following, the two types of preparation are described.

Confinement controlled sublimation (CCS)

During CCS, first degassing was carried out in a vacuum with a base pressure below 2×10^{-8} mbar at 700 °C for 3 h. In the next step, Si sublimation was conducted in an inductively heated graphite crucible in 900 mbar Ar at 1500 °C for 30 min, leading to the $(6\sqrt{3} \times 6\sqrt{3})$ R30°-reconstruction [23]. Varying the pressure and the temperature changes the sublimation rate of the silicon atoms and affects the formation of the reconstruction. To yield a single-domain reconstruction of mostly buffer layer over a large area, a slow sublimation rate together with a high carbon mobility is needed. The parameters were optimized so that only one domain appeared in the LEED patterns and only very small graphene monolayer stripes were observed at step-edges in the PEEM images. The height and width of the steps are some nm and several μm , respectively [38, 197].

Polymer assisted sublimation growth (PASG)

The PASG method uses the same principle as the CCS method, but in between the ultrasonic bath and the hydrogen etching prior to the sublimation, the sample surface is covered with a polymer serving as an additional carbon source. The polymer used in this work is the photoresist AZ5214E, which is a Novolac based thermosetting phenolic resin [70]. It is composed of hexagonal carbon rings and OH groups, which are known to crosslink at higher temperatures. Sample coating was carried out by spin-deposition with a spinning rate of 6000 rpm, held for 30 s [198]. While spinning, two droplets of the polymer diluted with isopropanol at a volume ratio AZ(μL)/IPA(mL) of 3.4 were dropped onto the surface.

The parameters of the PASG setup are slightly different from those of the CCS setup. For initial annealing, the base pressure was 1×10^{-6} mbar and the sample

temperature was 400 °C. During this step, the polymer decomposes and amorphous carbon clusters remain on the surface. Subsequently, buffer layer growth was carried out at 1450 °C for 10 min at an Ar pressure of 1 bar. Thereby, the carbon clusters act as seeds for the formation of a graphene layer and minimize the mass transport of carbon atoms, which normally contributes to step bunching and monolayer growth at the step edges. During this step, the clusters also connect and form a complete layer. Different from the CCS setup, samples were vented continuously with argon during sublimation at a flux of 20 sccm.

Since both setups were fully automated, samples could be prepared with very high reproducibility [70, 199]. Regardless of the preparation method, subsequently, the samples were inserted into another vacuum chamber and annealed at 550 °C for 3 h before coating and intercalation.

5.2 Sample coating and intercalation

The coating of the sample surfaces was accomplished by physical vapor deposition (PVD) with electron beam evaporators, such as the one shown in Figure 5.1. During this process, the evaporant is heated utilizing electron bombardment to the point where it evaporates. Therefore, a high voltage is applied between the material and a filament, which is used as an electron source. A water-cooled copper cylinder surrounds these parts and keeps the outer temperature low to prevent a sharp rise in pressure during evaporation. A collimator and a shutter allow for focusing the beam of evaporated material and controlling the deposition time, respectively. The evaporant can be used in the form of granules placed in a crucible or in the form of a rod, depending on the material to be evaporated. The use of granules is necessary when the material's melting point is below the temperature required for evaporation. Otherwise a rod can be used. This results in a lower rise in pressure because the heating energy can be focused more accurately and thus kept lower. Both cobalt and platinum were used in the form of rods. For platinum, this is absolutely necessary. The temperature required for evaporation is so high that only molybdenum, tantalum, and tungsten can be considered as materials for a crucible [200]. Unfortunately, all these metals are known to form alloys with platinum [201–203]. Cobalt was used in the form of a rod because its high stiffness makes it very easy to handle.

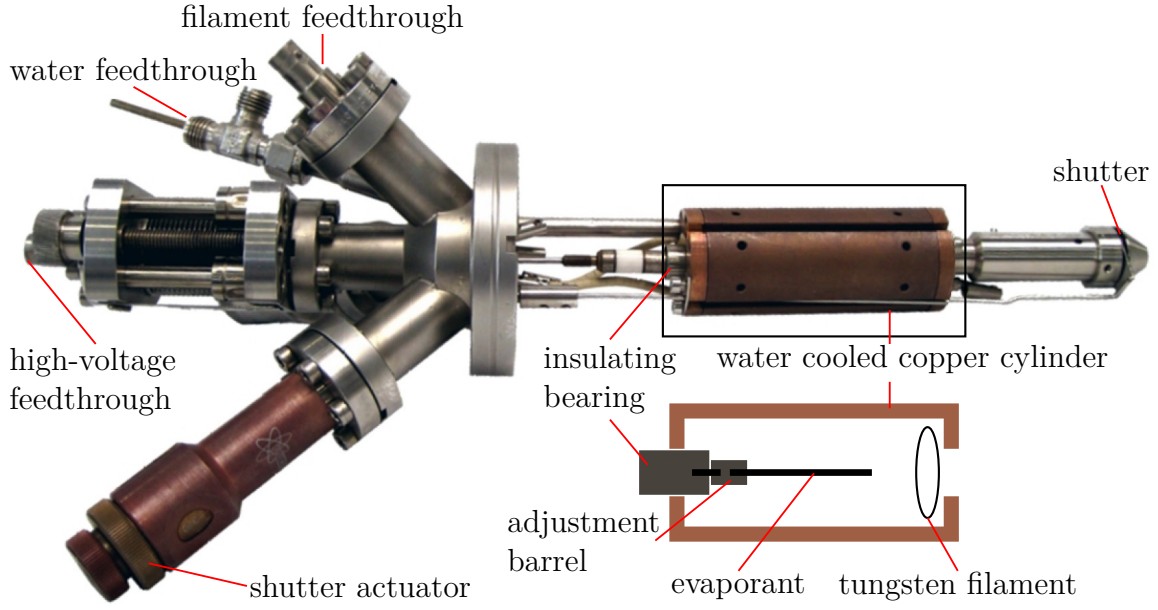


Figure 5.1: Image of an electron beam evaporator and schematic of the cooling cylinder and its inner parts. [204]

During metal deposition, all samples were kept at room temperature. The deposition rates were determined using a quartz crystal microbalance. This device indirectly determines the thickness of a deposited film by measuring the change of the oscillating frequency of quartz crystal Δf due to a deposited mass Δm [205]. The heating powers applied and resulting deposition rates are:

$$p_{\text{Pt}} = U_{\text{H}} \cdot I_{\text{H}} = 4.5 \text{ kV} \cdot 3.3 \text{ mA} = 14.85 \text{ W}, \quad t_{\text{Pt}} = 0.025 \frac{\text{\AA}}{\text{min}},$$

$$p_{\text{Co}} = U_{\text{H}} \cdot I_{\text{H}} = 1.5 \text{ kV} \cdot 7.5 \text{ mA} = 11.25 \text{ W}, \quad t_{\text{Co}} = 0.38 \frac{\text{\AA}}{\text{min}}.$$

The Pt-film thickness was chosen to be 4 Å. During this work, it has been shown that this thickness is sufficient to decouple the graphene from the substrate completely. The Co-film thicknesses of 1.5 nm, 2.4 nm, and 3.4 nm were selected. These are thick enough to form a complete layer after intercalation. Furthermore, for a film thickness of at least 3.0 nm, the magnetic domains cover several terraces [38]. For thicknesses greater than 4.0 nm, strong PMA is not expected [16].

Chapter Results and Discussion

6

This chapter presents the analysis results. First, a systematic and comprehensive preparation series was carried out to determine the annealing temperatures required to induce the intercalation of Pt and Co. During this series, the sample surfaces were studied by UV-PEEM, as shown in Section 6.1. These reveal the topography of the graphene and prove the homogeneity of the deposited metal films.

In the second step, LEED and XPS were used to analyze the structural and chemical properties of the system. Each layer of the system arranges itself in a crystalline structure, as shown by LEED in Section 6.2. Such long-range order is a great advantage regarding the magnetic properties. Structural inhomogeneities would also disturb the formation of magnetic features. The results of the XPS analysis are presented in Section 6.3. They show the presence of quasi-freestanding graphene, proving successful intercalation. In addition, cobalt silicide remained absent, indicating that the Pt-layer effectively functions as a diffusion barrier, as desired. Lastly, two silicon carbide surface components appeared, attributed to the uppermost substrate layers being in a changed Coulomb environment after Pt intercalation.

Finally, the magnetic structure of the embedded Co-layer was investigated using X-PEEM in combination with XMCD at the Co L_3 -edge [80, 171]. Corresponding results are discussed in Section 6.4. For all samples analyzed, numerous vortices and anti-vortices were detected across the whole layer. The overall magnetization was found to be predominantly in-plane. Thus, the different vortices are merons, anti-merons, and bimerons. Neither defects nor the stepped layer structure were found to affect the magnetic structure significantly. However, it was found that the Co-layer thickness, the flatness of the initial substrate reconstruction, and additional annealing steps influence the overall magnetic structure, its homogeneity and the number of vortices within the system.

6.1 Ultraviolet photoemission electron microscopy

To determine the temperatures needed for successful Pt- and Co-intercalation and to check for homogeneity of the deposited metal films, UV-PEEM was used. After examining the bare buffer layer on SiC, it was covered with Pt and systematically annealed and investigated until the intercalation appeared. Subsequently, this was repeated with Co. The temperatures initiating intercalations were determined by running preparation cycles consisting of a 5 min annealing step and the recording of a PEEM image (exposure time of 4 s). Subsequent preparation cycles started with a 10 °C increase in annealing temperature compared to the previous cycle. A series of resulting images showing each state of the preparation is presented in Figure 6.1.

The PEEM images of the $(6\sqrt{3} \times 6\sqrt{3})$ R30°-reconstruction of SiC are characterized by lines, as shown in Figure 6.1a. These lines indicate step edges of the substrate, resulting from the unavoidable miscut angle of the substrate. Besides the buffer layer, which is present on the terraces, an additional monolayer of graphene accumulates as thin strips at the step edges. Due to their higher work function compared to buffer layer, they show a darker contrast. These stripes form while the first carbon layer is still spreading over the surface during sublimation, making them unavoidable for the preparation of a complete reconstruction layer [22, 38]. Increasing the preparation time or temperature would cause this monolayer to spread across the terraces, typically indicated by a wavy edge. Furthermore, additional graphene layers would start to form, which are characterized by darker contrasts in the PEEM images due to their higher work function compared to buffer layers and monolayer graphene [206].

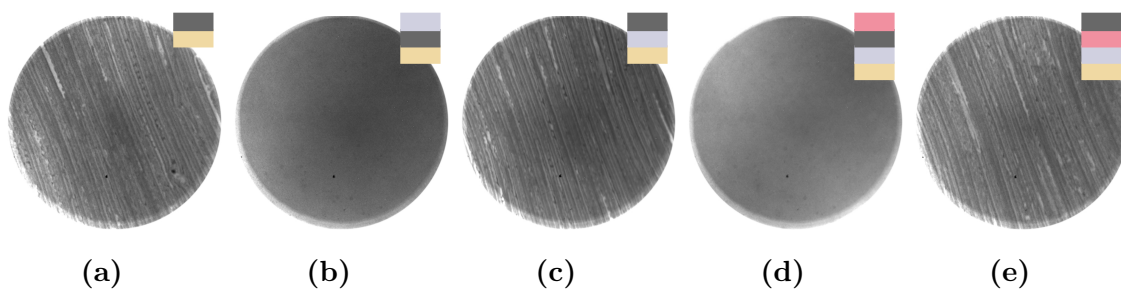


Figure 6.1: UV-PEEM images of the as-prepared buffer layer (a), after 4 Å Pt coverage (b), after annealing at 720 °C (c), after 2.6 nm Co coverage (d), and after annealing at 325 °C (e). Sketches in the upper left of each image depict the preparation state. Colors indicate: Graphene, SiC, Pt, and Co. (FOV 220 μm)

After metal deposition, all step edges and terraces are covered by an amorphous metal film that obscures the substrate's structure in the PEEM images. This observation holds true for all investigated samples, even for the thinnest Pt-film of 2 Å, which corresponds to an estimated coverage of approximately one monolayer. Thus, the metals seem to cover the surfaces very homogeneously. Images after the deposition of 4 Å Pt and 2.6 nm Co are shown in Figures 6.1b and 6.1d, respectively.

During the Pt-preparation cycle, the first noticeable change in the PEEM image occurred at 550 °C. After annealing at this temperature, the step structure becomes visible again. However, the steps appear quite blurred, as shown in Figure 6.2. This indicates a structural change in the amorphous Pt-layer. It most likely becomes flatter by wetting on the surface, preferably at terraces [207] or additionally by melting at the surface [208]. As a result, the topography of the Pt-layer becomes more similar to that of the stepped substrate while still being on top of the buffer layer. Further investigations are required to describe this process precisely. The next change occurred after annealing at 700 °C, which is shown in Figure 6.1c. After this annealing step, the surface looks like the initial bare buffer layer. These results are consistent with those of Xia et al. [72]. No further changes occurred after annealing at 900 °C, the highest temperature applied in this study.

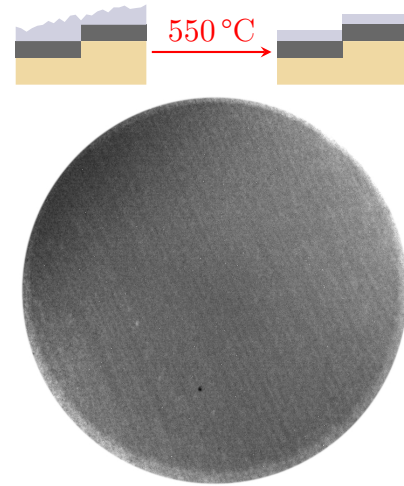


Figure 6.2: UV-PEEM image of a sample after 4 Å Pt deposition and subsequent annealing at 550 °C. The sketch at the top illustrates wetting of the Pt on the surface. Colors indicate: Graphene, SiC, and Pt. (FOV 220 μm)

Regarding the Co-preparation cycles, an annealing temperature of 325 °C was determined to initiate intercalation for all Co-layer thicknesses investigated, which is in excellent agreement with the results of Hönig et al. [38]. This final state of the preparation is shown in Figure 6.1e. To avoid structural changes due to Si-diffusion into the Co-layer, Co-diffusion into the substrate, or reorientation of the Co-atoms [209], no annealing temperatures above 325 °C were applied.

6.2 Low-energy electron diffraction

In this chapter, the structure of each of the system's layers is analyzed by means of LEED, beginning with the pattern of the prepared SiC surface reconstruction, shown in Figure 6.3. Next to two sets of hexagonally ordered spots originating from the substrate and the graphene, a variety of spots caused by the $(6\sqrt{3} \times 6\sqrt{3})$ R30°-reconstruction are visible. The individual spot-brightnesses within this image are characteristic of different numbers of graphene layers, as analyzed by Riedl et al. [62]. The spots marked with green circles next to the graphene spot, being slightly brighter than the graphene spot itself, indicate that a small amount of monolayer graphene is present. This monolayer represents the stripes at the step edges, as mentioned in Section 6.1.

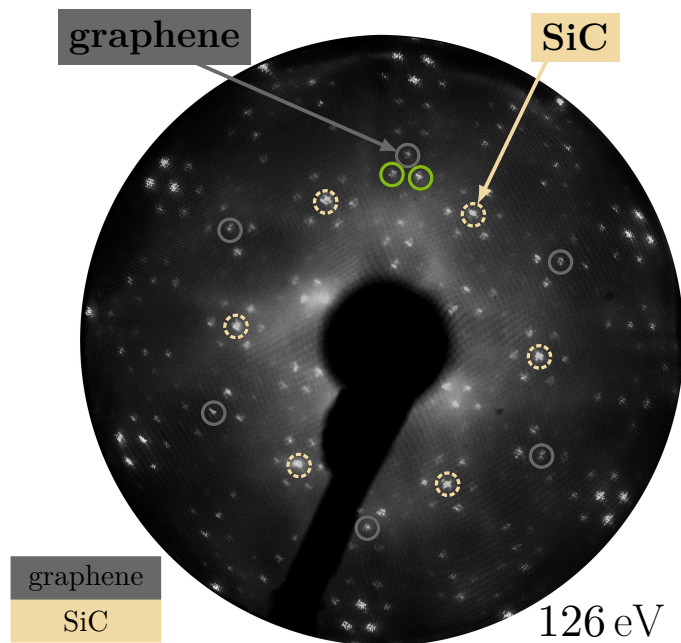


Figure 6.3: LEED pattern of a pristine sample, showing the $(6\sqrt{3} \times 6\sqrt{3})$ R30°-reconstruction on SiC. LEED-spots of graphene and SiC are marked in gray and yellow, respectively. Furthermore, two spots indicating a small amount of monolayer graphene on top of the reconstruction are marked by green circles. [40]

After deposition of only 4 Å Pt, the LEED pattern disappears completely, indicating a homogeneous and non-periodic coverage. Subsequently, the samples were annealed. In contrast to the results gathered by PEEM, using LEED, no changes were observed after annealing at 550 °C. This supports the assumption that the changes visible via PEEM after this heating step are due to wetting, as this only affects the smoothness of the deposited layer. The first change in the LEED patterns occurred at a temperature of 700 °C, which is in line with the PEEM results. After annealing at this temperature, the hexagonally ordered graphene and SiC spots reappeared. Simultaneously, the $(6\sqrt{3} \times 6\sqrt{3})$ R30°-reconstruction remained absent, indicating decoupling and partial lifting of the carbon layer. Thus, the buffer layer became quasi-freestanding graphene. In addition, a $(4\sqrt{3} \times 4\sqrt{3})$ R30°-reconstruction regarding the SiC pattern appeared, which is assigned to the intercalated Pt-layer. It is indicated by a prominent spot near each graphene spot and six hexagonal spots around each SiC spot. At a temperature of $T_{\text{Pt}} = 720$ °C, these spots became significantly more pronounced, while no further changes were found up to temperatures of 900 °C. For this reason, all samples were annealed at T_{Pt} to induce the intercalation of Pt. An image after the interaction of Pt is shown in Figure 6.4.

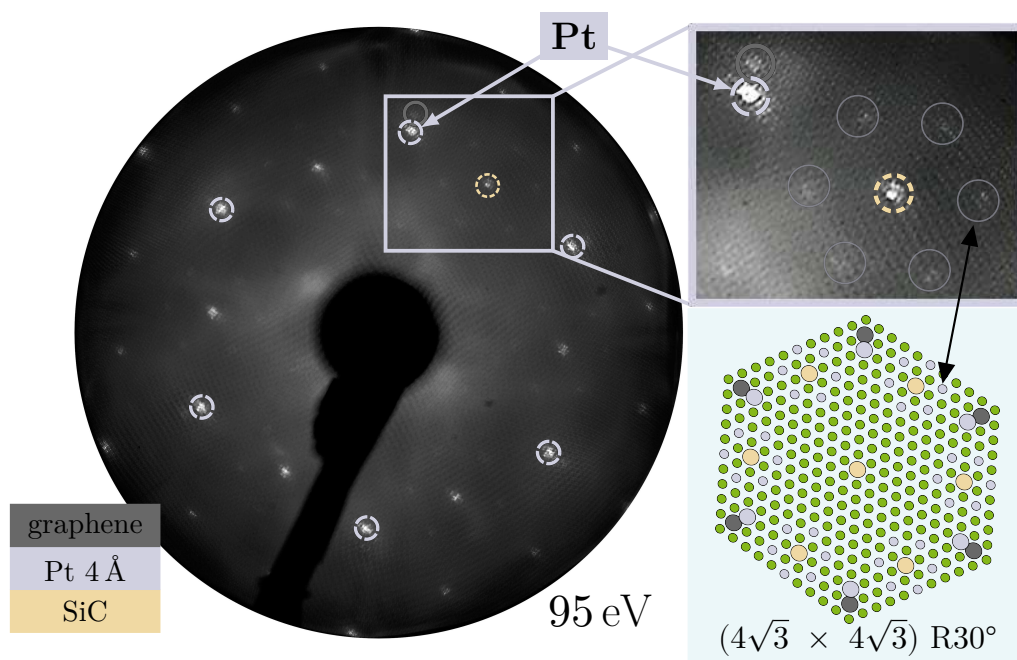


Figure 6.4: LEED pattern of the sample system after intercalation of 4 Å Pt. A $(4\sqrt{3} \times 4\sqrt{3})$ R30°-reconstruction appears, associated to intercalated Pt.

These results agree with those reported by Xia et al. [72]. However, in the present study, additional spots surrounding each SiC spot were found, which allowed identification of the superstructure. This difference can be explained by the increased Pt-layer thickness used in the present work. Also, the electron kinetic energy of $E_{\text{kin}} = 95 \text{ eV}$ used to record the LEED image corresponds to a slightly larger mean-free path. Within the present study, improved spot sharpness and brightness were found due to the increased layer thickness and increased mean-free path of electrons.

More structural properties of the Pt-layer were detected using confocal laser scanning microscopy (CLSM). CLSM is a depth-sensitive method with spatial resolution for imaging a sample's reflectivity [210]. Figure 6.5 shows a CLSM image of a sample after intercalation of 8 \AA Pt. Three different contrasts are visible: dark, medium, and bright, marked blue, orange, and green. These most likely represent regions with one, two, and three layers platinum, respectively. Their presence shows that platinum does not form one layer after the other, but several layers form simultaneously. Remarkably, the bright areas have a hexagonal shape, reflecting the structure found by LEED. The different contrasts and hexagonal features disappear after Co deposition and remain absent after its intercalation. This can be explained by the increased depth in which the Pt-layer is then located. In addition, some bright, round features with a blurry edge are observed. One is marked by a black circle. Such a blurry edge indicates features being on top of the sample surface. Therefore, these show platinum remaining on the surface even after annealing. Such defects were also visible in the X-PEEM images, as shown later in this work.

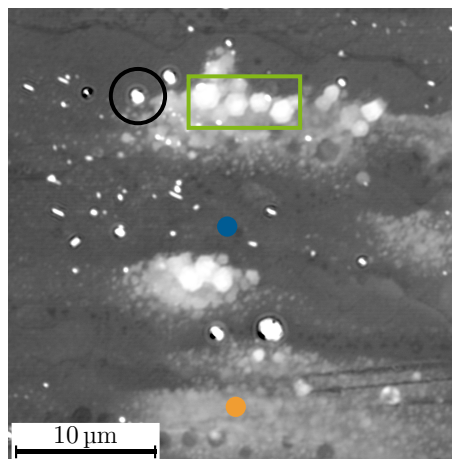


Figure 6.5: CLSM image of a sample after intercalation of 8 \AA Pt. Three different contrasts are present. These are associated with one, two, and three layers Pt, marked blue, orange, and green, respectively. Moreover, a surface defect is circled in black.

In the final phase of the preparation, Co deposition leads to the disappearance of the pattern, as already observed during Pt-deposition. Consistent with the PEEM observations, an annealing temperature of $T_{\text{Co}} = 325 \text{ }^\circ\text{C}$ was found to be sufficient to cause spots to reappear for all Co-layer thicknesses investigated. Figure 6.6 shows the LEED pattern of a sample after depositing 2.4 nm Co and subsequent annealing. Two sets of hexagonally ordered spots appeared, associated with graphene and Co. The Co-pattern is rotated by 30° with respect to the graphene pattern and has a lattice constant that matches that of Co in hcp-structure [209]. Spots of the Pt-layer and the substrate did not reappear due to the relatively thick Co-layer. The reappearance of graphene spots after annealing indicates that Co has successfully been intercalated. This is also confirmed by the bright appearance of the graphene spots compared to the cobalt spots.

To avoid Si diffusion through the Pt- and Co-layers and to keep Co in an hcp-lattice structure [209], higher temperatures were not used in this preparation phase. However, this relatively low temperature results in the Co spots not being very sharp. This is likely due to limited long-range order, which would also affect the system's magnetic properties. The same spots were visible in the LEED images for all Pt- and Co-layer thicknesses investigated.

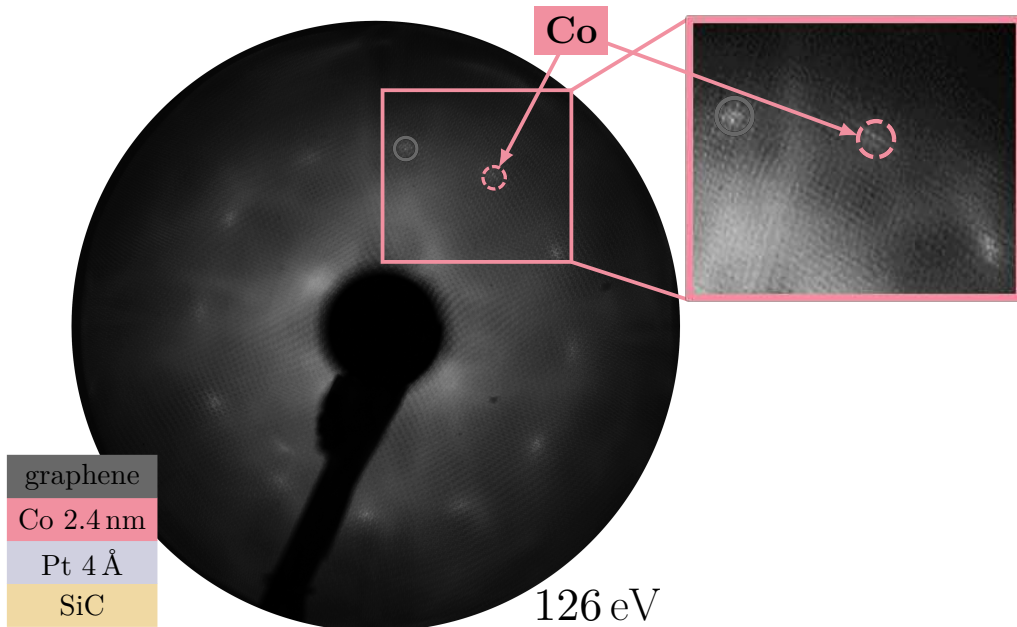


Figure 6.6: LEED pattern of the sample system after intercalation of 2.4 nm Co. A $(1 \times 1) R30^\circ$ -reconstruction appears, associated with the intercalated Co-layer.

6.3 X-ray photoelectron spectroscopy

The following presents XPS spectra of a sample intercalated with 4 Å Pt and subsequently 3 nm Co.

The chemical composition of the sample was verified by XPS survey spectra. The spectra were recorded at normal emission, i.e., at an emission angle of $\Theta = 0^\circ$ and with a photon energy of $h\nu = 700$ eV. The upper panel of Figure 6.7 shows a spectrum taken before any metal deposition. Characteristic peaks of the Si 2s, Si 2p, and C 1s orbitals, related plasmon-loss features, and two Auger signals are indicated. After intercalation, signals of the Pt 4d, Pt 4f, and Co 3p orbitals, along with the Pt OOO-Auger signal, emerged, as shown in the lower panel of Figure 6.7.

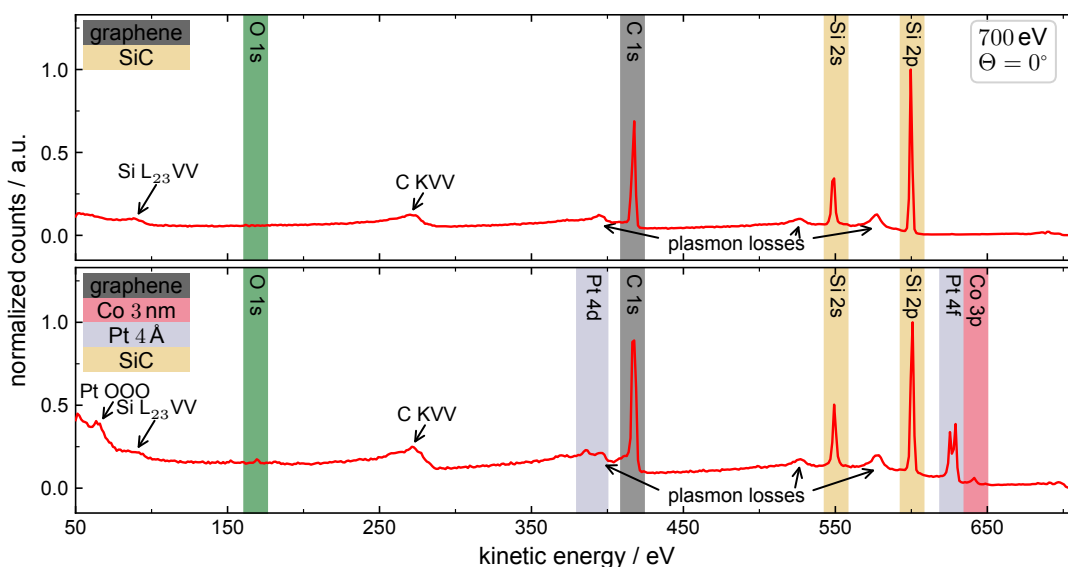


Figure 6.7: XPS survey spectra of the initial SiC surface reconstruction and after intercalation of 4 Å Pt + 3 nm Co in the upper and lower panel, respectively. The electron signals of the respective elements, plasmon loss features, and Auger signals are assigned in the figure. After intercalation, a very weak oxygen contamination was detected, as visible in the green area in the lower panel.

Next, a detailed analysis of the C 1s, Si 2p, Pt 4f, and Co 3p signals has been carried out. For this purpose, high-resolution spectra were recorded in each preparation step. The C 1s-, Si 2p-, Pt 4f-, and Co 3p-spectra were taken at 450 eV, 180 eV, 240 eV, and 180 eV, respectively. During the analysis, a combination of a linear and Shirley

background was removed [156]. For some of the Si 2p-spectra, additionally, a slope background was used [211]. The spectra were decomposed into components with Voigt- and Gauss-Doniach lineshapes [148, 212]. The parameters for the background and the components were determined by applying an active fitting-procedure [160]. The parameters for each component of each orbital are listed in Appendix A.

6.3.1 Carbon 1s signal

Figure 6.8 shows C 1s core level spectra of a sample in all preparation states. Spectra of the bare reconstructed SiC are presented in the first row. They consist of four components, assigned to SiC, graphene, S1, and S2. The components S1 and S2 are assigned to carbon atoms with bonds within the uppermost surface plane and bonds towards the Si atoms underneath, respectively. Thus, they represent the $(6\sqrt{3} \times 6\sqrt{3})$ R30°-reconstruction. The presence of a small graphene component results from graphene stripe formation at the step edges, as explained in Section 6.1. The last component, SiC, originates from the substrate. [40, 62]

The deposition of 4 Å Pt did not change the spectrum qualitatively, as can be seen in the spectra in the second row of Figure 6.8. Only the graphene component becomes slightly more pronounced, which can be attributed to the change in depth of the individual components. Furthermore, a small part of the platinum possibly already intercalated even without annealing. This process is usually limited to a small amount of the intercalate.

Spectra after the intercalation of platinum are shown in the third row of Figure 6.8. Due to this preparation step, the spectra change in three aspects. First, the photoemission features of the $(6\sqrt{3} \times 6\sqrt{3})$ R30°-reconstruction, S1 and S2, almost disappeared, while second, the graphene component increased significantly. These findings indicate the decoupling of the carbon layer and its transformation into quasi-freestanding graphene and, thus, a successful intercalation. The third change is the appearance of two additional components, SiC' and SiC''. They are associated with carbon atoms in the upper first SiC layers, which are in a changed Coulomb environment now due to the presence of Pt. Comparing the heights of the components in the spectrum taken at $\Theta = 0^\circ$ with those in the spectrum taken at $\Theta = 60^\circ$ supports the assumption that the new components are located at the top of the

substrate. Similar effects, with only one additional component, were found for the intercalation of H, Li, and Si [47, 72, 213, 214].

The deposition of 3 nm Co only moderately changed the components' height ratios, as seen in the fourth row of Figure 6.8. The signals of the components belonging to layers deeper inside the sample are suppressed slightly, especially at $\Theta = 60^\circ$.

The only effect of the Co intercalation was another slight change in the height ratios of the components and the disappearance of the last bit of components S1 and S2. Corresponding spectra are shown in the fifth row of Figure 6.8.

C 1s ($h\nu = 450 \text{ eV}$)

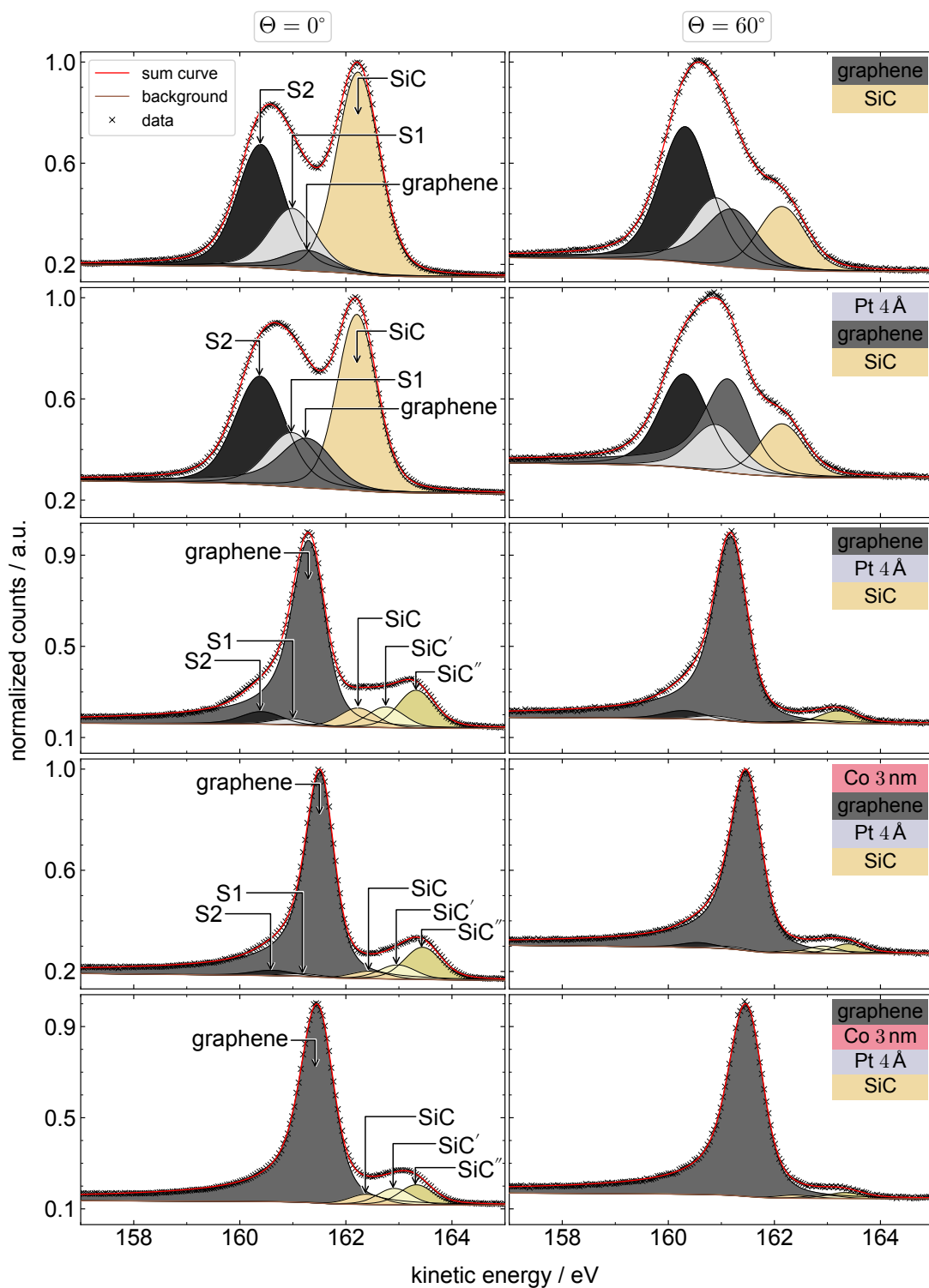


Figure 6.8: High resolution C 1s XPS spectra of the bear buffer layer (1s row), after Pt deposition (2nd row), intercalation (3rd row), Co deposition (4th row), and intercalation (5th row) at normal emission $\Theta = 0^\circ$ (left) and at $\Theta = 60^\circ$ (right).

6.3.2 Silicon 2p signal

Components of the surface reconstruction, the silicon carbide, and its changed upper first layers after platinum intercalation also appear in the Si 2p-spectra, shown in Figure 6.9. Spectra of the bare reconstructed SiC are presented in the first row. Two components can be identified, SiC and S2, representing the substrate and the silicon atoms bonded to the $(6\sqrt{3} \times 6\sqrt{3})$ R30° surface reconstruction, respectively. The component S2 reflects the same atomic bonds in the C 1s spectra and in the Si 2p spectra. Since component S1 in the C 1s spectra represents carbon atoms with bonds only within the surface reconstruction layer, it has no such counterpart in the Si 2p spectra. Because the component S2 indicates the surface reconstruction in the Si 2p spectra, it is also referred to in the literature as $6\sqrt{3}$ [47].

After the deposition of 4 Å Pt, only a small change in height appears. Corresponding spectra are shown in the second row. As for the C 1s signal, this change can be associated with the change in depth of the components and with a small part of platinum that has already intercalated, even without annealing.

After the intercalation of platinum, a total of seven new components appeared. The spectra of this preparation step are shown in the third row of Figure 6.9. As for the C 1s signal, there are two components assigned to the upper first layers of silicon carbide, which are now in a changed Coulomb environment, SiC' and SiC''. They are shifted towards smaller kinetic energies compared to the substrate's component. Next, there are three components, Pt₁Si, Pt₂Si, and Pt₃Si, which originate from different platinum silicide formations. These will be discussed in more detail when analyzing the Pf 4f-spectra. They are located at higher kinetic energies compared to the substrate's component. In between the silicon carbide and the platinum silicide components, a Si-Si component is placed. Comparing the spectra taken at $\Theta = 0^\circ$ and $\Theta = 60^\circ$ shows that this component's height behaves almost the same as the silicide components. Consequently, the silicon atoms forming Si-Si bonds seem to be localized near or in the Pt-layer. This is true for all states of preparation. Lastly, there is a component fitted by a singlet component. It is identified to be a Si 2p satellite [215].

After 3 nm Co has been deposited, a signal from the Co 3s orbital and a Si³⁺ component are added to the spectra. The spectra can be seen in the fourth row of

Figure 6.9. Since the Si^{3+} component is very small, it might also have been present before cobalt deposition but not visible compared to the others.

After cobalt intercalation, this component grows, indicating that a thermally activated process causes the silicon atoms to form this component. Its change in height regarding the angle of emission is similar to that of the Si-Si and the platinum silicide component. Therefore, it can also be attributed to the silicon atoms within the Pt-layer. Furthermore, the cobalt component decreases in intensity because it is covered by graphene after intercalation. The corresponding spectra are shown in the fifth row of Figure 6.9.

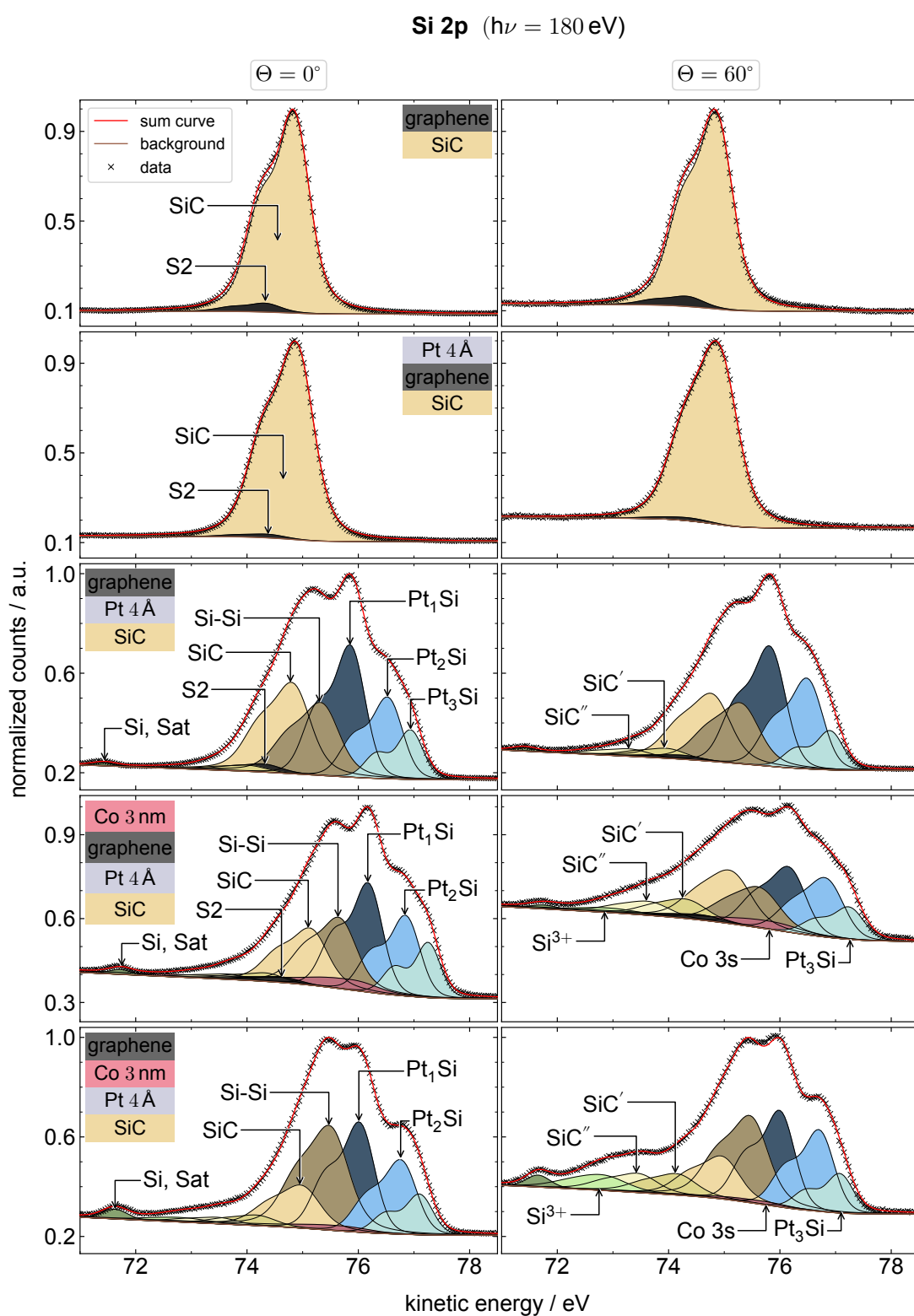


Figure 6.9: High resolution Si 2p XPS spectra of the bear buffer layer (1s row), after Pt deposition (2nd row), intercalation (3rd row), Co deposition (4th row), and intercalation (5th row) at normal emission $\Theta = 0^\circ$ (left) and at $\Theta = 60^\circ$ (right).

6.3.3 Platinum 4f single

Figure 6.10 shows XPS spectra of the Pt 4f doublet. Right after platinum deposition, there are four components. One of them can be assigned to pure platinum, while the others represent different platinum silicide formations, Pt₁Si, Pt₂Si, and Pt₃Si. In accordance with the growing graphene component in the C 1s signal and the decreasing $6\sqrt{3}$ component in the Si 2p spectra, the appearance of platinum silicide even before annealing indicates that part of the platinum did already intercalate even without thermal activation.

After annealing, almost all the platinum is bonded to Si, as shown in the spectra in the second row of Figure 6.10. This can be explained by the platinum now being located in between the graphene and the silicon carbide. Thus, the transformation of practically all the pure platinum into platinum silicide is another result of successful platinum intercalation.

Neither the deposition nor the intercalation of 3 nm Co led to any further qualitative change in the Pt 4f signal. Only the height ratios of the components changed slightly. Thus, cobalt intercalation does not alter the chemical structure of the Pt-layer. Corresponding spectra can be seen in the fourth and fifth row in Figure 6.10. In all preparation states, the components in the spectra taken at $\Theta = 0^\circ$ and $\Theta = 60^\circ$ have approximately the same height ratios, which indicates a well-defined and thin Pt-layer.

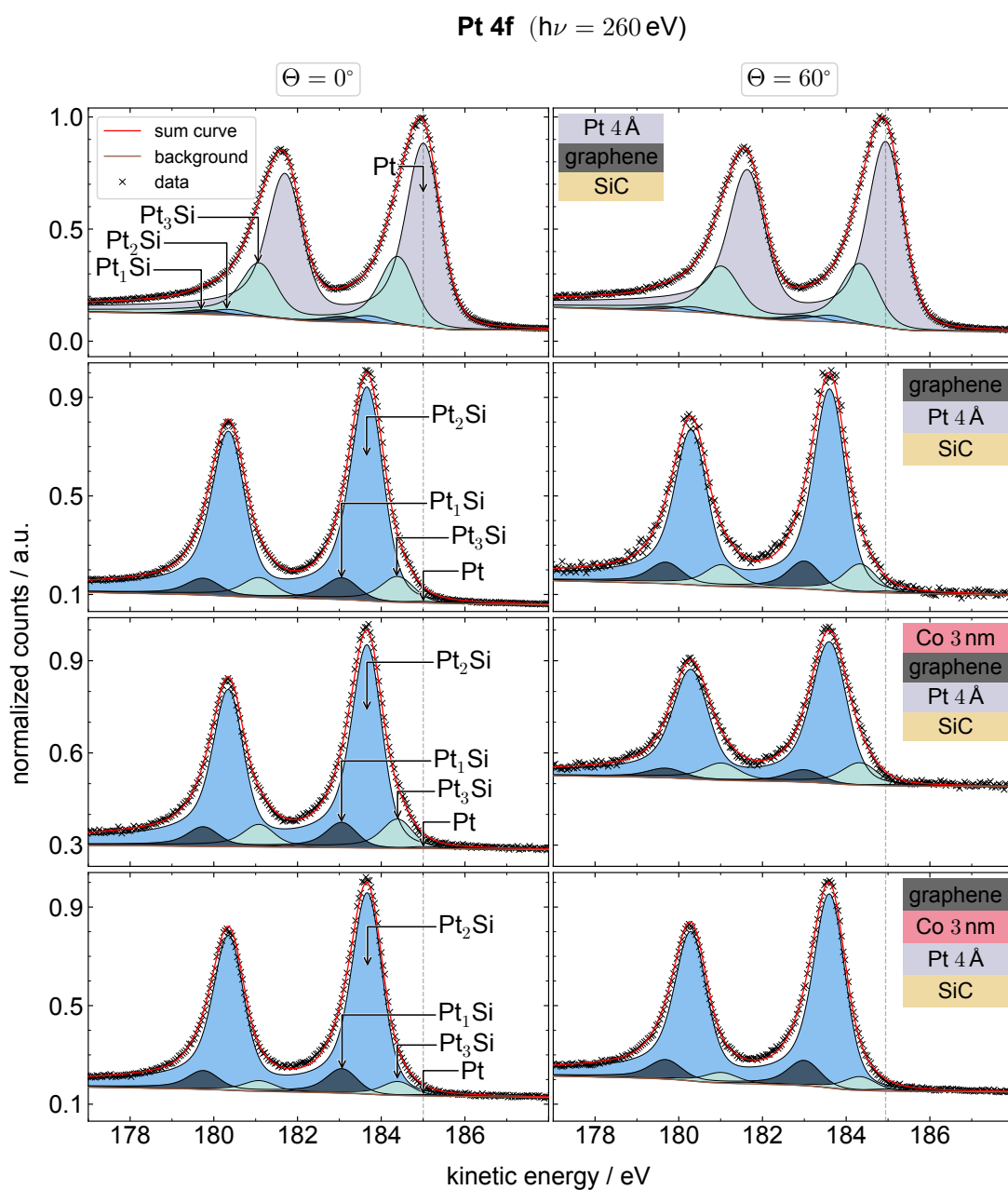


Figure 6.10: High resolution Pt 4f XPS spectra after Pt deposition (1st row), intercalation (2nd row), and subsequent Co deposition (3rd row), and intercalation (4th row) at normal emission $\Theta = 0^\circ$ (left) and at $\Theta = 60^\circ$ (right).

6.3.4 Carbon 3p signal

The Co 3p spectra before and after intercalation can be fitted with the same components and almost identical height ratios, as displayed in Figure 6.11. This proves the successful prevention of cobalt-silicide formation by first intercalating platinum. Next to the core level signal, two Co-satellite peaks are identified. These are associated with shake-up (Sat1) and shake-down (Sat2) signals [216]. Spectra in the first and second rows of Figure 6.11 show the signal before and after intercalation, respectively. After intercalation, the Pt 5p doublet is much more pronounced. Prior to annealing, this signal was extremely small. As a consequence of the intercalation, the cobalt is covered by the graphene layer, resulting in decreased photoelectron intensity. Since the Pt signal is not affected by intercalation, its intensity remains the same. Taken together, the intensity of the Co 3p signal decreases compared to the Pt 5p signal. This makes the later signal more pronounced in the spectra. Moreover, the Pt 5p signal is larger at $\phi = 0^\circ$ than at $\phi = 60^\circ$ when compared to the Co 3p signal. This shows that the Pt-layer is still below the Co-layer after intercalation.

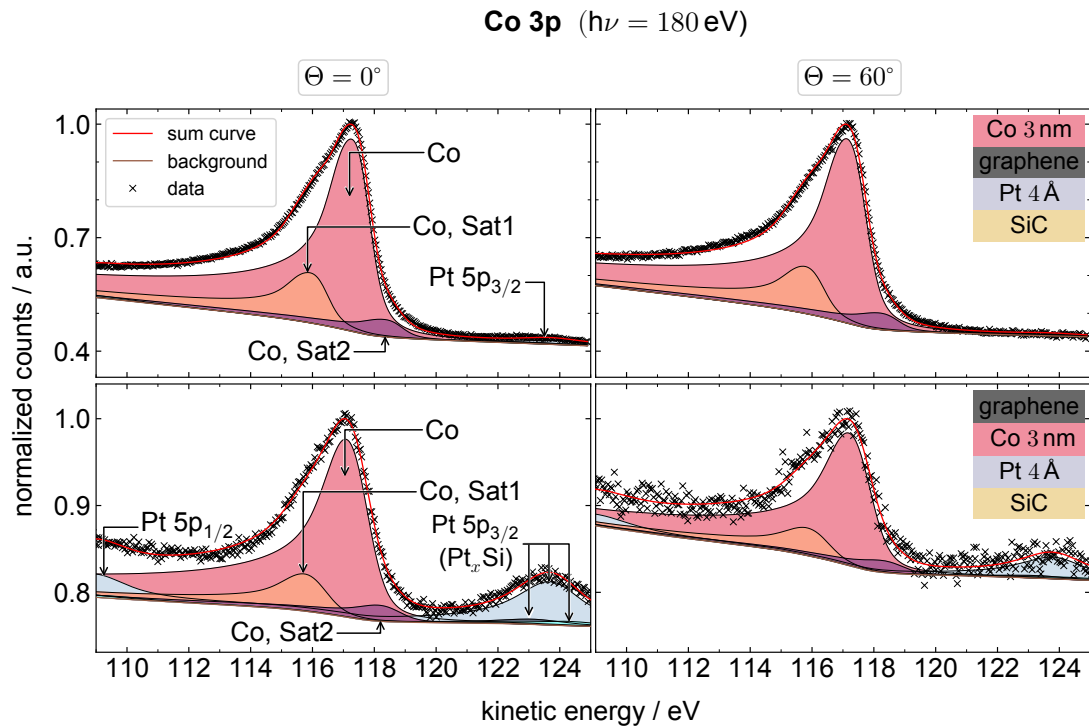


Figure 6.11: High resolution Co 3p XPS spectra after Co deposition (1st row) and intercalation (2nd row) at normal emission $\Theta = 0^\circ$ (left) and at $\Theta = 60^\circ$ (right).

As desired, there is no chemical change in the cobalt signal due to intercalation, such as the formation of silicides. However, this makes it necessary to prove successful intercalation in another way. For this reason, angle resolved XPS (ARXPS) was used. The spectra shown in Figure 6.12 display data of the C 1s and the Co 3p signals. The data represents the intensities after intercalation divided by those before as a function of polar angle. The Co 3p signal ratio decreases, while the C 1s signal ratio increases at high polar angles. This indicates Co intercalated under the top carbon layer due to annealing.

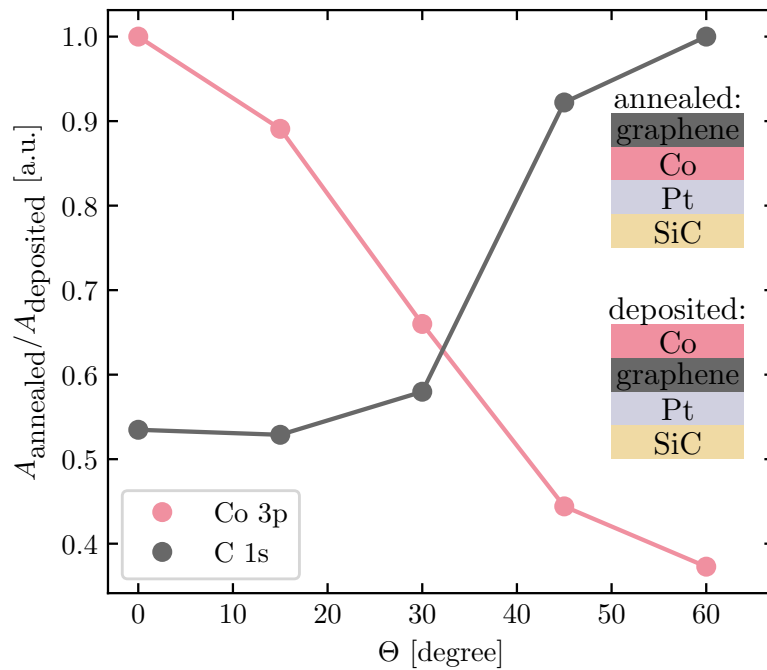


Figure 6.12: Intensity ratios of normalized XPS intensities after to before annealing of the Co 3p and C 1s signals as a function of polar angle. The Co-layer thickness was 1 nm.

6.3.5 Summary

To summarize the results obtained by XPS, the intercalation of platinum could be successfully confirmed by the increasing graphene component in the C 1s signal together with the decreasing components S1 and S2. Furthermore, due to platinum intercalation, two components appeared in the C 1s and the Si 2p spectra. These are associated with the uppermost silicon carbide layers being in a changed Coulomb environment due to the presence of platinum. Moreover, a Si-Si signal appeared in the Si 2p spectra. The corresponding silicon atoms are most likely located in the Pt-layer. Lastly, three platinum silicide components have formed. All three of these were already present in the Pt 4f signal prior to annealing, suggesting that part of the platinum did intercalate even before thermal activation. This assumption is supported by the finding that the reconstruction component decreases and the graphene component increases moderately in the Si 2p and C 1s spectra due to platinum deposition.

As desired, the cobalt signal did not change chemically as a result of annealing. Its intercalation was confirmed by ARXPS. The last result was the appearance of a Si³⁺ component, which seems to be caused by the annealing.

6.4 X-ray photoemission electron microscopy

6.4.1 Data processing

After complete preparation, the magnetization orientation of the sample system's Co-layer was investigated using X-PEEM combined with XMCD. The steps of analyzing these images are illustrated in Figures 6.13 and 6.14 and explained in the following.

Raw X-PEEM images were taken with circularly polarized light with both positive and negative helicity at the Co L_3 -edge and a few eV below, i.e., at 776.6 eV and 770 eV. At each sample position and azimuth angle, a total of 160 individual images were acquired in a series with the following symmetrical sequence:

		1.	2.	3.	4.	5.	6.	7.	8.
Energy	Co L_3 -edge		x	x			x	x	
	Pre edge	x			x	x			x
Helicity	Positive	x	x					x	x
	Negative			x	x	x	x		
Number of Images		20	20	20	20	20	20	20	20

Table 6.1: Sequence of images taken using X-PEEM at each sample position and azimuth angle. The sequence of steps 1.-4. is reversed for 5.-8 to create symmetry.

The symmetry of the series reduces the mean thermal drift between the different types of images. This drift causes the field of view to move slightly over time. Consequently, a long exposure time would impair the image sharpness. However, to improve statistics, a long exposure time is advantageous. To resolve this issue, individual images with a short exposure time of 3 s were taken, corrected for shift, and summed up, as illustrated in Figure 6.13a. This was done for each type of image. To do so, one image serves as a reference in which a characteristic part is selected. The Fourier transformation of this part is compared systematically to those of every other image to find the best alignment. Subsequently, the summed images of different helicities and energies were also aligned, which was done manually.

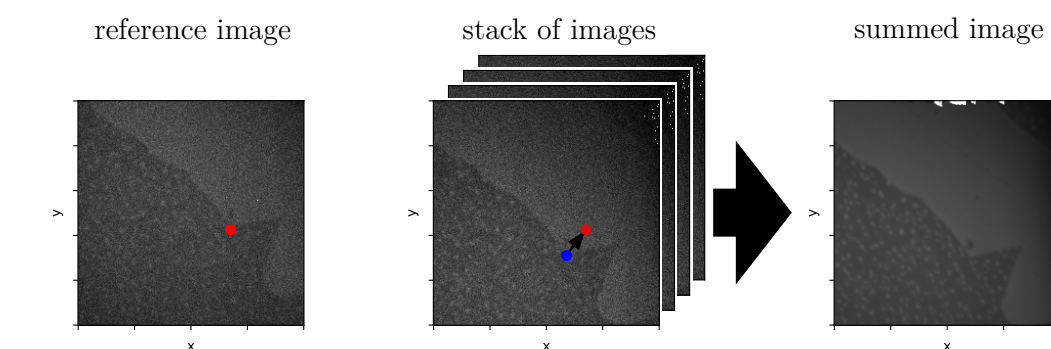
At each sample position, images were taken under azimuth angles $\phi = 0^\circ$, 90° , and 180° to obtain complete insight into the magnetic structure. By rotating the sample,

imaging conditions are slightly changed, causing a small image distortion. Even a small sample tilt or a minute unequal distortion of the electric field between the sample and objective lens influences the resulting images. To correct this distortion, the homography matrix \mathbf{G} is used. It transforms an image I with points $\mathbf{p}_i = (x_i, y_i, 1)$ so that it is mapped to a reference image I' with points $\mathbf{p}'_i = (x'_i, y'_i, 1)$:

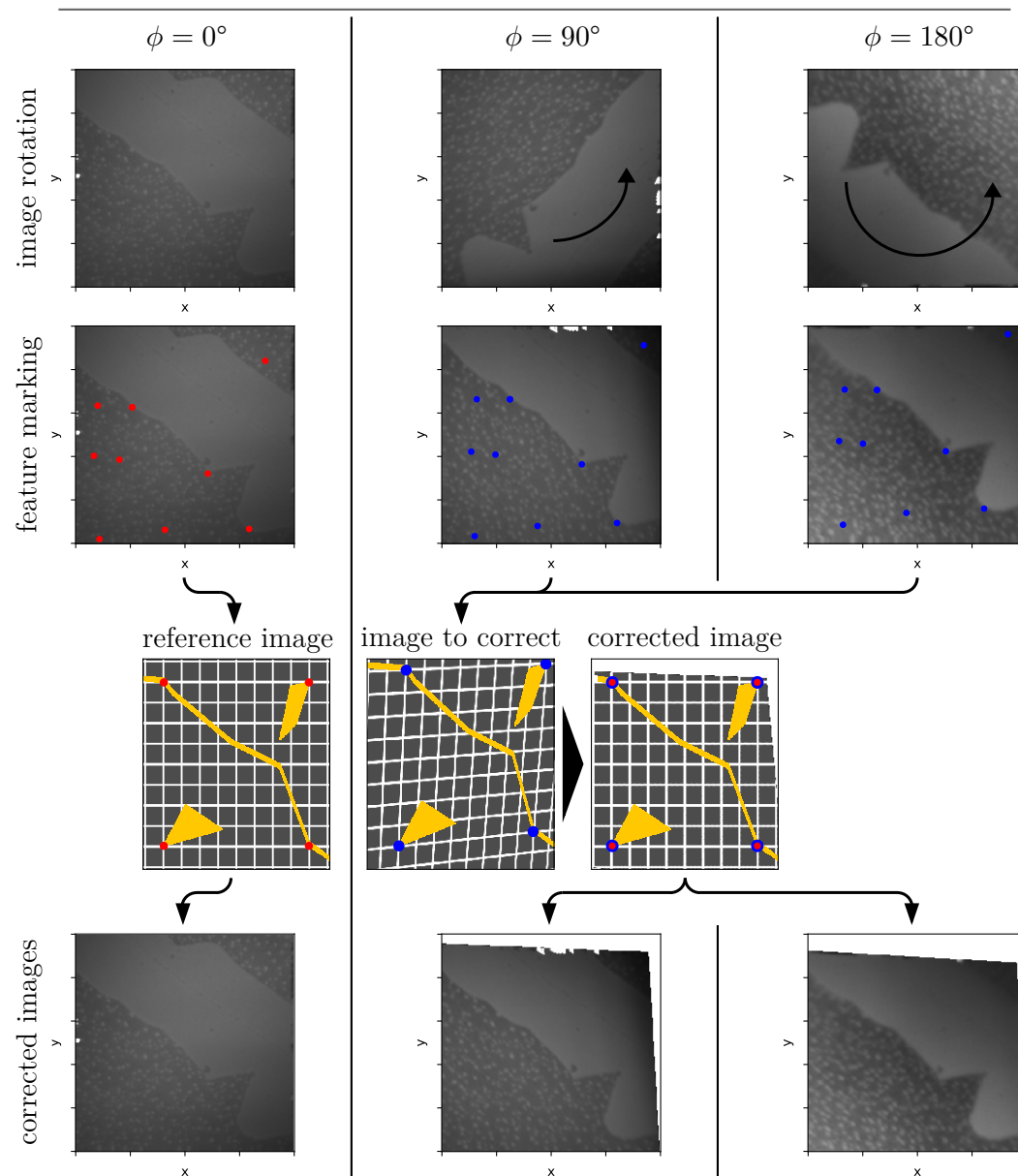
$$\alpha_g \mathbf{p}_i = \mathbf{G} \mathbf{p}'_i, \quad (6.1)$$

with α_g being a scaling factor [217]. For the X-PEEM data, it is $\alpha_g \approx 1$. Since, in practice, the distortion and determination of the points are not perfect, \mathbf{G} has to be determined by a fit. For this, the error of the back-projection is minimized by using a least square fit. To obtain a reliable result, approximately 20 characteristic points distributed over the entire field of view of two corresponding images were used per fit in this work. For each sample position, one image was used as a reference, and the other two were corrected. The distortion correction is illustrated in Figure 6.13b. Rotating the sample leads to a change in the magnetic contrast images, while the ones with topographic contrast remain unchanged. Therefore, it is much easier to determine the homography matrices for the topographic contrast images. For this reason, the homography matrices were calculated using the images with topographic contrast and then used to correct the corresponding images with magnetic contrast. Afterwards, the magnetic structure was analyzed.

The determination of the magnetic structure is illustrated in Figure 6.14. First, the XMCD images were calculated for each azimuth angle. This was done by combining the sum images taken at the Co L₃-edge with different helicities according to Equation 3.12. In the images, the intensity I_{XMCD} is given per pixel. Subsequently, a plane background was removed for each image. It is strongly pronounced in the XMCD image taken at $\phi = 90^\circ$. Before the plane background was removed, the upper right part of the image showed a much darker blue color than the rest. For illustration, the effect has been enhanced to make it more visible. Since there is no reason for such inhomogeneity associated with the sample, this background is associated with imperfect sample irradiation. It is particularly important that the mean value of an image is not changed in this step. This would change the calculated strength of the magnetic structure's components. Lastly, the individual components of the magnetization are calculated as described by Equation 3.16 and in Appendix B.



(a) Drift correction for images of one type and resulting summed image.



(b) Image correction between summed images taken at different azimuth angles.

Figure 6.13: Illustration of the correction process for X-PEEM images.

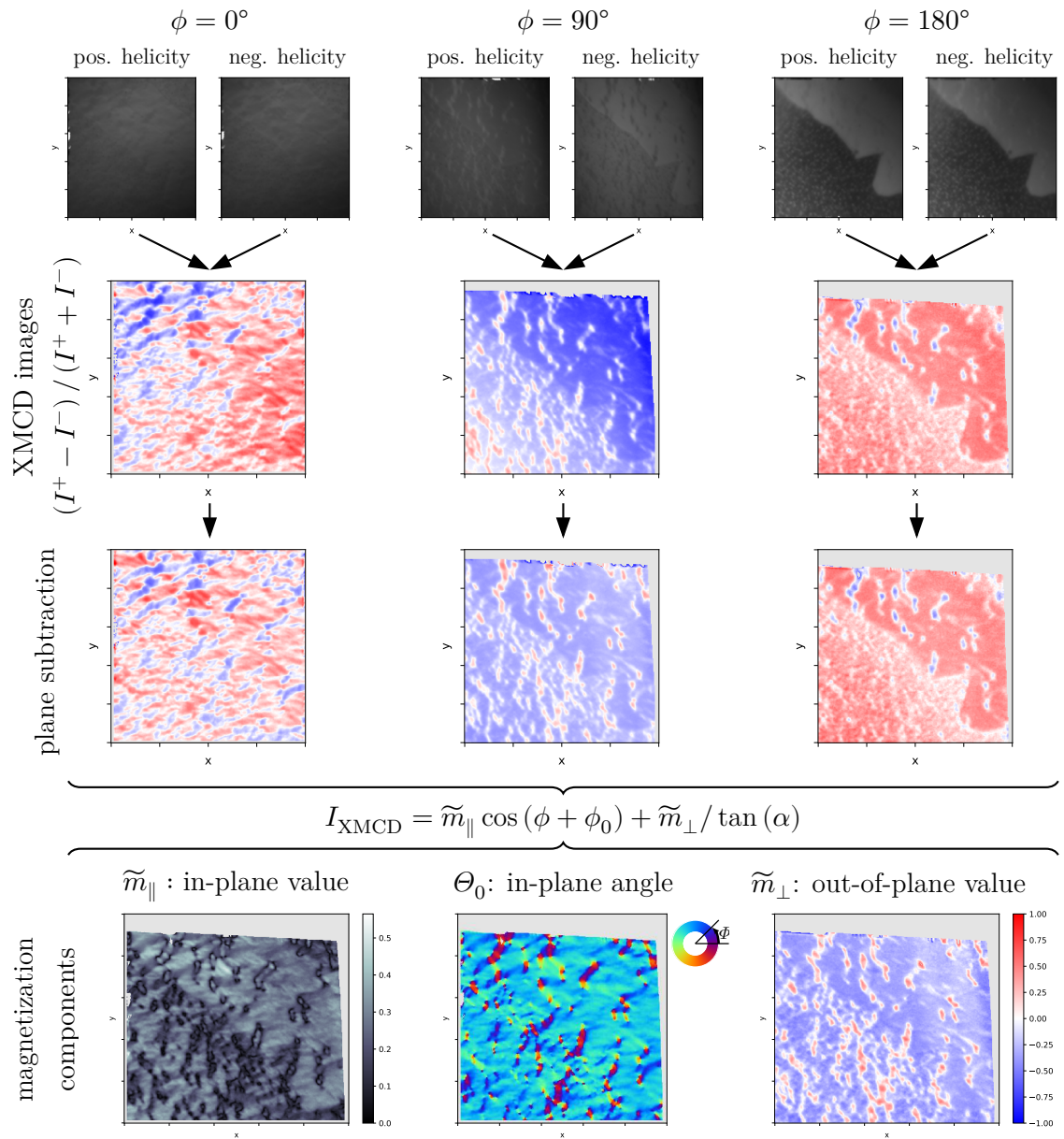


Figure 6.14: Illustration of the determination of the magnetization components using X-PEEM images. First, the XMCD images are calculated for each azimuth angle. Subsequently, a plane background is subtracted. Finally, the sample's magnetization components are calculated.

6.4.2 Magnetic structure of the embedded Co-layers

To investigate the influence of the preparation on the magnetic properties of the intercalated Co-layer, three different sample sets were prepared:

- A** CCS method and *ex-situ* treated,
- B** PASG method and *ex-situ* treated,
- C** CCS method and *in-situ* treated.

Ex-situ/in-situ sample treatment means that the samples were/were not exposed to air between preparation and investigation. All previous investigations were done solely *in-situ*. LEED patterns and XPS spectra of samples prepared with the two preparation methods, CCS and PASG, were quasi-identical. No difference could be identified. Figure 6.15 displays X-PEEM images of each sample type. The first column depicts chemical contrast images obtained by spatially resolved x-ray absorption spectroscopy displaying the morphology of the cobalt films. These images were acquired by subtracting images recorded at an energy a few electronvolt below the Co L₃-edge $I_{\text{pre edge}}$ from those taken at the edge I_{edge} :

$$I_{\text{XAS}} = \frac{I_{\text{edge}} - I_{\text{pre edge}}}{I_{\text{pre edge}}}. \quad (6.2)$$

Dividing by $I_{\text{pre edge}}$ removed the effects of an unequal sample irradiation. Both intensities represent sums of corresponding intensities recorded with positive and negative helicity.

In the second column, images of the in-plane magnetization angle are presented. In addition to the domain structure, the in-plane angle also shows features like vortices. For this reason, it is used for structural analysis in the following. All the images shown in Figure 6.15 and those presented in the following for samples **A**, **B**, and **C** are also shown in a sample-wise overview in Appendix C.

Chemical contrast images

The chemical contrast images, shown in Figures 6.15 (A1) and 6.15 (B1), are characterized by dark lines, depicting a decreased amount of cobalt compared to the

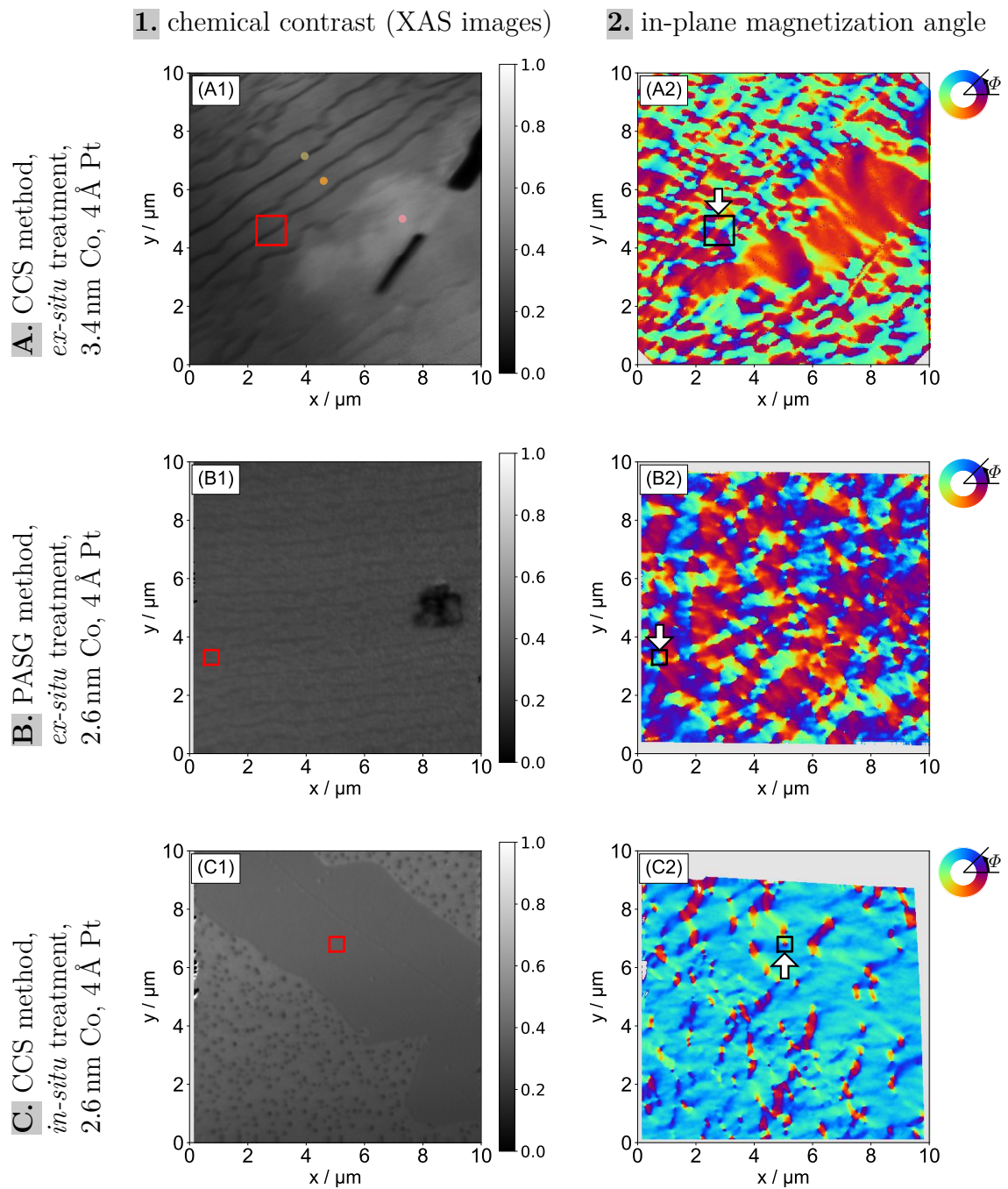


Figure 6.15: First column: X-PEEM images with chemical contrast (XAS images) recorded at the Co L_3 -edge. Step edges are visible as dark stripes, indicating that the Co-atoms avoid these areas. In image (A1), three different areas are visible, marked with dots. These are one step edge with a green dot, one terrace with an orange dot, and the continuous area with a red dot. XAS spectra of these areas are shown in Figure 6.17. Second column: In-plane magnetization angle of the Co-layer embedded between graphene and a 4 Å Pt-layer on SiC. Rectangles and arrows mark regions of which the in-plane magnetization direction is shown in close-ups in Figures 6.18-6.21.

rest of the images. These lines indicate the substrate's step edges. As explained in the previous sections, cobalt avoids the edges due to graphene stripe-formation over the buffer layer at step edges during preparation. The same was found for Co intercalated graphene on SiC without Pt [38]. However, for sample **A**, Pt intercalation prior to Co intercalation resulted in some small regions where no step edges were visible at all. In Figure 6.15 (A1), such a continuously covered region can be observed around the defect in the lower right. Its brighter contrast compared to the rest of the image indicates a locally thicker Co-layer. Continuously covered regions were only found for sample **A**. The increased Co-layer's thickness of 3.4 nm for the presented sample **A** compared to 2.6 nm for the other samples shown led to an overall more continuous Co-layer for this sample type. However, locally increased Co-layer thicknesses were also observed for thinner cobalt layers. Figure 6.16 presents the XAS image of a sample intercalated with 2.6 nm Co and 4 Å Pt. One wide stripe, most probably representing three or four terraces, shows such an area with locally increased Co-layer thickness. The other terraces are indicated by a grainy structure, suggesting an incomplete Co-layer on these. Interestingly, bright lines are present instead of dark ones associated with the step edges. This might be due to the cobalt accumulating near the step edges before it is fully covered. In this case, they would grow until a terrace is completely covered, excluding only the area under the step edges. Although only sample type **A** shows continuously covered regions, the flatter steps of the PASG-samples lead to a weaker contrast between the step edges and the terraces when compared to the CCS-samples. Moreover, many segments of the step edges appear to be continuously covered.

Defects were observed throughout the sample surfaces, and inspection of several images has shown that samples **A** and **B** exhibited approximately one defect per 220 nm². Since all defects appear dark, they are not caused by Co. Instead, they most likely originate from Pt remaining on the surface, even after most of the Pt had intercalated. This is consistent with the CLSM image shown in Figure 6.5. A similar observation was reported for Au [218].

Sample **C** was prepared by using CCS, followed by intercalation and *in-situ* investigation. *In-situ* investigation was chosen to avoid any sample modification due to air exposure or subsequent annealing after reinsertion into the vacuum. These potential modifications include the diffusion of Co into the substrate, Si diffusion

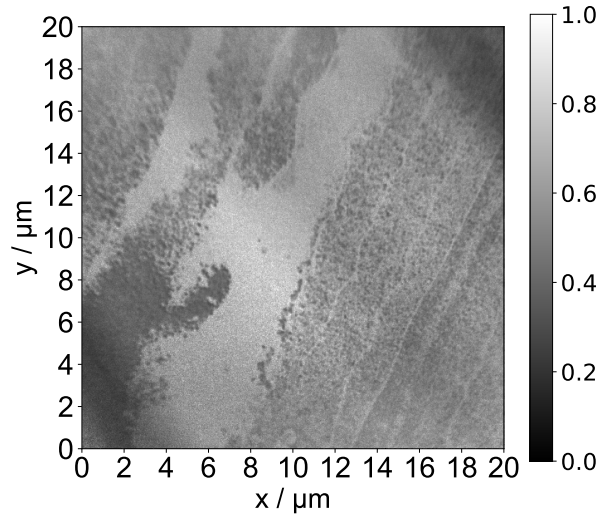


Figure 6.16: XAS image of a sample of type **A** after intercalation of 2.6 nm Co and 4 Å Pt.

into to the Co-layer, and the possibility of a structural rearrangement [209]. The corresponding XAS image is presented in Figure 6.15 (C1). It differs clearly from Figures 6.15 (A1) and 6.15 (B1) in that it exhibits two types of alternating terraces. One type is depicted in homogeneous gray, while the other is displayed in lighter gray with numerous dark dots indicating defects. The dot defects are most probably dewetted Pt remaining on the surface. This common phenomenon is caused by minimizing the surface free energy upon thin film annealing [219]. After further annealing, such dot defects can merge into larger ones, as visible in Figures 6.15 (A1) and 6.15 (B1). The terraces with dot defects are lighter than those without. This can be attributed to Co accumulation on them.

Information about the local chemical properties of the different identified regions has been gained by XAS intensity spectra. Figure 6.17 shows the spectra of the continuous region, the terraces, and the step edges of sample **A**, marked in Figure 6.15 (A1). Only the signal-to-noise ratio and the background shape differ between the spectra, indicating no chemical differences between the Co within the different areas. Furthermore, no oxide components are visible. The branching ratio of all areas is in the interval of [0.63; 0.67]. These results are comparable for the other samples.

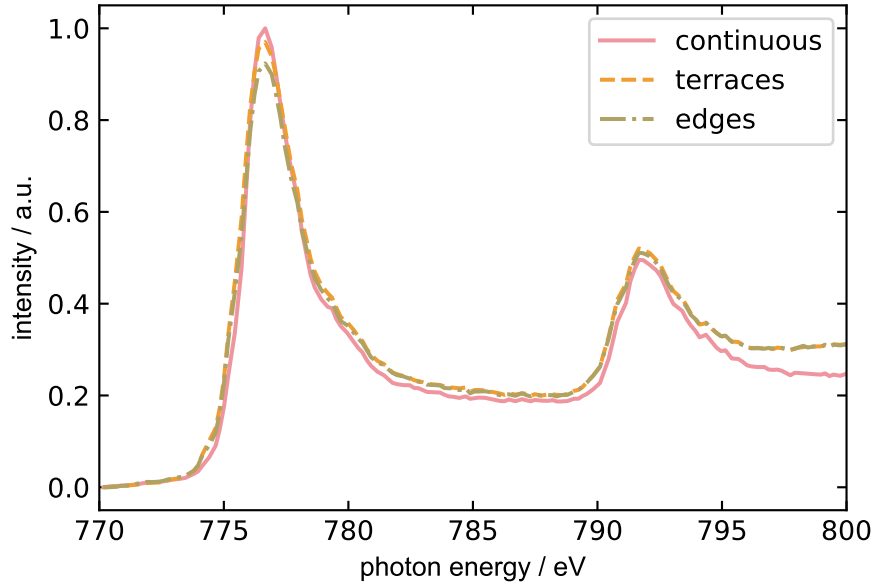


Figure 6.17: XAS intensities of the three different areas of sample **A**, measured around the Co L_3 -edge. The areas are marked in Figure 6.15 (A1).

In-plane magnetization angles

The in-plane magnetization angles of all samples show a texture-rich structure with different spin vortex formations, indicating a strong DMI. These structures are discussed in the following, together with some close-ups of the magnetic formations.

Sample A: The continuously covered region in Figure 6.15 (A1) also differs from the rest by its magnetic structure. The magnetization direction in this region is much more uniform than it is in the stepped ones, as displayed in Figure 6.15 (A2). This is probably caused by reduced DMI due to the increased thickness of the Co-layer [220]. In contrast, the other sample areas are much more diverse and show many structural features. More than 40 strongly pronounced and many more weaker vortices can be found, indicating a much stronger DMI than in the continuously covered area [221]. As an example, one vortex is shown in the close-up in Figure 6.18. To further analyze these vortices, the in-plane and out-of-plane component in this region are considered. Due to experimental uncertainties, it is particularly difficult to accurately estimate the ratio of the in-plane component to the out-of-plane component. However, using an approximation for a small out-of-plane component has almost the

same result as the full analysis. This indicates that the sample is primarily in-plane magnetized. Additionally, this was confirmed by magneto-optical Kerr effect (MOKE) measurements. This effect describes how linear polarized light becomes elliptically polarized when reflected off a magnetic surface [80]. The direction of polarization of the light concerning the light's propagation direction and the sample surface allows the distinction between in-plane and out-of-plane magnetization. All samples investigated showed a hysteresis curve using light with longitudinal and transversal polarization direction, indicating in-plane magnetization. As an example, Figure 6.19 shows the magnetic hysteresis curve of sample **A** taken with light polarization in transversal direction. Using light polarized in polar direction, no hysteresis curve was detected, meaning no significant out-of-plane magnetization was present. Consequently, the vortices are merons. In fact, all samples are primarily in-plane magnetized, which is in contrast to the results of studies of similar systems [16, 37]. Since the PtSi bonds are the main difference from other systems, they are most likely the reason for the absence of significant PMA in the studied system.

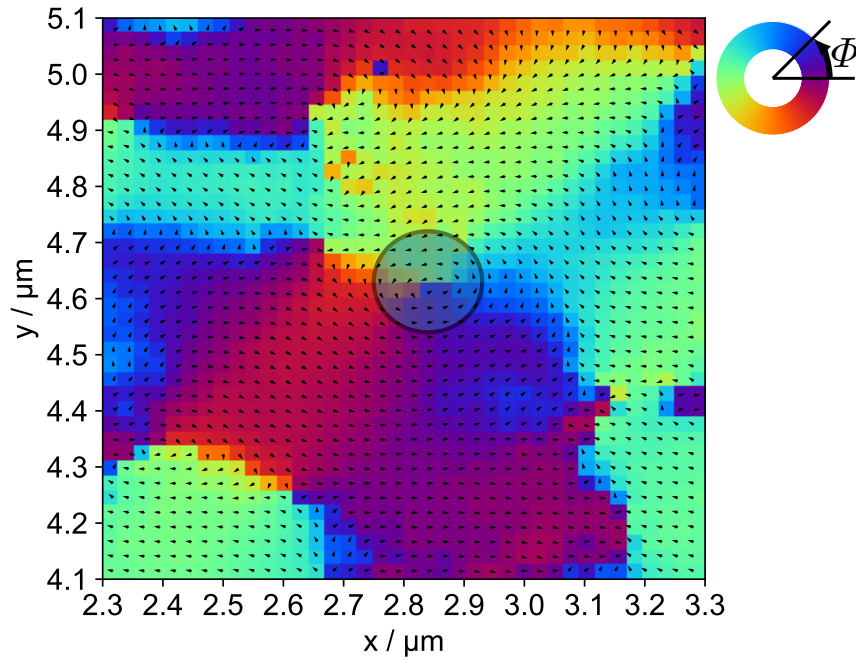


Figure 6.18: Close-up of the in-plane magnetization angle of sample **A** marked in Figure 6.15 by a black rectangle. It shows a meron, highlighted by a dark circle. Arrows indicate the spin direction. Values of x and y are equal to those in the full images.

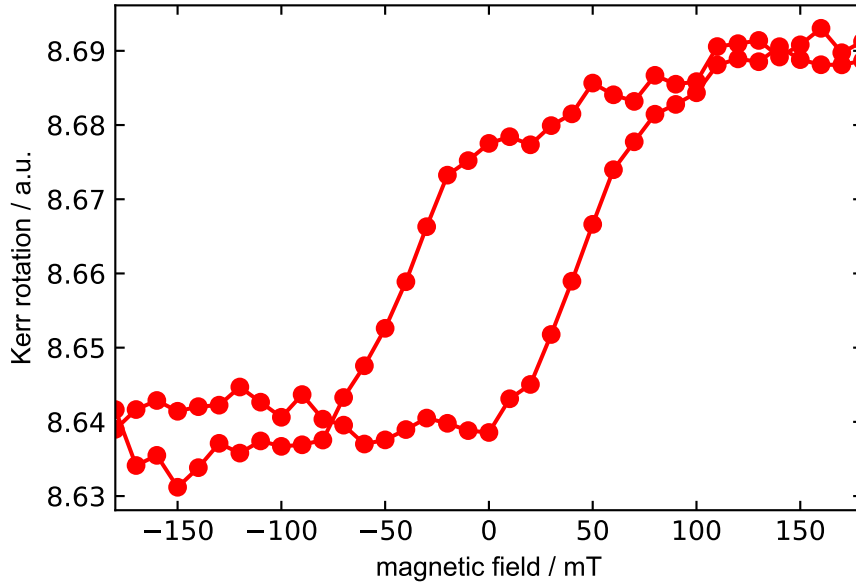


Figure 6.19: Magnetic hysteresis curve from MOKE measurements of sample **A** taken with light polarization in transversal direction.

Sample B: Even though the Co-layer in Figure 6.15 (B1) appears to be more continuous than in the striped areas in Figure 6.15 (A1), the magnetic orientation shown in Figure 6.15 (B2) seems similar to the stepped regions in Figure 6.15 (A2). This sample also shows numerous vortex formations over the entire surface. A total of over 50 relatively large vortices can be identified. In addition, one bimeron was found, which can be seen in the close-up in Figure 6.20. The centers of the anti-vortex (bottom) and the vortex (top) are marked. Remarkably, the anti-vortex and the vortex are surrounded by domains with different spin orientations, which seems to be the reason for the formation of this particular bimeron.

Sample C: The magnetic in-plane angle of the third sample is presented in Figure 6.15 (C2). It is particularly striking that the two types of terraces visible in Figure 6.15 (C1) do not differ in their magnetic structure. As an aside, this reinforces the assumption that the dots in Figure 6.15 (C1) represent Pt, which remains on the sample surface even after the interaction. Furthermore, the edges between the two types of terraces also do not change the magnetization angle.

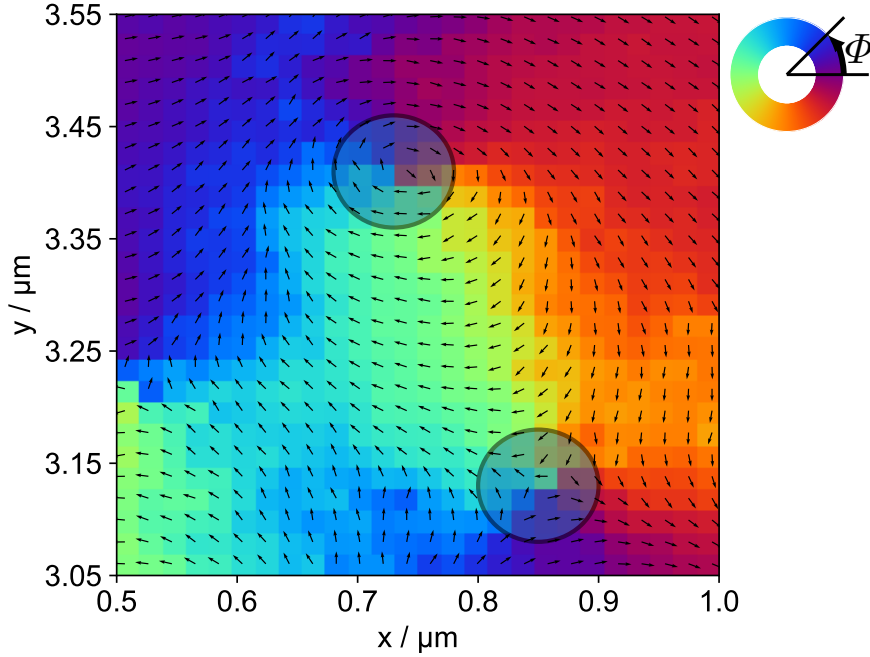


Figure 6.20: Close-up of the in-plane magnetization angle of sample **B** marked in Figure 6.15 by a black rectangle. It shows a particularly large bimeron. Its anti-vortex (bottom) and the vortex (top) are highlighted by a dark circle. Arrows indicate the spin direction. Values of x and y are equal to those in the full images.

The magnetic structure is primarily homogeneous, with many smaller domains of different spin orientations. This indicates that the intercalated Co appears to have formed a relatively homogeneous layer. The disorder in the other samples may be associated with the additional annealing after reinsertion into the vacuum. At the boundaries of the domains to the dominant spin direction, once again, a large number of spin vortices are present. In addition to many weak vortex features, nearly 50 merons and over 20 bimerons are clearly visible. The potential influence of the numerous dot defects on the formation of the merons and bimerons was analyzed by comparing their location in the chemical and magnetic contrast images. No correlation was found, indicating no pinning with a contribution of the defects. Thus, the formations are solely stable due to topological protection [222]. One bimeron is shown in the close-up in Figure 6.21. The center of the anti-vortex (left) and the vortex (right) are marked. Compared to the bimeron of sample **B**, the ones found for sample **C** are much more compact. Even more interestingly, some of them appear to

be isolated. They are not connected to the boundary of two in-plane domains but are located in a region where, otherwise, only the dominant spin direction is present.

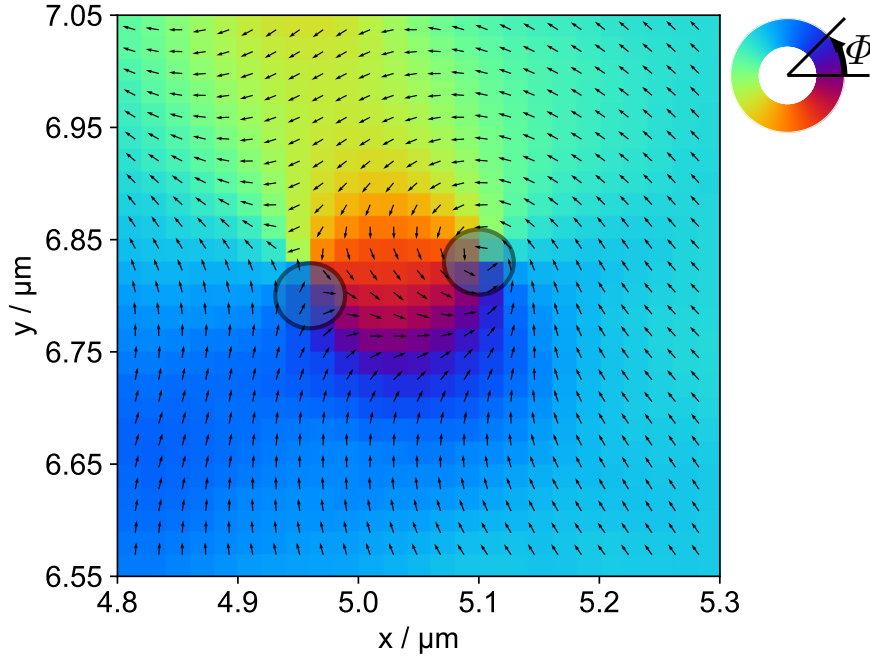


Figure 6.21: Close-up of the in-plane magnetization angle of sample **C** marked in Figure 6.15 by a black rectangle. It shows a bimeron. Its anti-vortex (left) and the vortex (right) are highlighted by a dark circle. Arrows indicate the spin direction. Values of x and y are equal to those in the full images.

6.4.3 Out-of-plane magnetization

Even though the magnetic out-of-plane component is relatively weak, its structure is analyzed to gain further insights into the samples' magnetic properties. For sample **A**, the domains of the in-plane and the out-of-plane component are aligned very well. Its out-of-plane component is shown in Figure 6.22. Regions with an in-plane component pointing to the left (turquoise color) have a positive out-of-plane component, while those pointing to the right (red-purple color) have a negative one. Considering both components, it can be seen that there are mainly two types of domains in the magnetic structure of sample **A**, which point in opposite directions. Consequently, the merons are located in areas with a changing out-of-plane component, even though

this component is small. The region of the close-up shown in Figure 6.18 is also marked by a black rectangle, and the corresponding close-up of the out-of-plane component is shown in the upper right.

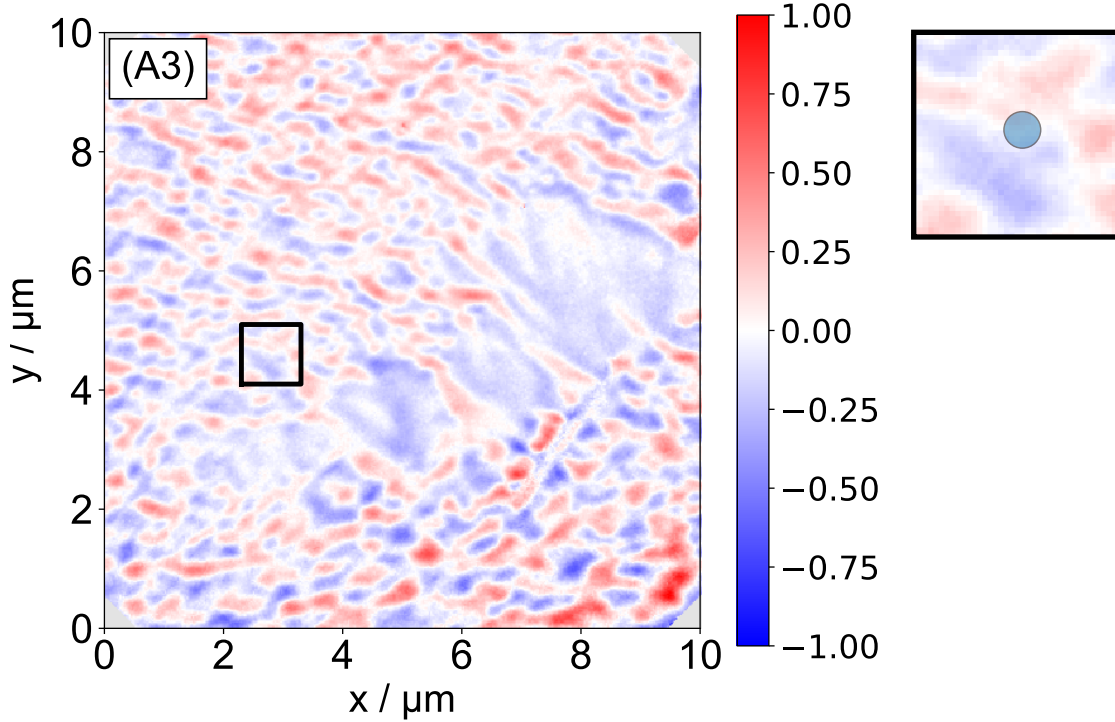


Figure 6.22: Magnetic out-of-plane component of sample **A**, presented in the first row of Figures 6.15. The black rectangle indicates the area whose magnetic in-plane component is shown in a close-up in Figure 6.18. The corresponding close-up of the out-of-plane component is shown in the upper right. The position of the meron is highlighted by a blue circle.

In contrast to sample **A**, the out-of-plane component of sample **B**, shown in Figure 6.23, does not align with its in-plane component. Only very few domain walls follow the same path in both the in-plane and out-of-plane component. As a consequence, for this sample, the merons and bimerons are not positioned closely to the domain walls of the out-of-plane domains.

As for sample **A**, the in-plane and out-of-plane component of sample **C** are aligned almost perfectly. The corresponding out-of-plane component is shown in Figure 6.24. The alignment also results in mainly two types of domains pointing in opposite directions in both the in-plane and out-of-plane component. Regions with an in-plane

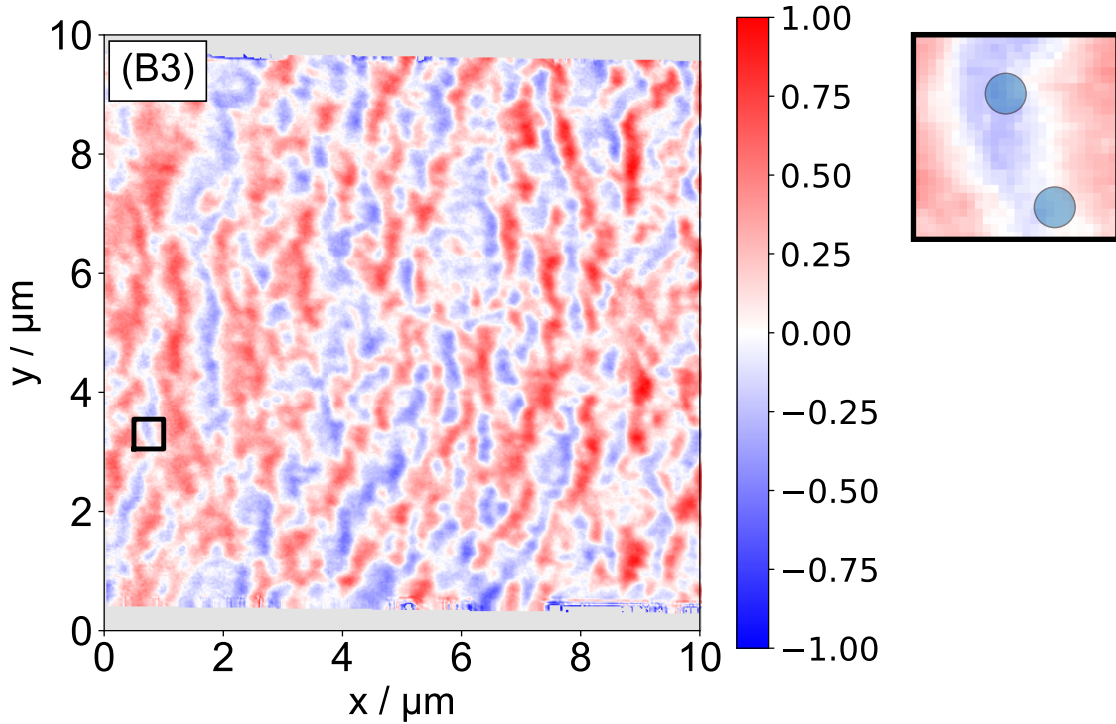


Figure 6.23: Magnetic out-of-plane component of sample **B**, presented in the second row of Figures 6.15. The black rectangle indicates the area whose magnetic in-plane component is shown in a close-up in Figure 6.20. The corresponding close-up of the out-of-plane component is shown in the upper right. The positions of the bimeron's anti-vortex (bottom) and the vortex (top) are highlighted by a blue circle.

component pointing to the top-left (blue color) have a negative out-of-plane component, while those pointing to the bottom-right (red color) have a positive one. As a consequence, the merons are located at domain walls of the out-of-plane component. Moreover, most bimerons are positioned in such a way that their vortex and anti-vortex are located on two sides of an out-of-plane domain. The close-up region shown in Figure 6.18 is also marked by a black rectangle, and the corresponding close-up of the out-of-plane component is shown in the upper right.

At last, the orientation of the magnetic domains was compared to the direction of the step edges. For sample **A** and **C**, no correlation was found at all between the magnetic domains and step edges. For sample **B**, the direction of many magnetic in-plane domains is almost parallel to the step edges and a few domain walls are at the position of step edges. However, the alignment of the domains of sample **B** does not appear to be correlated with the direction of the step edges, as the vast majority

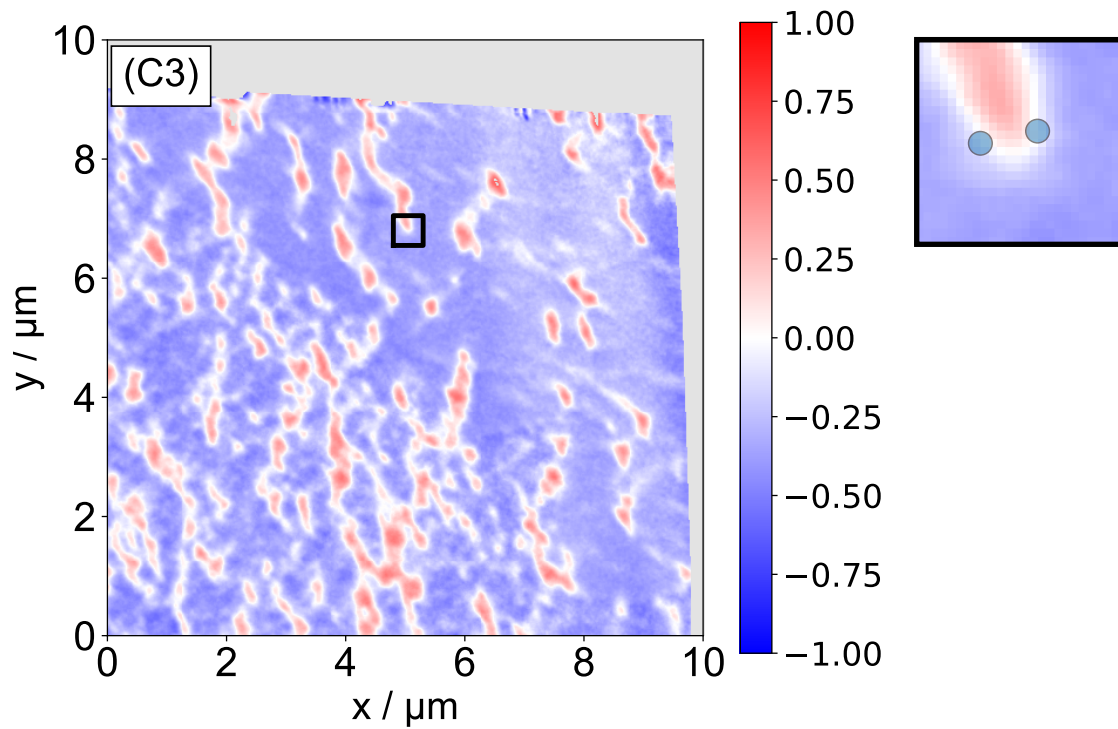


Figure 6.24: Magnetic out-of-plane component of sample **C**, presented in the third row of Figures 6.15. The black rectangle indicates the area whose magnetic in-plane component is shown in a close-up in Figure 6.21. The corresponding close-up of the out-of-plane component is shown in the upper right. The positions of the bimeron's anti-vortex (left) and the vortex (right) are highlighted by a blue circle.

of the domains reach over them instead of being confined or otherwise influenced by them. In conclusion, the orientation of the step edges is not correlate with the orientation or shape of the magnetic domains.

6.4.4 Summary

To end this section, a concluding summary of the results obtained using X-PEEM is provided below. The three investigated samples, sample **A** (CCS, *ex-situ*), sample **B** (PASG, *ex-situ*), and sample **C** (CCS, *in-situ*), differ in both the chemical structure and in the magnetic structure of their Co-layer.

The chemical contrast images revealed two distinct features: step edges, which were visible due to a reduced amount of cobalt caused by graphene stripe-formation, and numerous defects associated with remaining Pt.

Sample **A**: It appears that sample **A** has the most pronounced step edges. Uniquely for this sample type, it has been observed that μm -sized continuously covered regions appeared, associated with a local Co accumulation. It is possible that these regions could form as a result of the significant height of the steps in this sample type. This makes even distribution of the Co across steps more difficult.

Sample **B**: The flatter steps of sample **B** led to a weaker contrast between the step edges and the terraces. Moreover, only for this sample many segments of the step edges are covered by the Co.

Sample **C**: The defects of sample **C** are smaller in size and higher in number than those of samples **A** and **B**. This indicates the defects to be Pt remaining on the surface, even after most of the Pt had intercalated. The additional annealing of samples **A** and **B** after they have been reinserted into the vacuum caused their individual Pt-defects to merge into fewer and larger ones.

As proven by XAS intensity spectra, the chemical properties of the Co-layer are not affected differently by the terraces, step edges, or defects. Its magnetic structure also does not correlate with the step edges or defects. Neither are the magnetic domains restricted by the step edges, nor is their value or orientation influenced by crossing them. This is true for the in-plane and out-of-plane components. This observation differs from the findings for the system graphene/Co/SiC(0001) without Pt as a diffusion barrier. In this system magnetic alignment along the step-edges was reported [38]. Moreover, the position of the dot defects is not connected with those of the merons or bimerons identified in the structure. Therefore, it can be concluded that the defects do not cause any pinning, and the stability of the magnetic formations is solely due to topological protection.

The samples appear to be primarily in-plane magnetized, which means that there is no significant PMA. The presence of PtSi bonds in the studied system may be the reason for this, as they represent the main distinguishing factor from similar systems with PMA.

The domains of the in-plane and the out-of-plane components of samples **A** and **C** are aligned very well. Both sample types display mainly two types of domains in the magnetic structure, pointing in opposite directions. In contrast, for sample **B**, the components are not aligned in any noticeable way. The cause of this is yet to be determined. It seems that the samples with higher steps result in the two magnetic components being connected. One possible explanation for this discrepancy may be related to differences in the relative strength of the two components for the different types of samples. Further investigation is needed to say for sure, such as an examination of further Co-layer thicknesses. Moreover, many differences in the in-plane magnetic structure of the different sample types were found. The continuously covered region of sample **A** showed a magnetic structure without any merons. It was much more uniform, similar to a bulk structure, in comparison to in the stepped regions. This is explained by a reduced DMI due to the increased thickness of the Co-layer in this region. The in-plane magnetization structure of the stepped region shows many small domains of different directions and numerous merons. This is the same for the magnetic structure of sample **B**. One of the main differences observed between samples prepared using CCS and those prepared using PASG is that the latter exhibits a more even distribution of Co, which results in the absence of regions without merons.

In contrast to the *ex-situ* samples, which show many small domains, sample **C** shows a predominantly homogeneous magnetic structure with numerous smaller domains of different spin orientations. The transition from a single primary spin direction to many small domains may have been caused by the additional annealing process after reinsertion into the vacuum. It is worth noting that the required annealing temperature was relatively high, i.e. the same that was needed to induce cobalt interaction, and the annealing time was quite long at half an hour. These conditions may have caused the alteration in the magnetic structure. At the boundaries of the domains of sample **C** to the dominant spin direction, again numerous merons and bimerons are present. The bimerons are very compact in size. Some of them appear

to be isolated, meaning they are not connected to the domain wall separating two larger in-plane domains. Since no such bimerons were found in the *ex-situ* samples, it is possible that the additional annealing step may also cause this to change.

Chapter Conclusion

7

This work presented the successful preparation and comprehensive investigation of a G/Co/Pt multilayer system on SiC. The sample preparation was realized in two steps. First, the $(6\sqrt{3} \times 6\sqrt{3})$ R30°-reconstruction of the SiC(0001) surface was prepared using either the CCS or the PASG method. Subsequently, Pt- and Co-layers were prepared beneath the reconstruction by intercalation. The sample system's structural, chemical, and magnetic properties were investigated using LEED, XPS, and PEEM. Different preparation variations were used to investigate possible changes in the resulting samples. While the results obtained by LEED and XPS were unaffected regardless of the sample type, the magnetic structure was proven to differ depending on the preparation.

Initial systematic UV-PEEM investigations were used to determine the annealing temperatures required to induce the intercalation of platinum and cobalt. The corresponding images of the bare buffer layer show bright stripes restricted by dark lines. These lines reflect the step edges originating from the substrate's unavoidable miscut angle. The additional monolayer graphene forming at these is the origin of the step edges contrast. After metal deposition, the structure is no longer visible. Even for the thinnest Pt layer thickness investigated, which was only 2 Å thick, no steps were observed at all. This indicates a highly homogeneous coverage. After platinum coverage and subsequent annealing at 550 °C, the step structure reappeared in a weak manner. This represented wetting of the platinum on the surface. The full structure reappeared after intercalation, which occurred at an annealing temperature of $T_{\text{Pt}} = 725$ °C [72]. The intercalation of cobalt was found to be induced for an annealing temperature of $T_{\text{Co}} = 325$ °C [38].

Subsequently, LEED and XPS were used to analyze the structural and chemical properties of the system in every state of the preparation. The platinum intercalation

lifts the $(6\sqrt{3} \times 6\sqrt{3})$ $R30^\circ$ -reconstruction by which it becomes quasi-freestanding graphene. In the LEED images, the transformation can be seen in the fact that the spots of the reconstruction remain absent after intercalation, while those of the substrate and graphene reappeared. Additionally, new spots emerged, showing the platinum arranging in a $(4\sqrt{3} \times 4\sqrt{3})$ $R30^\circ$ -reconstruction. Moreover, the Pt-layers are growing in μm -sized hexagonal structures, as visible in CLSM images. In the XPS spectra, the transformation of the buffer layer into quasi-freestanding graphene was proven by an increase in the graphene component in the C 1s XPS spectra, together with a decrease of the components associated with the buffer layer. Furthermore, the intercalation of platinum led to the formation of PtSi, Pt₂Si, and Pt₃Si, as visible in the Pt 4f and Si 2p spectra. Small signals of these silicides were already present before annealing, which shows that part of the platinum did intercalate even without thermal activation. After intercalation, the substrate stays in direct contact with the Pt-layer, which changes the coulomb environment of its uppermost layers. As a consequence, two additional components appeared in the C 1s and the Si 2p spectra, reflecting these layers [47, 72, 213, 214].

The intercalation of cobalt caused a (1×1) $R30^\circ$ -reconstruction with respect to the graphene pattern to appear in the LEED image, which was attributed to the intercalated Co-layer [209]. Next to it, only the graphene pattern reappeared. All other former spots remained absent. This is due to the high thickness of the the Co-layer preventing low-energy electrons from traveling through it, resulting in the absence of diffraction signal of the deeper buried layers. The XPS spectra indicated that there were no chemical changes resulting from the intercalation process, specifically no formation of cobalt-silicide. Thus, the subsequent intercalation of platinum successfully prevented these formations from occurring. To prove the intercalation, ARXPS spectra were taken. These show that the graphene layer is positioned above the Co-layer after annealing. In summary, the sample system was prepared as desired. It is expected that the absence of cobalt-silicides and the crystalline structure of the layers are of significant advantage for the formation of magnetic structural features.

Finally, the magnetic structure of the embedded Co-layer was investigated using X-PEEM in combination with XMCD at the Co L₃-edge. First and foremost, numerous merons and bimerons were detected for all samples analyzed.

The chemical contrast images showed the system's step edges and surface defects. The defects represent Pt remaining on the surface, even after intercalation. The comparison of samples prepared *in-situ* and *ex-situ* showed that these initially small and numerous defects merge into larger ones due to additional annealing. High step edges cause the accumulation of cobalt in small regions in which the surface is continuously covered. The height of the steps seem to impede an even distribution of cobalt on their surface. Samples with flatter steps show no cobalt accumulation. Moreover, flatter steps causes cobalt to cover many segments across the step edges. In the area with Co accumulation, i.e., where the Co-layer is thicker, there are no magnetic vortices due to reduced DMI. It appeared more like a magnetic bulk structure.

As proven by XAS intensity spectra, the local chemical properties of the Co-layer do not differ in the region of terraces, step edges, or defects. Its magnetic structure also does not correlate with the step edges or defects. It is particularly noteworthy that the positions of the dot defects do not correlate with those of the merons or bimerons. This excludes pinning with a contribution of the defects. Consequently, the systems merons and bimerons are solely stable due to topological protection.

Furthermore, all samples were found to be primarily in-plane magnetized. The absence of PMA is associated with the PtSi bonds, as they are the main difference from similar systems with PMA.

Regarding the domains of the in-plane and the out-of-plane component, samples prepared using CCS showed the two magnetic components to be connected. This was not the case for samples prepared using PASG. It is possible that the relative strength of the two components is different for the samples prepared by the two methods. Further research is needed to answer this question, such as investigating more Co-layer thicknesses.

Samples prepared *ex-situ* showed a magnetic structure with numerous small domains of different directions. In contrast, the magnetic structure of the sample prepared *in-situ* was primarily homogeneous, with one preferred direction and many smaller domains oriented in the opposite spin direction to the preferred one. This change from one primary spin direction to many small domains seems to be caused by the additional annealing step of the *ex-situ* samples after their reinsertion into the

vacuum. The required annealing temperature and time are relatively high, which may cause the changes in the magnetic structure. Moreover, the bimerons of the *in-situ* samples were very compact in size and appeared to be isolated. Additional annealing also changes this. Future studies could combine the advantages of a lower step high and no additional annealing and investigate the magnetic structure of samples prepared with PASG and treated *in-situ*. A capping layer could also be used to reduce the necessary temperature or time of the additional annealing step or make it obsolete at all.

In conclusion, this study comprehensively investigated the structural, chemical, and magnetic properties of the graphene/cobalt/platinum multilayer system on silicon carbide. The crystalline structure of each of the system's layers, as well as chemical bonds such as platinum silicides and an altered coulomb environment of the uppermost SiC layers, were detected. The magnetic structure of the system's Co-layer was found to host numerous merons and bimerons. Moreover, the structure itself was found to be strongly dependent on the type of preparation. These results are a solid foundation for future investigations of similar sample systems and applications in spintronics.

XPS fit parameters

In this Section, the XPS fit parameters used to generate Figures 6.8-6.11 are provided.

A.1 Carbon 1s

	$\theta/^\circ$	Comp.	E_{kin}/eV	$\Delta E_{\text{kin}}/\text{eV}$	FWHM/eV	A/%	α
G on SiC	0	graphene	161.31	0	1.06	6.6	0.112
		S1	160.97	-0.34	0.98	15.9	0
		S2	160.38	-0.93	1.02	31.8	0
		SiC	162.21	0.90	0.94	45.8	0
	60	graphene	161.23	0	1.19	21.7	0.112
		S1	160.89	-0.34	1.11	20.4	0
		S2	160.30	-0.93	1.11	40.8	0
		SiC	162.12	0.89	1.02	17.1	0
Pt/G on SiC	0	graphene	161.30	0	1.15	17.3	0.112
		S1	160.96	-0.34	1.07	15.1	0
		S2	160.36	-0.94	1.06	30.2	0
		SiC	162.19	0.89	0.82	37.4	0
	60	graphene	161.16	0	1.02	36.7	0.112
		S1	160.88	-0.28	1.07	15.9	0
		S2	160.28	-0.88	1.06	31.7	0
		SiC	162.12	0.97	0.98	15.8	0

	$\Theta/^\circ$	Comp.	E_{kin}/eV	$\Delta E_{\text{kin}}/\text{eV}$	FWHM/eV	A/%	α
G/Pt on SiC	0	graphene	161.31	0	0.74	69.8	0.112
		S1	160.98	-0.34	0.86	2.2	0
		S2	160.39	-0.93	0.86	4.4	0
		SiC	162.21	0.89	0.78	5.9	0
		SiC'	162.74	1.42	0.78	6.3	0
		SiC''	163.30	1.99	0.78	11.5	0
	60	graphene	161.19	0	0.74	87.7	0.112
	S1	160.85	-0.34	0.86	1.8	0	
	S2	160.26	-0.93	0.86	3.7	0	
	SiC	162.08	0.89	0.78	0.6	0	
	SiC'	162.61	1.41	0.78	1.4	0	
	SiC''	163.18	1.99	0.78	4.8	0	
Co/G/Pt on SiC	0	graphene	161.52	0	0.66	78.5	0.112
		S1	161.18	-0.34	0.86	1.1	0
		S2	160.59	-0.93	0.86	2.1	0
		SiC	162.43	0.90	0.78	2.6	0
		SiC'	162.95	1.43	0.78	4.8	0
		SiC''	163.43	1.90	0.78	10.9	0
	60	graphene	161.48	0	0.74	89.5	0.112
	S1	161.14	-0.34	0.74	1.1	0	
	S2	160.55	-0.93	0.74	2.2	0	
	SiC	162.37	0.89	0.66	1.1	0	
	SiC'	162.90	1.42	0.66	2.7	0	
	SiC''	163.37	1.89	0.66	3.5	0	

	$\Theta/^\circ$	Comp.	E_{kin}/eV	$\Delta E_{\text{kin}}/\text{eV}$	FWHM/eV	A/%	α
G/Co/Pt on SiC	0	graphene	161.47	0	0.74	85.2	0.112
		SiC	162.37	0.90	0.74	3.3	0
		SiC'	163.31	1.84	0.74	6.4	0
		SiC''	162.89	1.43	0.74	5.2	0
	60	graphene	161.48	0	0.78	95.4	0.112
		SiC	162.37	0.90	0.74	1.2	0
		SiC'	163.32	1.84	0.70	2.2	0
		SiC''	162.90	1.43	0.70	1.2	0

Table A.1: Parameters for fitting the C 1s XPS spectra shown in Figures 6.8.

A.2 Silicon 2p

	$\theta/^\circ$	Comp.	E_{kin}/eV	$\Delta E_{\text{kin}}/\text{eV}$	FWHM/eV	A/%	α	E_{SOC}/eV
G on SiC	0	SiC	74.85	0	0.65	95.8	0	0.61
		$6\sqrt{3}$	74.33	-0.52	0.65	4.2	0	0.61
	60	SiC	74.87	0	0.68	95.1	0	0.61
		$6\sqrt{3}$	74.35	-0.52	0.68	4.9	0	0.61
Pt/G on SiC	0	SiC	74.90	0	0.70	98.2	0	0.61
		$6\sqrt{3}$	74.38	-0.52	0.71	1.8	0	0.61
	60	SiC	74.91	0	0.78	98.3	0	0.61
		$6\sqrt{3}$	74.39	-0.52	0.78	1.7	0	0.61
G/Pt on SiC	0	SiC	74.84	0	0.72	23.4	0	0.61
		$6\sqrt{3}$	74.32	-0.52	0.73	2.1	0	0.61
		SiC'	74.04	-0.80	0.72	1.6	0	0.61
		SiC''	73.37	-1.47	0.73	0.4	0	0.61
		Si-Si	75.36	0.52	0.73	18.7	0	0.61
		Pt ₁ Si	75.87	1.03	0.60	27.4	0	0.61
		Pt ₂ Si	76.54	1.70	0.60	16.9	0	0.61
		Pt ₃ Si	76.94	2.10	0.52	9.1	0	0.61
		Si ⁴⁺	71.44	-3.40	0.45	0.4	0	-
	60	SiC	74.80	0	0.75	19.2	0	0.61
		$6\sqrt{3}$	74.28	-0.52	0.75	1.2	0	0.61
		SiC'	74.00	-0.80	0.75	2.8	0	0.61
		SiC''	73.33	-1.47	0.75	2.1	0	0.61
60	Si-Si	75.32	0.52	0.75	17.3	0	0.61	
	Pt ₁ Si	75.83	1.03	0.63	27.8	0	0.61	
	Pt ₂ Si	76.50	1.70	0.63	21.0	0	0.61	
	Pt ₃ Si	76.90	2.10	0.54	8.1	0	0.61	
		Si, Sat	71.40	-3.40	0.45	0.5	0	-

$\theta/^\circ$	Comp.	E_{kin}/eV	$\Delta E_{\text{kin}}/\text{eV}$	FWHM/eV	A/%	α	E_{SOC}/eV
0	SiC	75.16	0	0.70	15.5	0	0.61
	$6\sqrt{3}$	74.64	-0.52	0.71	1.6	0	0.61
	SiC'	74.36	-0.80	0.70	2.3	0	0.61
	SiC''	73.69	-1.47	0.70	1.5	0	0.61
	Si-Si	75.68	0.52	0.71	19.4	0	0.61
	Pt ₁ Si	76.19	1.03	0.59	23.9	0	0.61
	Pt ₂ Si	76.86	1.70	0.59	17.6	0	0.61
	Pt ₃ Si	77.26	2.10	0.51	10.7	0	0.61
	Si, Sat	71.13	-3.40	0.45	0.6	0	-
	Si ³⁺	73.05	-2.11	1.06	0	0	0.61
	Co3s	76.11	0.95	1.26	7.0	0.31	0.6
	60	SiC	75.15	0	0.82	18.6	0
$6\sqrt{3}$		74.63	-0.52	0.83	1.9	0	0.61
SiC'		74.35	-0.80	0.82	6.8	0	0.61
SiC''		73.68	-1.47	0.82	4.9	0	0.61
Si-Si		75.66	0.51	0.82	14.2	0	0.61
Pt ₁ Si		76.18	1.03	0.67	18.6	0	0.61
Pt ₂ Si		76.85	1.70	0.70	17.4	0	0.61
Pt ₃ Si		77.25	2.10	0.60	8.5	0	0.61
Si, Sat		71.75	-3.40	0.53	0.7	0	-
Si ³⁺		73.04	-2.11	1.06	1.9	0	0.61
Co3s		76.10	0.95	1.39	6.6	0.31	0.6

$\Theta/^\circ$	Comp.	E_{kin}/eV	$\Delta E_{\text{kin}}/\text{eV}$	FWHM/eV	A/%	α	E_{SOC}/eV
0	SiC	75.00	0	0.75	11.8	0	0.61
	$6\sqrt{3}$	74.48	-0.52	0.75	0	0	0.61
	SiC'	74.20	-0.80	0.75	2.9	0	0.61
	SiC''	73.50	-1.50	0.74	1.8	0	0.61
	Si-Si	75.52	0.51	0.75	28.6	0	0.61
	Pt ₁ Si	76.03	1.03	0.60	24.0	0	0.61
	Pt ₂ Si	76.78	1.77	0.63	16.7	0	0.61
	Pt ₃ Si	77.10	2.10	0.54	8.1	0	0.61
	Si, Sat	71.63	-3.38	0.49	1.3	0	-
	Si ³⁺	72.90	-2.11	0.98	1.5	0	0.61
	Co3s	75.95	0.95	1.31	3.4	0.31	0.6
	60	SiC	74.98	0	0.73	11.3	0
$6\sqrt{3}$		74.46	-0.52	0.73	0	0	0.61
SiC'		74.18	-0.80	0.78	6.1	0	0.61
SiC''		73.48	-1.50	0.78	5.5	0	0.61
Si-Si		75.49	0.51	0.73	22.9	0	0.61
Pt ₁ Si		76.01	1.03	0.60	20.5	0	0.61
Pt ₂ Si		76.72	1.74	0.60	17.3	0	0.61
Pt ₃ Si		77.08	2.10	0.55	7.8	0	0.61
Si, Sat		71.66	-3.32	0.49	1.5	0	-
Si ³⁺		72.86	-2.12	0.95	4.9	0	0.61
Co3s		75.93	0.95	1.27	2.2	0.31	0.6

Table A.2: Parameters for fitting the Si 2p XPS spectra shown in Figures 6.9.

A.3 Platinum 4f

	$\theta/^\circ$	Comp.	E_{kin}/eV	$\Delta E_{\text{kin}}/\text{eV}$	FWHM/eV	A/%	α	E_{SOC}/eV
Pt/G on SiC	0	Pt	185.05	0	0.99	69.8	0.09	3.31
		Pt ₃ Si	184.34	-0.62	0.99	25.6	0.09	3.31
		Pt ₂ Si	183.70	-1.35	0.99	2.6	0.09	3.31
		Pt ₁ Si	183.10	-1.95	0.99	2.0	0.09	3.31
	60	Pt	184.99	0	1.02	72.1	0.09	3.31
		Pt ₃ Si	184.37	-0.62	1.02	23.3	0.09	3.31
		Pt ₂ Si	183.64	-1.35	1.02	2.5	0.09	3.31
		Pt ₁ Si	183.04	-1.95	1.04	2.1	0.09	3.31
G/Pt on SiC	0	Pt	184.87	0	0.94	0.6	0.09	3.31
		Pt ₃ Si	184.25	-0.62	0.94	9.9	0.09	3.31
		Pt ₂ Si	183.52	-1.35	0.94	81.3	0.09	3.31
		Pt ₁ Si	182.92	-1.95	0.94	8.2	0.09	3.31
	60	Pt	185.16	0	0.92	0.7	0.09	3.31
		Pt ₃ Si	184.54	-0.62	0.92	11.0	0.09	3.31
		Pt ₂ Si	183.81	-1.35	0.91	77.6	0.09	3.31
		Pt ₁ Si	183.21	-1.95	0.92	10.7	0.09	3.31
Co/G/Pt on SiC	0	Pt	185.33	0	0.87	0.8	0.09	3.31
		Pt ₃ Si	184.71	-0.62	0.87	11.4	0.09	3.31
		Pt ₂ Si	183.98	-1.35	0.87	78.2	0.09	3.31
		Pt ₁ Si	183.38	-1.95	0.87	9.7	0.09	3.31
	60	Pt	185.33	0	1.01	0.7	0.09	3.31
		Pt ₃ Si	184.71	-0.62	1.01	12.7	0.09	3.31
		Pt ₂ Si	183.98	-1.35	1.00	79.7	0.09	3.31
		Pt ₁ Si	183.38	-1.95	1.00	6.9	0.09	3.31

	$\Theta/^\circ$	Comp.	E_{kin}/eV	$\Delta E_{\text{kin}}/\text{eV}$	FWHM/eV	A/%	α	E_{SOC}/eV
G/Co/Pt on SiC	0	Pt	185.27	0	0.88	0.6	0.09	3.31
		Pt ₃ Si	184.65	-0.62	0.87	5.8	0.09	3.31
		Pt ₂ Si	183.92	-1.35	0.88	83.6	0.09	3.31
		Pt ₁ Si	183.32	-1.95	0.88	10.0	0.09	3.31
	60	Pt	185.24	0	0.92	0.9	0.09	3.31
		Pt ₃ Si	184.62	-0.62	0.92	5.9	0.09	3.31
		Pt ₂ Si	183.89	-1.35	0.91	82.5	0.09	3.31
		Pt ₁ Si	132.28	-1.95	0.91	10.6	0.09	3.31

Table A.3: Parameters for fitting the Pt 4f XPS spectra shown in Figures 6.10.

The height ratio is between 0.74 and 0.75 for all components. [223].

A.4 Cobalt 3p

	$\theta/^\circ$	Comp.	E_{kin}/eV	$\Delta E_{\text{kin}}/\text{eV}$	FWHM/eV	A/%	α	E_{SOC}/eV
Co/G/Pt on SiC	0	Co	117.62	0	1.37	73.3	0.305	0.60
		Co, Sat1	118.67	1.05	1.37	6.8	0.305	0.60
		Co, Sat2	116.27	-1.35	1.37	18.0	0.305	0.60
		Pt ₁ Si	123.90	6.28	2.35	2.0	0.101	14.74
		Pt ₂ Si	123.35	5.74	2.41	0.7	0.101	14.74
		Pt ₃ Si	124.48	6.86	1.77	0.2	0.101	14.74
		Co/G/Pt on SiC	60	Co	117.50	0	1.45	74.0
Co, Sat1	118.55			1.05	1.45	6.9	0.305	0.60
Co, Sat2	116.15			-1.35	1.45	18.0	0.305	0.60
Pt ₁ Si	123.78			6.28	2.57	1.0	0.101	14.74
Pt ₂ Si	123.24			5.74	2.52	0.1	0.101	14.74
Pt ₃ Si	124.37			6.86	1.99	0.1	0.101	14.74
G/Co/Pt on SiC	0			Co	117.11	0	1.74	58.7
		Co, Sat1	118.16	1.05	1.73	5.5	0.305	0.60
		Co, Sat2	116.76	-1.35	1.73	11.7	0.305	0.60
		Pt ₁ Si	123.39	6.28	2.70	19.9	0.101	14.74
		Pt ₂ Si	122.85	5.74	2.67	2.3	0.101	14.74
		Pt ₃ Si	123.98	6.86	2.46	2.0	0.101	14.74
		G/Co/Pt on SiC	60	Co	117.22	0	1.73	63.8
Co, Sat1	118.27			1.05	1.73	5.9	0.305	0.60
Co, Sat2	115.87			-1.35	1.73	12.7	0.305	0.60
Pt ₁ Si	123.50			6.28	2.72	14.5	0.101	14.74
Pt ₂ Si	122.95			5.74	2.67	1.7	0.101	14.74
Pt ₃ Si	124.08			6.86	2.36	1.4	0.101	14.74

Table A.4: Parameters for fitting the Co 3p XPS spectra shown in Figures 6.11.

For all Co components, the height ratio is 0.6. The height ratio of all Pt components is 0.75.

Solution to the equation system used to calculate the surface magnetization components using X-PEEM data

B

As discussed in Section 3.3.2, combining X-PEEM images recorded at three equidistant angles ϕ leads to an analytically solvable system of equations regarding Equation 3.16. In the present study, images were taken at 0° , 90° , and 180° . As a result, \tilde{m}_\parallel , ϕ_0 , and \tilde{m}_\perp can be determined for each pixel of the field of view. The resulting images can be analyzed, e.g., for the relative strength of the in- and out-of-plane components and for structures.

The solution to the equation system is presented in the following. The data were normalized, which reduced the range of values for the in- and out-of-plane components. For the sake of simplicity, I is always used instead of I_{XMCD} .

\tilde{m}_\parallel : In-plane magnetization strength; $\tilde{m}_\parallel \in [0, 1]$

ϕ_0 : In-plane orientation; $\phi_0 \in [0, 2\pi)$

\tilde{m}_\perp : Out-of-plane magnetization strength; $\tilde{m}_\perp \in [-1, 1]$

The equation system is given by:

$$\text{I} \quad I(0^\circ) = m_{\parallel} \cdot \cos(0^\circ + \phi_0) + \tilde{m}_{\perp} \quad (\text{B.1})$$

$$\text{II} \quad I(90^\circ) = m_{\parallel} \cdot \cos(90^\circ + \phi_0) + \tilde{m}_{\perp} \quad (\text{B.2})$$

$$\text{III} \quad I(180^\circ) = m_{\parallel} \cdot \cos(180^\circ + \phi_0) + \tilde{m}_{\perp} \quad (\text{B.3})$$

$$\text{I} \quad I(0^\circ) = m_{\parallel} \cdot \cos(\phi_0) + \tilde{m}_{\perp} \quad (\text{B.4})$$

$$\text{II} \quad I(90^\circ) = -m_{\parallel} \cdot \sin(\phi_0) + \tilde{m}_{\perp} \quad (\text{B.5})$$

$$\text{III} \quad I(180^\circ) = -m_{\parallel} \cdot \cos(\phi_0) + \tilde{m}_{\perp} \quad (\text{B.6})$$

$$(\text{I+III})/2 \quad \tilde{m}_{\perp} = \frac{I(0^\circ) + I(180^\circ)}{2} \quad (\text{B.7})$$

$$\text{I} \quad I(0^\circ) = m_{\parallel} \cdot \cos(\phi_0) + \frac{I(0^\circ) + I(180^\circ)}{2} \quad (\text{B.8})$$

$$\Leftrightarrow \quad m_{\parallel} \cdot \cos(\phi_0) = \frac{I(0^\circ) - I(180^\circ)}{2} \quad (\text{B.9})$$

$$\text{II} \quad I(90^\circ) = -m_{\parallel} \cdot \sin(\phi_0) + \frac{I(0^\circ) + I(180^\circ)}{2} \quad (\text{B.10})$$

$$\Leftrightarrow \quad m_{\parallel} \cdot \sin(\phi_0) = \frac{I(0^\circ) + I(180^\circ) - 2 \cdot I(90^\circ)}{2} \quad (\text{B.11})$$

In the following, three different cases and associated sub-cases are analyzed separately.

Case 1: $I(0^\circ) = I(180^\circ)$

$$1.1 \quad m_{\parallel} = 0 \Leftrightarrow I(0^\circ) = I(180^\circ) = I(90^\circ) = \tilde{m}_{\perp} \quad (\text{B.12})$$

$$\Rightarrow \quad \phi_0: \text{Undefined}$$

$$1.2 \quad \phi_0 \in \left\{ \frac{\pi}{2}; \frac{3\pi}{2} \right\} \Leftrightarrow I(0^\circ) = I(180^\circ) = \tilde{m}_{\perp} \neq I(90^\circ) \quad (\text{B.13})$$

$$1.2.1 \quad \phi_0 = \frac{\pi}{2} \Rightarrow \sin(\phi_0) = 1 \quad (\text{B.14})$$

$$\text{II} \quad m_{\parallel} = \frac{I(0^\circ) + I(180^\circ) - 2 \cdot I(90^\circ)}{2} \quad (\text{B.15})$$

$$1.2.2 \quad \phi_0 = \frac{3\pi}{2} \Rightarrow \sin(\phi_0) = -1 \quad (\text{B.16})$$

$$\text{II} \quad m_{\parallel} = \frac{2 \cdot I(90^\circ) - (I(0^\circ) + I(180^\circ))}{2} \quad (\text{B.17})$$

The condition $m_{\parallel} > 0$ can be used to determine whether Case 1.2.1 or Case 1.2.2 is present:

$$\begin{aligned} I(0^\circ) + I(180^\circ) - 2 \cdot I(90^\circ) &> 0 \\ \Rightarrow 1.2.1 \quad \phi_0 &= \frac{\pi}{2} \end{aligned} \quad (\text{B.18})$$

$$\begin{aligned} I(0^\circ) + I(180^\circ) - 2 \cdot I(90^\circ) &< 0 \\ \Rightarrow 1.2.2 \quad \phi_0 &= \frac{3\pi}{2} \end{aligned} \quad (\text{B.19})$$

$$\begin{aligned} \text{Case 2:} \quad & I(0^\circ) + I(180^\circ) - 2 \cdot I(90^\circ) = 0 \wedge I(0^\circ) \neq I(180^\circ) \neq I(90^\circ) \\ & \Rightarrow \phi_0 \in \{0; \pi\} \end{aligned} \quad (\text{B.20})$$

$$2.1 \quad \phi_0 = 0 \Rightarrow m_{\parallel} = \frac{I(0^\circ) - I(180^\circ)}{2} \quad (\text{B.21})$$

$$2.2 \quad \phi_0 = \pi \Rightarrow m_{\parallel} = \frac{I(180^\circ) - I(0^\circ)}{2} \quad (\text{B.22})$$

Again, the condition $m_{\parallel} > 0$ can be used to determine whether Case 2.1 or Case 2.2 is present:

$$\begin{aligned} I(0^\circ) - I(180^\circ) &> 0 \\ &\Rightarrow 2.1 \phi_0 = 0 \end{aligned} \quad (\text{B.23})$$

$$\begin{aligned} I(0^\circ) - I(180^\circ) &< 0 \\ &\Rightarrow 2.2 \phi_0 = \pi \end{aligned} \quad (\text{B.24})$$

$$\text{Case 3:} \quad I(0^\circ) \neq I(180^\circ) \neq I(90^\circ) \wedge I(0^\circ) + I(180^\circ) - 2 \cdot I(90^\circ) \neq 0$$

$$\text{II/I} \quad \tan(\phi_0) = \frac{I(0^\circ) + I(180^\circ) - 2 \cdot I(90^\circ)}{I(0^\circ) - I(180^\circ)} \quad (\text{B.25})$$

$$\phi_0 = \arctan\left(\frac{I(0^\circ) + I(180^\circ) - 2 \cdot I(90^\circ)}{I(0^\circ) - I(180^\circ)}\right) \quad (\text{B.26})$$

The range of values for $\arctan(x)$ is limited to $(-\frac{\pi}{2}; \frac{\pi}{2})$. Other angles can be determined using Equations (B.9) and (B.11), and the condition $\tilde{m}_{\perp} > 0$ as described in the following:

3.1:

$$I(0^\circ) - I(180^\circ) > 0 \quad \text{I} \Rightarrow \phi_0 \in (0; \pi/2) \vee (3\pi/2; 2\pi) \quad (\text{B.27})$$

\wedge

$$I(0^\circ) + I(180^\circ) - 2 \cdot I(90^\circ) > 0 \quad \text{II} \Rightarrow \phi_0 \in (0; \pi) \quad (\text{B.28})$$

$$\Rightarrow \phi_0 \in (0; \pi/2) \quad (\text{B.29})$$

3.2:

$$I(0^\circ) - I(180^\circ) > 0 \quad \text{I} \Rightarrow \phi_0 \in (0; \pi/2) \vee (3\pi/2; 2\pi) \quad (\text{B.30})$$

\wedge

$$I(0^\circ) + I(180^\circ) - 2 \cdot I(90^\circ) < 0 \quad \text{II} \Rightarrow \phi_0 \in (\pi; 2\pi) \quad (\text{B.31})$$

$$\Rightarrow \phi_0 \in (3\pi/2; 2\pi) \quad (\text{B.32})$$

3.3:

$$I(0^\circ) - I(180^\circ) < 0 \quad \text{I} \Rightarrow \phi_0 \in (\pi/2; 3\pi/2) \quad (\text{B.33})$$

\wedge

$$I(0^\circ) + I(180^\circ) - 2 \cdot I(90^\circ) > 0 \quad \text{II} \Rightarrow \phi_0 \in (0; \pi) \quad (\text{B.34})$$

$$\Rightarrow \phi_0 \in (\pi/2; \pi) \quad (\text{B.35})$$

3.4:

$$I(0^\circ) - I(180^\circ) < 0 \quad \text{I} \Rightarrow \phi_0 \in (\pi/2; 3\pi/2) \quad (\text{B.36})$$

\wedge

$$I(0^\circ) + I(180^\circ) - 2 \cdot I(90^\circ) < 0 \quad \text{II} \Rightarrow \phi_0 \in (\pi; 2\pi) \quad (\text{B.37})$$

$$\Rightarrow \phi_0 \in (\pi; 3\pi/2) \quad (\text{B.38})$$

The angles calculated using Equation (B.26) have to be corrected:

$$3.1: \quad \phi_0 = \phi_{\text{calculated}} \quad (\text{B.39})$$

$$3.2: \quad \phi_0 = \phi_{\text{calculated}} + 2\pi \quad (\text{B.40})$$

$$3.3: \quad \phi_0 = \phi_{\text{calculated}} + \pi \quad (\text{B.41})$$

$$3.4: \quad \phi_0 = \phi_{\text{calculated}} + \pi \quad (\text{B.42})$$

Lastly, m_{\parallel} can be determined using Equations (B.9) or (B.11):

$$\text{I} \quad m_{\parallel} = \frac{I(0^\circ) - I(180^\circ)}{2 \cdot \cos(\phi_0)} \quad (\text{B.43})$$

or

$$\text{II} \quad m_{\parallel} = \frac{I(0^\circ) + I(180^\circ) - 2 \cdot I(90^\circ)}{2 \cdot \sin(\phi_0)} \quad (\text{B.44})$$

Overview of the X-PEEM images

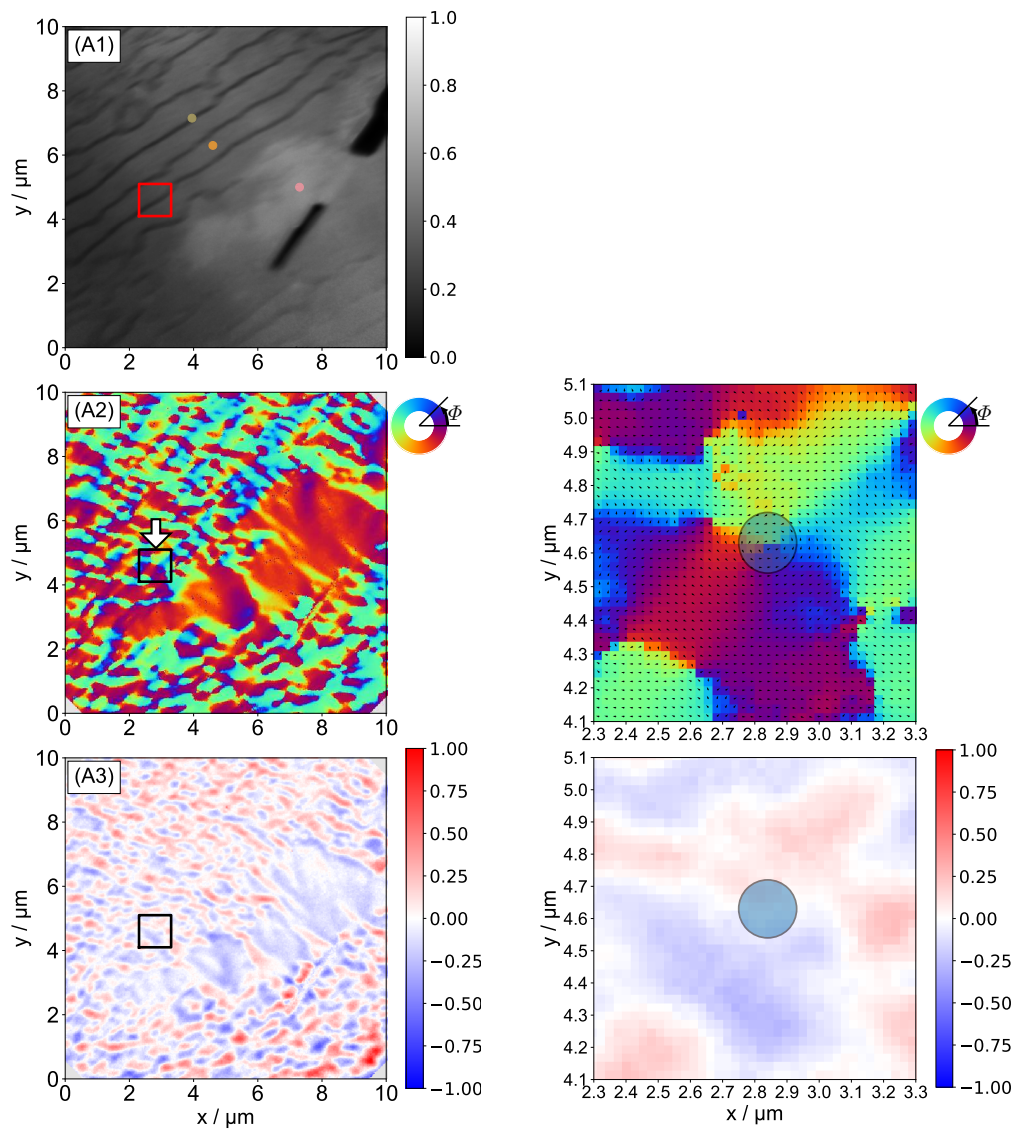


Figure C.1: Overview of the X-PEEM images and close-ups of sample A.

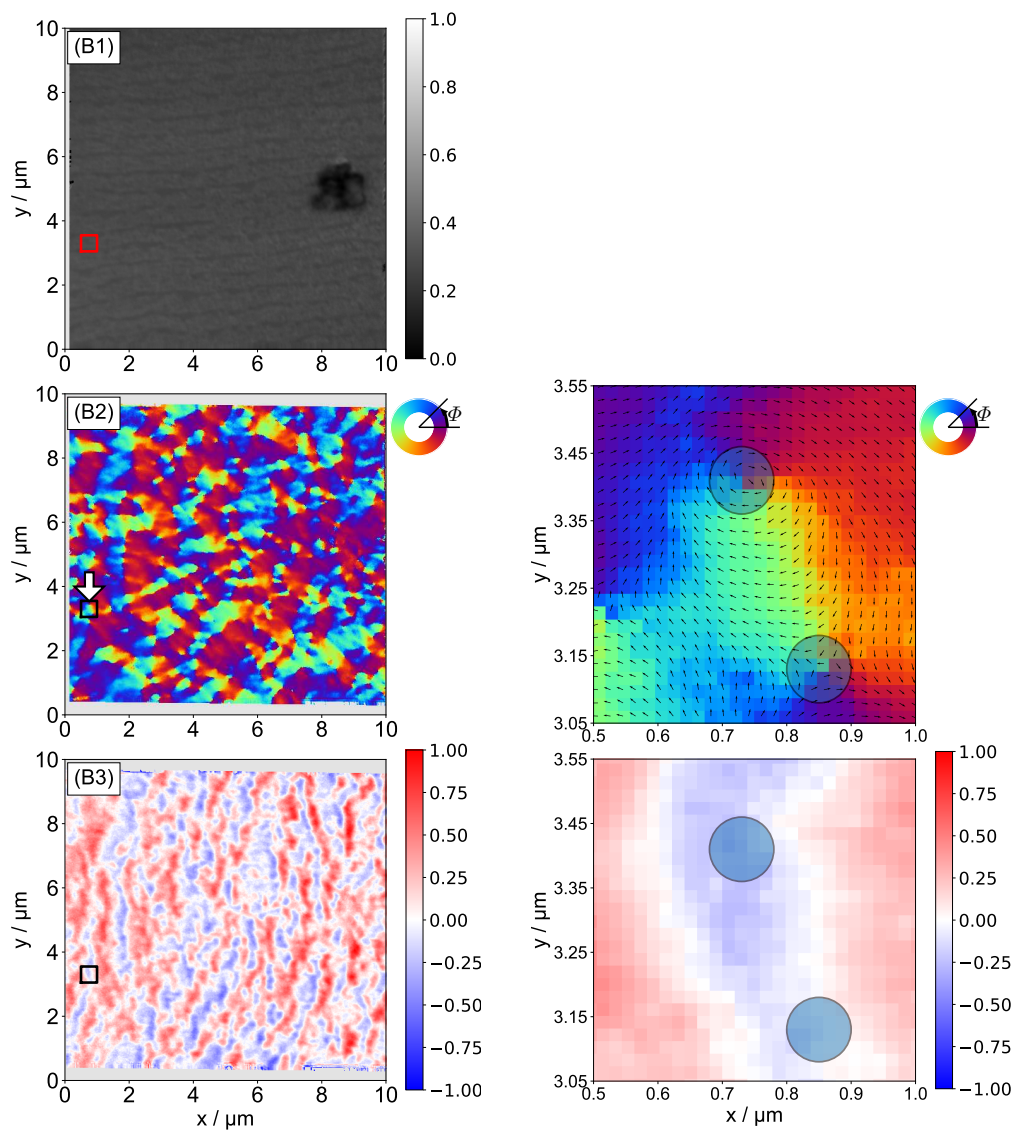


Figure C.2: Overview of the X-PEEM images and close-ups of sample **B**.

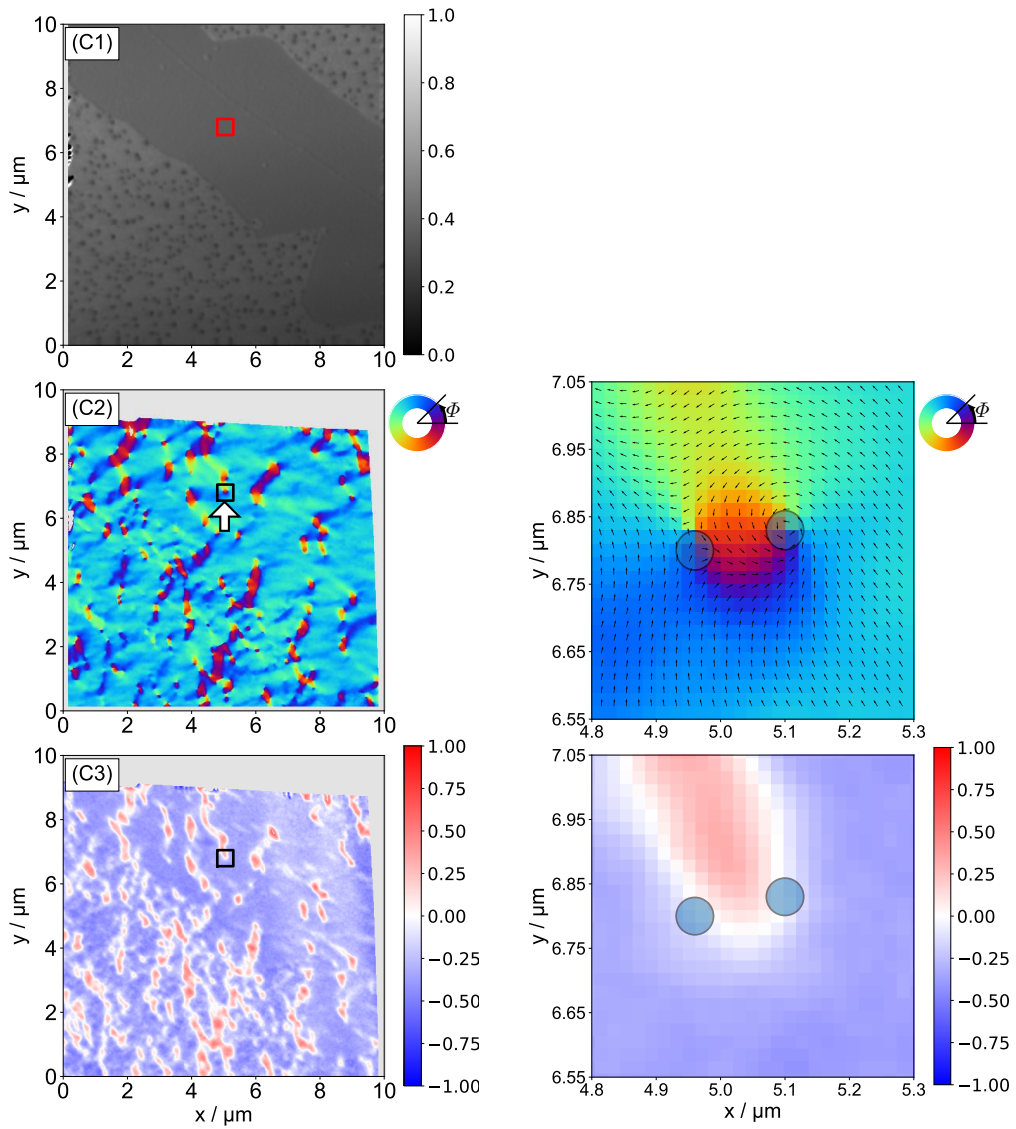


Figure C.3: Overview of the X-PEEM images and close-ups of sample C.

Appendix

Bibliography

- [1] P. Weinert, J. A. Hochhaus, L. Kesper, R. Appel, S. Hilgers, M. Schmitz, M. G. H. Schulte, R. Hönig, F. Kronast, S. Valencia, M. Kruskopf, A. Chatterjee, U. Berges, and C. Westphal, *Structural, chemical, and magnetic investigation of a graphene/cobalt/platinum multilayer system on silicon carbide*, Nanotechnology, Accepted Manuscript (Status: Jan. 11, 2024).
- [2] L. B. Kish, *End of Moore's law: thermal (noise) death of integration in micro and nano electronics*, Phys. Lett. A **305**, 144 (2002).
- [3] S. A. Wolf, D. D. Awschalom, R. A. Buhrman, J. M. Daughton, S. von Molnár, M. L. Roukes, A. Y. Chtchelkanova, and D. M. Treger, *Spintronics: A Spin-Based Electronics Vision for the Future*, Science **294**, 1488 (2001).
- [4] A. Hirohata and K. Takanashi, *Future perspectives for spintronic devices*, J. Phys. D Appl. Phys. **47**, 193001 (2014).
- [5] E. C. Ahn, *2D materials for spintronic devices*, npj 2D Mater. Appl. **4**, 17 (2020).
- [6] A. Makarov, T. Windbacher, V. Sverdlov, and S. Selberherr, *CMOS-compatible spintronic devices: a review*, Semicond. Sci. Tech. **31**, 113006 (2016).
- [7] P. J. Rajput, S. U. Bhandari, and G. Wadhwa, *A Review on—Spintronics an Emerging Technology*, Silicon **14**, 9195 (2022).
- [8] M. N. Baibich, J. M. Broto, A. Fert, F. N. Van Dau, F. Petroff, P. Etienne, G. Creuzet, A. Friederich, and J. Chazelas, *Giant magnetoresistance of (001) Fe/(001) Cr magnetic superlattices*, Phys. Rev. Lett. **61**, 2472 (1988).

- [9] G. Binasch, P. Grünberg, F. Saurenbach, and W. Zinn, *Enhanced magnetoresistance in layered magnetic structures with antiferromagnetic interlayer exchange*, Phys. Rev. B **39**, 4828 (1989).
- [10] S. Parkin, Z. Li, and D. J. Smith, *Giant magnetoresistance in antiferromagnetic Co/Cu multilayers*, Appl. Phys. Lett. **58**, 2710 (1991).
- [11] M. Julliere, *Tunneling between ferromagnetic films*, Phys. Lett. A **54**, 225 (1975).
- [12] R. Meservey and P. Tedrow, *Spin-polarized electron tunneling*, Phys. Rep. **238**, 173 (1994).
- [13] J. S. Moodera, L. R. Kinder, T. M. Wong, and R. Meservey, *Large magnetoresistance at room temperature in ferromagnetic thin film tunnel junctions*, Phys. Rev. Lett. **74**, 3273 (1995).
- [14] D. Apalkov, B. Dieny, and J. M. Slaughter, *Magnetoresistive random access memory*, Proc. IEEE **104**, 1796 (2016).
- [15] P. P. Freitas, Ferreira, R., and S. Cardoso, *Spintronic sensors*, Proc. IEEE **104**, 1894 (2016).
- [16] F. Ajejas, A. Gudín, R. Guerrero, A. A. Barcelona, J. M. Diez, L. de Melo Costa, P. Olleros, M. Angel Niño, S. Pizzini, J. Vogel, M. Valvidares, P. Gargiani, M. Cabero, M. Varela, J. Camarero, R. Miranda, and P. Perna, *Unraveling Dzyaloshinskii–Moriya Interaction and Chiral Nature of Graphene/Cobalt Interface*, Nano Lett. **18**, 5364 (2018).
- [17] W. Han, R. K. Kawakami, M. Gmitra, and J. Fabian, *Graphene spintronics*, Nat. Nanotechnol. **9**, 794 (2014).
- [18] Q. Tang and Z. Zhou, *Graphene-analogous low-dimensional materials*, Prog. Mater. Sci. **58**, 1244 (2013).
- [19] Y.-M. Lin, C. Dimitrakopoulos, K. A. Jenkins, D. B. Farmer, H.-Y. Chiu, A. Grill, and P. Avouris, *100-GHz transistors from wafer-scale epitaxial graphene*, Science **327**, 662 (2010).

- [20] K. S. Novoselov, A. K. Geim, S. V. Morozov, D. Jiang, Y. Zhang, S. V. Dubonos, I. V. Grigorieva, and A. A. Firsov, *Electric Field Effect in Atomically Thin Carbon Films*, Science **306**, 666 (2004).
- [21] A. K. Geim, *Nobel Lecture: Random walk to graphene*, Rev. Mod. Phys. **83**, 851 (2011).
- [22] K. V. Emtsev, A. Bostwick, K. Horn, J. Jobst, G. L. Kellogg, L. Ley, J. L. McChesney, T. Ohta, S. A. Reshanov, J. Röhrhl, E. Rotenberg, A. K. Schmid, D. Waldmann, H. B. Weber, and T. Seyller, *Towards wafer-size graphene layers by atmospheric pressure graphitization of silicon carbide*, Nat. Mater. **8**, 203 (2009).
- [23] W. A. De Heer, C. Berger, M. Ruan, M. Sprinkle, X. Li, Y. Hu, B. Zhang, J. Hankinson, and E. Conrad, *Large area and structured epitaxial graphene produced by confinement controlled sublimation of silicon carbide*, Proc. Natl Acad. Sci. USA **108**, 16900 (2011).
- [24] H. Yang, G. Chen, A. A. Cotta, A. T. N'Diaye, S. A. Nikolaev, E. A. Soares, W. A. Macedo, K. Liu, A. K. Schmid, A. Fert, and M. Chshiev, *Significant Dzyaloshinskii–Moriya interaction at graphene–ferromagnet interfaces due to the Rashba effect*, Nat. Mater. **17**, 605 (2018).
- [25] E. D. Cobas, O. M. J. van't Erve, S.-F. Cheng, J. C. Culbertson, G. G. Jernigan, K. Bussman, and B. T. Jonker, *Room-Temperature Spin Filtering in Metallic Ferromagnet–Multilayer Graphene–Ferromagnet Junctions*, ACS nano **10**, 10357 (2016).
- [26] R. Decker, J. Brede, N. Atodiresei, V. Caciuc, S. Blügel, and R. Wiesendanger, *Atomic-scale magnetism of cobalt-intercalated graphene*, Phys. Rev. B **87**, 041403 (2013).
- [27] A.-D. Vu, J. Coraux, G. Chen, A. T. N'Diaye, A. K. Schmid, and N. Rougemaille, *Unconventional magnetisation texture in graphene/cobalt hybrids*, Sci. Rep. **6**, 24783 (2016).
- [28] H. Yang, A. D. Vu, A. Hallal, N. Rougemaille, J. Coraux, G. Chen, A. K. Schmid, and M. Chshiev, *Anatomy and giant enhancement of the perpendicular*

- magnetic anisotropy of cobalt-graphene heterostructures*, Nano Lett. **16**, 145 (2016).
- [29] S. Fukami, T. Anekawa, C. Zhang, and H. Ohno, *A spin-orbit torque switching scheme with collinear magnetic easy axis and current configuration*, Nat. Nanotechnol. **11**, 621 (2016).
- [30] A. Moser, K. Takano, D. T. Margulies, M. Albrecht, Y. Sonobe, Y. Ikeda, S. Sun, and E. E. Fullerton, *Magnetic recording: advancing into the future*, J. Phys. D Appl. Phys. **35**, R157 (2002).
- [31] I. M. Miron, K. Garello, G. Gaudin, P.-J. Zermatten, M. V. Costache, S. Auffret, S. Bandiera, B. Rodmacq, S. Schuhl, and P. Gambardella, *Perpendicular switching of a single ferromagnetic layer induced by in-plane current injection*, Nature **476**, 189– (2011).
- [32] P. Barlia, V. K. Joshi, and S. Bhat, *Spintronic devices: a promising alternative to CMOS devices*, J. Comput. Electron. 805–37 (2021).
- [33] T. Hanyu, T. Endoh, D. Suzuki, H. Koike, Y. Ma, N. Onizawa, M. Natsui, S. Ikeda, and H. Ohno, *Standby-Power-Free Integrated Circuits Using MTJ-Based VLSI Computing*, P. IEEE **104**, 1844 (2016).
- [34] A. Quindeau, C. O. Avci, W. Liu, C. Sun, M. Mann, A. S. Tang, M. C. Onbasli, D. Bono, P. M. Voyles, Y. Xu, J. Robinson, G. S. D. Beach, and C. A. Ross, *Tm₃Fe₅O₁₂/Pt heterostructures with perpendicular magnetic anisotropy for spintronic applications*, Adv. Electron. Mater. **3**, 1600376 (2017).
- [35] H. Naganuma, V. Zlatko, M. Galbiati, F. Godel, A. Sander, C. Carrétéro, O. Bezencenet, N. Reyren, M.-B. Martin, B. Dlubak, and P. Seneor, *A perpendicular graphene/ferromagnet electrode for spintronics*, Appl. Phys. Lett. **116**, 173101 (2020).
- [36] F. Garcia, G. Casali, S. Auffret, B. Rodmacq, and B. Dieny, *Exchange bias in (Pt/Co 0.9 Fe 0.1) *n*/FeMn multilayers with perpendicular magnetic anisotropy*, J. Appl. Phys. **91**, 6905 (2002).

- [37] N. Nakajima, T. Koide, T. Shidara, H. Miyauchi, H. Fukutani, A. Fujimori, K. Iio, T. Katayama, M. Nyvlt, and Y. Suzuki, *Perpendicular Magnetic Anisotropy Caused by Interfacial Hybridization via Enhanced Orbital Moment in Co/Pt Multilayers: Magnetic Circular X-Ray Dichroism Study*, Phys. Rev. Lett. **81**, 5229 (1998).
- [38] R. Hönig, P. Roese, K. Shamout, T. Ohkochi, U. Berges, and C. Westphal, *Structural, chemical, and magnetic properties of cobalt intercalated graphene on silicon carbide*, Nanotechnology **30**, 025702 (2018).
- [39] F. Ajejas, A. Anadon, A. Gudin, J. M. Diez, C. G. Ayani, P. Olleros-Rodríguez, L. de Melo Costa, C. Navío, A. Gutierrez, F. Calleja, A. L. Vazquez de Parga, R. Miranda, J. Camarero, and P. Perna, *Thermally Activated Processes for Ferromagnet Intercalation in Graphene-Heavy Metal Interfaces*, ACS Appl. Mater. Interfaces **12**, 4088 (2019).
- [40] C. Riedl, *Epitaxial Graphene on Silicon Carbide Surfaces: Growth, Characterization, Doping and Hydrogen Intercalation*, Ph.d. thesis, Friedrich-Alexander-Universität Erlangen-Nürnberg (2010).
- [41] M. D. Henry and C. R. Ahlers, *Platinum Diffusion Barrier Breakdown in a-Si/Au Eutectic Wafer Bonding*, IEEE T. Comp. Pack. Man. **3**, 899 (2013).
- [42] R. Madar, C. d'Anterroches, F. Arnaud d'Avitaya, D. Boursier, O. Thomas, and J. P. Senateur, *Magnetic and transmission electron microscopy studies of the formation of cobalt silicide thin films*, J. Appl. Phys. **64**, 3014 (1988).
- [43] K. Ishida, T. Nishizawa, and M. E. Schlesinger, *The Co-Si (cobalt-silicon) system*, J. Phase Equilib. **12**, 578 (1991).
- [44] G. F. Zhou and H. Bakker, *Atomically disordered nanocrystalline Co₂Si by high-energy ball milling*, J. Phys. Condensed Mat. **6**, 4043 (1994).
- [45] B. Dlubak, M.-B. Martin, C. Deranlot, B. Servet, S. Xavier, R. Mattana, M. Sprinkle, C. Berger, W. A. De Heer, F. Petroff, A. Anane, P. Seneor, and A. Fert, *Highly efficient spin transport in epitaxial graphene on SiC*, Nat. Phys. **8**, 557 (2012).

- [46] M. S. Whittingham, *Intercalation Chemistry: an introduction*, Academic Press New York, New York, 1 ed. (1982).
- [47] C. Riedl, C. Coletti, T. Iwasaki, A. A. Zakharov, and U. Starke, *Quasi-free-standing epitaxial graphene on SiC obtained by hydrogen intercalation*, Phys. Rev. Lett. **103**, 246804 (2009).
- [48] A. Varykhalov, J. Sánchez-Barriga, A. M. Shikin, C. Biswas, E. Vescovo, A. Rybkin, D. Marchenko, and O. Rader, *Electronic and magnetic properties of quasifree-standing graphene on Ni*, Phys. Rev. Lett. **101**, 157601 (2008).
- [49] B. Premlal, M. Cranney, F. Vonau, D. Aubel, D. Casterman, M. M. De Souza, and L. Simon, *Surface intercalation of gold underneath a graphene monolayer on SiC (0001) studied by scanning tunneling microscopy and spectroscopy*, Appl. Phys. Lett. **94**, 263115 (2009).
- [50] K. Shen, H. Sun, J. Hu, J. Hu, Z. Liang, H. Li, Z. Zhu, Y. Huang, L. Kong, and Y. Wang, *Fabricating quasi-free-standing graphene on a SiC (0001) surface by steerable intercalation of iron*, J. Phys. Chem C **122**, 21484 (2018).
- [51] K. Yagyu, T. Tajiri, A. Kohno, K. Takahashi, H. Tochiara, H. Tomokage, and T. Suzuki, *Fabrication of a single layer graphene by copper intercalation on a SiC (0001) surface*, Appl. Phys. Lett. **104**, 053115 (2014).
- [52] K. V. Emtsev, A. A. Zakharov, C. Coletti, S. Forti, and U. Starke, *Ambipolar doping in quasifree epitaxial graphene on SiC (0001) controlled by Ge intercalation*, Phys. Rev. B **84**, 125423 (2011).
- [53] H. Toyama, R. Akiyama, S. Ichinokura, M. Hashizume, T. Iimori, Y. Endo, R. Hobara, T. Matsui, K. Horii, and S. Sato, *Two-dimensional superconductivity of Ca-intercalated graphene on SiC: Vital role of the interface between monolayer graphene and the substrate*, ACS Nano **16**, 3582 (2022).
- [54] H. Wagner, *Long-wavelength excitations and the Goldstone theorem in many-particle systems with "broken symmetries"*, Z. Phys. **195**, 273 (1966).
- [55] J. C. Meyer, A. K. Geim, M. I. Katsnelson, K. S. Novoselov, T. J. Booth, and S. Roth, *The structure of suspended graphene sheets*, Nature **446**, 60 (2007).

- [56] Z. Zhen and H. Zhu, *Structure and properties of graphene*, in *Graphene*, Elsevier, 1–12 (2018).
- [57] P. R. Wallace, *The band theory of graphite*, Phys. Rev. **71**, 622 (1947).
- [58] S. V. Morozov, K. S. Novoselov, M. I. Katsnelson, F. Schedin, D. C. Elias, J. A. Jaszczak, and A. K. Geim, *Giant intrinsic carrier mobilities in graphene and its bilayer*, Phys. Rev. Lett. **100**, 016602 (2008).
- [59] A. K. Geim, *Graphene: Status and Prospects*, Science **324**, 1530 (2009).
- [60] C. Lee, X. Wei, J. W. Kysar, and J. Hone, *Measurement of the elastic properties and intrinsic strength of monolayer graphene*, Science **321**, 385 (2008).
- [61] M. Inagaki, Y. A. Kim, and M. Endo, *Graphene: preparation and structural perfection*, J. Mater. Chem. **21**, 3280 (2011).
- [62] C. Riedl, C. Coletti, and U. Starke, *Structural and electronic properties of epitaxial graphene on SiC (0 0 0 1): a review of growth, characterization, transfer doping and hydrogen intercalation*, J. Phys. D Appl. Phys. **43**, 374009 (2010).
- [63] P. G. Neudeck, *SiC technology*, Tech. rep., NASA Technical Reports Server (1998).
- [64] D. J. Young, J. Du, C. A. Zorman, and W. H. Ko, *High-temperature single-crystal 3C-SiC capacitive pressure sensor*, IEEE Sens. J. **4**, 464 (2004).
- [65] H. Morkoc, S. Strite, G. B. Gao, M. Lin, B. Sverdlov, and M. Burns, *Large-band-gap SiC, III-V nitride, and II-VI ZnSe-based semiconductor device technologies*, J. Appl. Phys. **76**, 1363 (1994).
- [66] W. J. Choyke, H. Matsunami, and G. Pensl, *Silicon carbide: recent major advances*, Springer Berlin, Heidelberg, Heidelberg, 1 ed. (2004).
- [67] J. Bao, O. Yasui, W. Norimatsu, K. Matsuda, and M. Kusunoki, *Sequential control of step-bunching during graphene growth on SiC (0001)*, Appl. Phys. Lett. **109**, 081602 (2016).

- [68] A. Chatterjee, M. Kruskopf, S. Wundrack, P. Hinze, K. Pierz, R. Stosch, and H. Scherer, *Impact of Polymer-Assisted Epitaxial Graphene Growth on Various Types of SiC Substrates*, ACS Appl. Electron. Mater. **4**, 5317 (2022).
- [69] M. Kruskopf, D. M. Pakdehi, K. Pierz, S. Wundrack, R. Stosch, T. Dziomba, M. Götz, J. Baringhaus, J. Aprojanz, and C. Tegenkamp, *Comeback of epitaxial graphene for electronics: large-area growth of bilayer-free graphene on SiC*, 2D Mater. **3**, 041002 (2016).
- [70] M. Kruskopf, *Epitaxial graphene on SiC for quantum resistance metrology*, Ph.d. thesis, Physikalisch-Technische Bundesanstalt, Braunschweig, Germany (2017).
- [71] F. Ronci, S. Colonna, R. Flammini, M. De Crescenzi, M. Scarselli, M. Salvato, I. Berbezier, F. Jardim, C. Lechner, P. Pochet, H. Vach, and P. Castrucci, *High graphene permeability for room temperature silicon deposition: The role of defects*, Carbon **158**, 631 (2020).
- [72] C. Xia, L. I. Johansson, Y. Niu, A. A. Zakharov, E. Janzén, and C. Virojanadara, *High thermal stability quasi-free-standing bilayer graphene formed on 4H-SiC (0 0 0 1) via platinum intercalation*, Carbon **79**, 631 (2014).
- [73] B. V. Krsihna, S. Ravi, and M. D. Prakash, *Recent developments in graphene based field effect transistors*, Mater. Today Proc. **45**, 1524 (2021).
- [74] S. G. Chatterjee, S. Chatterjee, A. K. Ray, and A. K. Chakraborty, *Graphene-metal oxide nanohybrids for toxic gas sensor: A review*, Sensor. Actuat. B Chem. **221**, 1170 (2015).
- [75] A. F. Rigosi, C.-I. Liu, B. Y. Wu, H.-Y. Lee, M. Kruskopf, Y. Yang, H. M. Hill, J. Hu, E. G. Bittle, J. Obrzut, A. R. Hight Walker, R. E. Elmquist, and D. B. Newell, *Examining epitaxial graphene surface conductivity and quantum Hall device stability with Parylene passivation*, Microelectron. Eng. **194**, 51 (2018).
- [76] W. Pauli, *Über den Zusammenhang des Abschlusses der Elektronengruppen im Atom mit der Komplexstruktur der Spektren*, Z. Phys. **31**, 765 (1925).
- [77] F. Hund, *Zur deutung verwickelter spektren, insbesondere der elemente scandium bis nickel*, Z. Phys. **33**, 345 (1925).

- [78] C. Kittel, *Introduction to solid state physics*, John Wiley & sons, inc, Hoboken, NJ, 8 ed. (2005).
- [79] F. Weigand, *XANES und MEXAFS an magnetischen Übergangsmetalloxiden: Entwicklung eines digitalen Lock-In-XMCD-Experiments mit Phasenschieber*, Ph.d. thesis, Universität Würzburg (2003).
- [80] J. Stöhr and H. C. Siegmann, *Magnetism*, vol. 5, Springer-Verlag Berlin, Heidelberg, Heidelberg (2006).
- [81] E. C. Stoner, *Ferromagnetism*, Rep. Prog. Phys. **11**, 43 (1947).
- [82] W. Nolting, *Grundkurs theoretische physik 7: viel-teilchen-theorie (springer-lehrbuch)(german edition)*, Springer Spektrum Berlin, Heidelberg, Berlin, 8 ed. (2015).
- [83] H. Ibach, H. Lüth, H. Ibach, and H. Lüth, *Solid-State Physics: An Introduction to Principles of Materials Science*, Springer, Berlin, Heidelberg, Heidelberg (2003).
- [84] N. W. Ashcroft and N. D. Mermin, *Solid State Physics*, Holt, Rinehart and Winston, New York (1978).
- [85] R. Hoffmann, *Solids and surfaces: a chemist's view of bonding in extended structures*, Wiley-VCH, New York (1988).
- [86] P. Weiss, *L'hypothèse du champ moléculaire et la propriété ferromagnétique*, J. Phys. Theor. Appl. **6**, 661 (1907).
- [87] A. Hubert and R. Schäfer, *Magnetic Domains: The Analysis of Magnetic Microstructures*, Springer Berlin, Heidelberg, Berlin, 1 ed. (1988).
- [88] H. Ibach, *Physics of surfaces and interfaces*, vol. 12, Springer Berlin Heidelberg, Heidelberg, 1 ed. (2006).
- [89] M. T. Johnson, P. J. H. Bloemen, F. J. A. Den Broeder, and J. J. De Vries, *Magnetic anisotropy in metallic multilayers*, Rep. Prog. Phys. **59**, 1409 (1996).
- [90] T. H. R. Skyrme, *A non-linear field theory*, P. Roy. Soc. Lond. A Mat. **260**, 127 (1961).

- [91] T. H. R. Skyrme, *A unified field theory of mesons and baryons*, Nucl. Phys. **1962**, 556 (31).
- [92] J. Sampaio, V. Cros, S. Rohart, A. Thiaville, and A. Fert, *Nucleation, stability and current-induced motion of isolated magnetic skyrmions in nanostructures*, Nat. nanotechnol. **8**, 839 (2013).
- [93] S. Parkin and S.-H. Yang, *Memory on the racetrack*, Nat. nanotechnol. **10**, 195 (2015).
- [94] A. Fert, V. Cros, and J. Sampaio, *Skyrmions on the track*, Nat. nanotechnol. **8**, 152 (2013).
- [95] N. Nagaosa and Y. Tokura, *Topological properties and dynamics of magnetic skyrmions*, Nat. nanotechnol. **8**, 899 (2013).
- [96] B. Göbel, I. Mertig, and O. A. Tretiakov, *Beyond skyrmions: Review and perspectives of alternative magnetic quasiparticles*, Phys. Rep. **895**, 1 (2021).
- [97] A. N. Bogdanov and D. A. Yablonskii, *Thermodynamically stable “vortices” in magnetically ordered crystals. The mixed state of magnets*, Sov. Phys. JETP **95**, 178 (1989).
- [98] Y. A. Kharkov, O. P. Sushkov, and M. Mostovoy, *Bound states of skyrmions and merons near the Lifshitz point*, Phys. Rev. Lett. **119**, 207201 (2017).
- [99] B. Göbel, A. Mook, J. Henk, I. Mertig, and O. A. Tretiakov, *Magnetic bimerons as skyrmion analogues in in-plane magnets*, Phys. Rev. B **99**, 060407 (2019).
- [100] N. Gao, S.-G. Je, M.-Y. Im, J. W. Choi, M. Yang, Q.-c. Li, T. Y. Wang, S. Lee, H.-S. Han, K.-S. Lee, W. Chao, C. Hwang, J. Li, and Z. Q. Qiu, *Creation and annihilation of topological meron pairs in in-plane magnetized films*, Nat. Commun. **10**, 5603 (2019).
- [101] J. Xia, X. Zhang, X. Liu, Y. Zhou, and M. Ezawa, *Qubits based on merons in magnetic nanodisks*, Commun. Mater. **3**, 88 (2022).
- [102] X. Z. Yu, Y. Onose, N. Kanazawa, J. H. Park, J. H. Han, Y. Matsui, N. Nagaosa, and Y. Tokura, *Real-space observation of a two-dimensional skyrmion crystal*, Nature **465**, 901 (2010).

- [103] A. Bogdanov and A. Hubert, *Thermodynamically stable magnetic vortex states in magnetic crystals*, J. Magn. Magn. Mater. **138**, 255 (1994).
- [104] A. De Lucia, K. Litzius, B. Krüger, O. A. Tretiakov, and M. Kläui, *Multiscale simulations of topological transformations in magnetic-skyrmion spin structures*, Phys. Rev. B **96**, 020405 (2017).
- [105] T. Okubo, S. Chung, and H. Kawamura, *Multiple- q states and the skyrmion lattice of the triangular-lattice Heisenberg antiferromagnet under magnetic fields*, Phys. Rev. Lett. **108**, 017206 (2012).
- [106] T. Garel and S. Doniach, *Phase transitions with spontaneous modulation—the dipolar Ising ferromagnet*, Phys. Rev. B **26**, 325 (1982).
- [107] A. Fert and P. M. Levy, *Role of anisotropic exchange interactions in determining the properties of spin-glasses*, Phys. Rev. Lett. **44**, 1538 (1980).
- [108] A. N. Bogdanov, U. K. Roessler, M. Wolf, and K.-H. Müller, *Magnetic structures and reorientation transitions in noncentrosymmetric uniaxial antiferromagnets*, Phys. Rev. B **66**, 214410 (2002).
- [109] S. Heinze, K. Von Bergmann, M. Menzel, J. Brede, A. Kubetzka, R. Wiesendanger, G. Bihlmayer, and S. Blügel, *Spontaneous atomic-scale magnetic skyrmion lattice in two dimensions*, Nat. Phys. **7**, 713 (2011).
- [110] A. K. Nayak, V. Kumar, T. Ma, P. Werner, E. Pippel, R. Sahoo, F. Damay, U. K. Rößler, C. Felser, and S. S. P. Parkin, *Magnetic antiskyrmions above room temperature in tetragonal Heusler materials*, Nature **548**, 561 (2017).
- [111] A. Soumyanarayanan, M. Raju, A. L. Gonzalez Oyarce, A. K. Tan, M.-Y. Im, A. P. Petrović, P. Ho, K. H. Khoo, M. Tran, C. K. Gan, F. Ernult, and C. Panagopoulos, *Tunable room-temperature magnetic skyrmions in Ir/Fe/Co/Pt multilayers*, Nat. Mater. **16**, 898 (2017).
- [112] C. Moreau-Luchaire, C. Moutafis, N. Reyren, J. Sampaio, C. A. F. Vaz, N. Van Horne, K. Bouzehouane, K. Garcia, C. Deranlot, P. Warnicke, P. Wohlhüter, J.-M. George, M. Weigand, J. Raabe, V. Cros, and A. Fert, *Additive interfacial chiral interaction in multilayers for stabilization of small individual skyrmions at room temperature*, Nat. nanotechnol. **11**, 444 (2016).

- [113] R. Hönig, *Photoemission microscopy and spectroscopy of cobalt-intercalated graphene on silicon carbide*, Ph.d. thesis, TU Dortmund University, Dortmund, Germany (2019).
- [114] H. Ibach, J. D. Carette, and B. Feuerbacher, *Electron spectroscopy for surface analysis*, Springer Berlin Heidelberg, Heidelberg, 1 ed. (1977).
- [115] D. B. Williams, C. B. Carter, D. B. Williams, and C. B. Carter, *The transmission electron microscope*, Springer Science+Business Media New York / Springer, Boston, MA, Boston, MA, 1 ed. (1996).
- [116] S. Hüfner, *Photoelectron spectroscopy: principles and applications*, Springer Berlin Heidelberg, Heidelberg, 3 ed. (2003).
- [117] M. P. I. Seah and W. A. Dench, *Quantitative electron spectroscopy of surfaces: A standard data base for electron inelastic mean free paths in solids*, Surf. interface anal. **1**, 2 (1979).
- [118] H. Shinotsuka, S. Tanuma, C. J. Powell, and D. R. Penn, *Calculations of electron inelastic mean free paths. X. Data for 41 elemental solids over the 50 eV to 200 keV range with the relativistic full Penn algorithm*, Surf. interface anal. **47**, 871 (2015).
- [119] C. J. Powell, *Attenuation lengths of low-energy electrons in solids*, Surf. Sci. **44**, 29 (1974).
- [120] B. Lesiak, A. Jablonski, Z. Prussak, and P. Mrozek, *Experimental determination of the inelastic mean free path of electrons in solids*, Surf. Sci. **223**, 213 (1989).
- [121] H. Hertz, *Ueber einen Einfluss des ultravioletten Lichtes auf die elektrische Entladung*, Ann. Phys. **267**, 983 (1887).
- [122] W. Hallwachs, *Ueber den Einfluss des Lichtes auf electrostatisch geladene Körper*, Ann. Phys. **269**, 301 (1888).
- [123] P. Lenard, *Ueber die lichtelektrische Wirkung*, Ann. Phys. **313**, 149 (1902).
- [124] A. Einstein, *Über einem die Erzeugung und Verwandlung des Lichtes betreffenden heuristischen Gesichtspunkt*, Ann. Phys. **322**, 132 (1905).

-
- [125] R. A. Millikan, *A Direct Photoelectric Determination of Planck's "h"*, Phys. Rev. **7**, 355 (1916).
- [126] S. Suga, A. Sekiyama, and C. Tusche, *Photoelectron Spectroscopy: Bulk and Surface Electronic Structures*, Springer Cham, Cham, 2 ed. (2021).
- [127] W. Schattke, *PHOTOEMISSION WITHIN AND BEYOND THE ONE-STEP MODEL*, Prog. Surf. Sci. **54**, 211 (1997).
- [128] J. B. Pendry, *Theory of photoemission*, Surface Science **57**, 679 (1976).
- [129] L. Hedin, J. Michiels, and J. Inglesfield, *Transition from the adiabatic to the sudden limit in core-electron photoemission*, Phys. Rev. B **58**, 15565 (1998).
- [130] W. Demtröder, *Experimentalphysik 4*, Springer Spektrum Berlin, Heidelberg, Heidelberg, 4 ed. (2014).
- [131] P. Van der Heide, *X-ray photoelectron spectroscopy: an introduction to principles and practices*, John Wiley & Sons, Hoboken, NJ, 1 ed. (2011).
- [132] F. De Groot and A. Kotani, *Core level spectroscopy of solids*, CRC press, Boca Raton, 1 ed. (2008).
- [133] P. Auger, *Sur l'effet photoélectrique composé*, J. Phys. Paris **6**, 205 (1925).
- [134] L. Meitner, *Über die β -Strahl-Spektren und ihren Zusammenhang mit der γ -Strahlung*, Z. Phys. **11**, 35 (1922).
- [135] J. Herschel and F. William, *IV. 'Αμόρφωτα, no. I.—on a case of superficial colour presented by a homogeneous liquid internally colourless*, Philos. T. R. Soc. Lon. **135**, 143 (1845).
- [136] J. R. Lakowicz and J. R. Lakowicz, *Introduction to Fluorescence*, Springer, Boston, MA, Boston, MA, 2 ed. (1999).
- [137] M. O. Krause, *Atomic radiative and radiationless yields for K and L shells*, J. Phys. Chem. Ref. Data **8**, 307 (1979).
- [138] K. Oura, V. Lifshits, A. Saranin, A. Zotov, and M. Katayama, *Surface science: an introduction*, Springer Berlin, Heidelberg, New York, 1 ed. (2003).
-

- [139] L. Kesper, *On the structural evolution towards germanene - A photoemission study of the structural formation of a 2D material at the surface and interface*, Ph.d. thesis, TU Dortmund University, Dortmund, Germany (2022).
- [140] R. Steinhardt and E. Serfass, *X-ray photoelectron spectrometer for chemical analysis*, *Anal. Chem.* **23**, 1585 (1951).
- [141] C. Nordling, E. Sokolowski, and K. Siegbahn, *Precision method for obtaining absolute values of atomic binding energie*, *Phys. Rev.* **105**, 1676 (1957).
- [142] W. E. Spicer, *Photoemissive, photoconductive, and optical absorption studies of alkali-antimony compounds*, *Phys. Rev.* **112**, 114 (1958).
- [143] P. H. Citrin and D. R. Hamann, *Phonon broadening of x-ray photoemission line shapes in solids and its independence of hole state lifetimes*, *Phys. Rev. B* **15**, 2923 (1977).
- [144] P. Van der Heide, *X-ray photoelectron spectroscopy: an introduction to principles and practices*, John Wiley & Sons, Ltd, Hoboken, New Jersey, 10 ed. (2012).
- [145] S. Dreiner, *Untersuchung von Ober- und Grenzflächen mittels niederenergetischer Photoelektronenbeugung*, Ph.d. thesis, TU Dortmund University, Dortmund, Germany (2002).
- [146] M. Cardona and L. Ley, *Photoemission in Solids I: General Principles*, Springer Berlin Heidelberg, Berlin, Heidelberg, 1–104 (1978).
- [147] G. H. Major, N. Fairley, P. Sherwood, M. R. Linford, J. Terry, V. Fernandez, and K. Artyushkova, *Practical guide for curve fitting in x-ray photoelectron spectroscopy*, *A. Vac. Sci. Technol. A* **38** (2020).
- [148] S. Doniach and M. Sunjic, *Many-electron singularity in X-ray photoemission and X-ray line spectra from metals*, *J. Phys. C Solid State Phys.* **3**, 285 (1970).
- [149] W. Demtröder, *Experimentalphysik 3*, Springer Spektrum Berlin, Heidelberg, Heidelberg, 5 ed. (2016).
- [150] K. M. G. Siegbahn, *Photoelectron spectroscopy: retrospects and prospects*, *Philos. T. R. Soc. Lon.. S. A.* **318**, 3 (1986).

- [151] K. Siegbahn, C. Nordling, and A. Fahlman, *ESCA - Atomic, Molecular and Solid State Structure Studies by Means of Electron Spectroscopy*, Nova acta regiae societatis scientiarum Upsaliensis, Almqvist og Wiksell (1967).
- [152] R. J. Ouellette and J. D. Rawn, *Organic chemistry: structure, mechanism, synthesis*, Academic Press, Cambridge, Massachusetts, USA, 2 ed. (2018).
- [153] U. Gelius, E. Basilier, S. Svensson, T. Bergmark, and K. Siegbahn, *A high resolution ESCA instrument with X-ray monochromator for gases and solids*, J. Electron Spectrosc. **2**, 405 (1973).
- [154] NIST, *X-ray Photoelectron Spectroscopy Database, NIST Standard Reference Database 20, Ver. 4.1, Distributed by the Measurement Services Division of the National Inst. of Stand. and Techn.(NIST)*, National Institute of Standards and Technology **20** (2000).
- [155] R. Hesse, M. Weiß, R. Szargan, P. Streubel, and R. Denecke, *Improved peak-fit procedure for XPS measurements of inhomogeneous samples - Development of the advanced Tougaard background method*, J. Electron Spectrosc. **205**, 29 (2015).
- [156] D. A. Shirley, *High-Resolution X-Ray Photoemission Spectrum of the Valence Bands of Gold*, Phys. Rev. B **5**, 4709 (1972).
- [157] S. Tougaard and B. Jørgensen, *Absolute background determination in XPS*, Surf. Interface Anal. **7**, 17 (1985).
- [158] R. Hesse, M. Weiß, R. Szargan, P. Streubel, and R. Denecke, *Comparative study of the modelling of the spectral background of photoelectron spectra with the Shirley and improved Tougaard methods*, J. Electron Spectrosc. **186**, 44 (2013).
- [159] J. Végh, *The Shirley background revised*, J. Electron Spectrosc. **151**, 159 (2006).
- [160] J. A. Hochhaus and N. Hideki, *LG4X-V2 (V2.1.2)* (Aug. 2023).
- [161] B. Singh, R. Hesse, and M. R. Linford, *Good practices for XPS (and other types of) peak fitting*, Vac. Technol. Coat. **12**, 25 (2015).

- [162] D. W. Marquardt, *An algorithm for least-squares estimation of nonlinear parameters*, J. Soc. Ind. Appl. Math. **11**, 431 (1963).
- [163] M. Rocca, T. S. Rahman, and L. Vattuone, *Springer Handbook of Surface Science*, Springer Cham, Cham, 1 ed. (2020).
- [164] C. Keutner, *Der direkte Blick auf die Magnetosomen-Kette: PEEM- und SEM-Untersuchungen am intakten Magnetospirillum magnetotacticum*, Ph.d. thesis, TU Dortmund University (2015).
- [165] F. Roccaforte, F. Giannazzo, and V. Raineri, *Nanoscale transport properties at silicon carbide interfaces*, J. Phys. D Appl. Phys. **43**, 223001 (2010).
- [166] C.-H. Kuo, C.-P. Liu, S.-H. Lee, H.-Y. Chang, W.-C. Lin, Y.-W. You, H.-Y. Liao, and J.-J. Shyue, *Effect of surface chemical composition on the work function of silicon substrates modified by binary self-assembled monolayers*, Phys. Chem. Chem. Phys. **13**, 15122 (2011).
- [167] G. Schönhense, *Imaging of magnetic structures by photoemission electron microscopy*, J. Phys. Condens. Matter **11**, 9517 (1999).
- [168] J. Stöhr and S. Anders, *X-ray spectro-microscopy of complex materials and surfaces*, IBM Journal of Research and Development **44**, 535 (2000).
- [169] W. Gudat and C. Kunz, *Close similarity between photoelectric yield and photoabsorption spectra in the soft-x-ray range*, Phys. Rev. Lett. **29**, 169 (1972).
- [170] W. Swiech, G. Fecher, C. Ziethen, O. Schmidt, G. Schönhense, K. Grzelakowski, C. M. Schneider, R. Frömter, H. Oepen, and J. Kirschner, *Recent progress in photoemission microscopy with emphasis on chemical and magnetic sensitivity*, J. Electron Spectrosc. **84**, 171 (1997).
- [171] W. Kuch, R. Schäfer, P. Fischer, and F. U. Hillebrecht, *Magnetic Microscopy of Layered Structures*, Springer-Verlag Berlin, Heidelberg, Heidelberg, 1 ed. (2015).
- [172] U. Fano, *Spin orientation of photoelectrons ejected by circularly polarized light*, Phys. Rev. **178**, 131 (1969).

- [173] G. Schütz, W. Wagner, W. Wilhelm, P. Kienle, R. Zeller, R. Frahm, and G. Materlik, *Absorption of circularly polarized x rays in iron*, Phys. Rev. Lett. **58**, 737 (1987).
- [174] A. Scherz, *Spin-dependent X-ray Absorption Spectroscopy of 3d Transition Metals: Systematics and Applications*, Ph.d. thesis, Universität Berlin (2003).
- [175] W. Kuch, R. Schäfer, P. Fischer, and F. U. Hillebrecht, *Magnetic Microscopy of Layered Structures*, Springer-Verlag Berlin, Heidelberg, Heidelberg, 1 ed. (2014).
- [176] L. de Broglie, *XXXV. A tentative theory of light quanta*, Lond. Edinb. Dub. Philos. Mag. J. Sci. **47**, 446 (1924).
- [177] C. Davisson and L. H. Germer, *Diffraction of electrons by a crystal of nickel*, Phys. Rev. **30**, 705 (1927).
- [178] M. A. VanHove, W. H. Weinberg, and C.-M. Chan, *Low-energy electron diffraction: experiment, theory and surface structure determination*, vol. 6, Springer Berlin, Heidelberg, Berlin, 1 ed. (2012).
- [179] H. Schulz, *Elektronen und Oberflächen: Low Energy Electrons and Surface Chemistry. Von G. Ertl und J. Küppers. VCH Verlagsgesellschaft, Weinheim-Deerfield Beach, FL/USA 1985. XII. 374 S., 257 Abb., 15 Tab., DM 168,-. ISBN 3-527-26056-0* (1987).
- [180] M. Henzler and W. Göpel, *Oberflächenphysik des Festkörpers*, Vieweg+Teubner Verlag Wiesbaden, Stuttgart, 2 ed. (1991).
- [181] C. Hilscher, *Großflächiges Wachstum von Graphen auf SiC(0001)-6H*, Master's thesis, TU Dortmund University (2015).
- [182] E. J. Davies and T. Barker, *Conduction and induction heating*, Peter Peregrinus, London (1991).
- [183] M. L. Wang, J. P. Lynch, and H. Sohn, *Sensor technologies for civil infrastructures Volume 2: Applications in Structural Health Monitoring*, Elsevier, 2 ed. (2014).

- [184] G. F. Rempfer, *Unipotential electrostatic lenses: Paraxial properties and aberrations of focal length and focal point*, J. Appl. Phys. **57**, 2385 (1985).
- [185] R. Hönig, *Charakterisierung von Graphen auf 6H-SiC(0001) mittels PEEM und XPS*, Master's thesis, TU Dortmund University, Dortmund, Germany (2019).
- [186] T. Fauster, L. Hammer, K. Heinz, and M. A. Schneider, *Oberflächenphysik: Grundlagen und Methoden*, Oldenbourg Wissenschaftsverlag, München (2019).
- [187] SPECS GmbH, Berlin, Germany, *ErLEED Optics and Power Supplies*, 1.3 ed. (2003).
- [188] C. Westphal, U. Berges, S. Dreiner, R. Follath, M. Krause, S. F. D. Schirmer, and M. Schürmann, *The plane-grating monochromator beamline at the U55 undulator for surface and interface studies at DELTA*, J. Electron Spectrosc. **144-147**, 1117 (2005).
- [189] S. Mobilio, F. Boscherini, and C. Meneghini, *Synchrotron Radiation: Basics, Methods and Applications*, Springer Berlin, Heidelberg, Heidelberg, 1 ed. (2015).
- [190] J. Osterwalder, M. Sagurton, P. J. Orders, C. S. Fadley, B. D. Hermsmeier, and D. J. Friedman, *Electron trajectory analysis of the spherical-sector electrostatic spectrometer: focussing properties and multichannel detection capability*, J. Electron Spectrosc. **48**, 55 (1989).
- [191] S. Hüfner, *Photoelectron spectroscopy: principles and applications*, Springer Berlin, Heidelberg, New York, 3 ed. (2003).
- [192] H. Sjuts, *Channel Electron Multipliers Series KBL & Complete Measurement Systems*, http://www.sjuts.com/index_english.html (2022), retrieved: 2022-09-28.
- [193] A. G. Shard and B. P. Reed, *Al K α XPS reference spectra of polyethylene for all instrument geometries*, A. Vac. Sci. Technol. A **38**, 063209 (2020).
- [194] F. Kronast and S. V. Molina, *SPEEM: The photoemission microscope at the dedicated microfocussing PGM beamline UE49-PGMa at BESSY II*, Journal of large-scale research facilities JLSRF **2**, A90 (2016).

-
- [195] *ELMITEC Elektronenmikroskopie GmbH*, <https://elmitec.de/index.php> (2023), retrieved: 2023-09-26.
- [196] S. Dhar, O. Seitz, M. D. Halls, S. Choi, Y. J. Chabal, and L. C. Feldman, *Chemical properties of oxidized silicon carbide surfaces upon etching in hydrofluoric acid*, Am. Chem. Soc. **131**, 16808 (2009).
- [197] H. Kromer, *Epitaktisches Wachstum von Graphen mittels der CCS-Methode*, Master's thesis, TU Dortmund University (2016).
- [198] M. Kruskopf, A. F. Rigosi, A. R. Panna, M. Marzano, D. Patel, H. Jin, D. B. Newell, and R. E. Elmquist, *Next-generation crossover-free quantum Hall arrays with superconducting interconnections*, Metrologia **56**, 065002 (2019).
- [199] M. Gianfelice, *Untersuchung des Rekonstruktionsverhaltens von gestuftem 4H-SiC(0001) mittels Rasterkraftmikroskopie*, Master's thesis, TU Dortmund University (2017).
- [200] R. C. of America Laboratories, *Vapor pressure data for the more common elements*, Tech. rep., RCA laboratories, Industry Service Laboratory (1957).
- [201] G. L. Selman, *The Platinum-Molybdenum System*, Platin. Met. Rev. **11**, 132 (1967).
- [202] E. D. Olsen, R. F. Eakin, and W. J. Blaedel, *Using tantalum and platinum-clad tantalum electrodes for depositions*, J. Chem. Educ. **40**, 320 (1963).
- [203] A. G. Knapton, *Alloys of platinum and tungsten*, Platin. Met. Rev. **24**, 64 (1980).
- [204] P. D. Mehring, *SAMs organischer Halbleiter auf Au-Substraten - Eine STM-Untersuchung*, Ph.d. thesis, TU Dortmund University, Dortmund, Germany (2013).
- [205] G. Sauerbrey, *Verwendung von Schwingquarzen zur Wägung dünner Schichten und zur Mikrowägung*, Z. Phys. **155**, 206 (1959).
- [206] S. Mammadov, J. Ristein, J. Krone, C. Raidel, M. Wanke, V. Wiesmann, F. Speck, and T. Seyller, *Work function of graphene multilayers on SiC (0001)*, 2D Mater. **4**, 015043 (2017).

- [207] R. Yu, H. Song, X.-F. Zhang, and P. Yang, *Thermal wetting of platinum nanocrystals on silica surface*, J. Phys. Chem. B **109**, 6940 (2005).
- [208] Z. L. Wang, J. M. Petroski, T. C. Green, and M. A. El-Sayed, *Shape transformation and surface melting of cubic and tetrahedral platinum nanocrystals*, J. Phys. Chem. B **102**, 6145 (1998).
- [209] T. Nishizawa and K. Ishida, *The Co (cobalt) system*, Bull. Alloy Phase Diagr. **4**, 387 (1983).
- [210] V. Panchal, Y. Yang, G. Cheng, J. Hu, M. Kruskopf, C.-I. Liu, A. F. Rigosi, C. Melios, A. R. Walker Hight, D. B. Newell, O. Kazakova, and R. E. Elmquist, *Confocal laser scanning microscopy: A tool for rapid optical characterization of 2D materials*, arXiv:1804.04420 (2018).
- [211] A. Herrera-Gomez, M. Bravo-Sanchez, F. Aguirre-Tostado, and M. Vazquez-Lepe, *The slope-background for the near-peak regimen of photoemission spectra*, J. Electron spectrosc. **189**, 76 (2013).
- [212] B. H. Armstrong, *Spectrum line profiles: the Voigt function*, J. Quant. Spectrosc. Radiat. Transfer **7**, 61 (1967).
- [213] C. Virojanadara, S. Watcharinyanon, A. A. Zakharov, and L. I. Johansson, *Epitaxial graphene on 6H-SiC and Li intercalation*, Phys. Rev. B **82**, 205402 (2010).
- [214] C. Xia, S. Watcharinyanon, A. A. Zakharov, R. Yakimova, L. Hultman, L. I. Johansson, and C. Virojanadara, *Si intercalation/deintercalation of graphene on 6H-SiC(0001)*, Phys. Rev. B **85**, 045418 (2012).
- [215] J. A. Gardella, S. A. Ferguson, and R. L. Chin, *$\pi^* \leftarrow \pi$ shakeup satellites for the analysis of structure and bonding in aromatic polymers by X-ray photoelectron spectroscopy*, Appl. spectrosc. **40**, 224 (1986).
- [216] P. S. Bagus, E. S. Ilton, and C. J. Nelin, *The interpretation of XPS spectra: Insights into materials properties*, Surf. Sci. Rep. **68**, 273 (2013).

- [217] E. Malis and M. Vargas Villanueva, *Deeper understanding of the homography decomposition for vision-based control*, [Research Report] **RR-6303, INRIA., inria-00174036v3** (2007).
- [218] I. Gierz, T. Suzuki, R. T. Weitz, D. S. Lee, B. Krauss, C. Riedl, H. Starke, U. S. H. J. H, and C. R. Ast, *Electronic decoupling of an epitaxial graphene monolayer by gold intercalation*, *Phys. Rev. B* **81**, 235408 (2010).
- [219] C. V. Thompson, *Solid-state dewetting of thin films*, *Annu. Rev. Mater. Res.* **42**, 399 (2012).
- [220] J. Cho, N.-H. Kim, S. Lee, J.-S. Kim, R. Lavrijsen, A. Solignac, Y. Yin, D.-S. Han, N. J. J. Van Hoof, H. J. M. Swagten, B. Koopmans, and C.-Y. You, *Thickness dependence of the interfacial Dzyaloshinskii–Moriya interaction in inversion symmetry broken systems*, *Nat. Commun.* **6**, 7635 (2015).
- [221] W.-S. Wei, Z.-D. He, Z. Qu, and H.-F. Du, *Dzyaloshinsky–Moriya interaction (DMI)-induced magnetic skyrmion materials*, *Rare Metals* **40**, 3076 (2021).
- [222] H.-B. Braun, *Topological effects in nanomagnetism: from superparamagnetism to chiral quantum solitons*, *Adv. Phys.* **61**, 1 (2012).
- [223] R. T. Fryer and R. J. Lad, *Synthesis and thermal stability of Pt₃Si, Pt₂Si, and PtSi films grown by e-beam co-evaporation*, *J. Alloy. Compd.* **682**, 216 (2016).

Appendix

Publications

Article

- Philipp Weinert, Julian A. Hochhaus, Lukas Kesper, Robert Appel, Stefanie Hilgers, Marie Schmitz, Malte G. H. Schulte, Richar Hönig, Florian Kronast, Sergio Valencia, Mattias Kruskopf, Atasi Chatterjee, Ulf Berges, and Carsten Westphal, *Structural, chemical, and magnetic investigation of a graphene/cobalt/platinum multilayer system on silicon carbide*, Nanotechnology, Accepted Manuscript (Status: Jan. 11, 2024).

Conference Talks and Presentations

1. Philipp Weinert, Richar Hönig, Peter Rose, Karim Shamout, Ulf Berges, and Carsten Westphal, *Intercalation of silver and gold between graphene and silicon carbide*, 14th DELTA User Meeting, Dortmund, Germany (2018).
2. Philipp Weinert, Richar Hönig, Ulf Berges, and Carsten Westphal, *Intercalation of silver between graphene and silicon carbide studied by PEEM and AFM*, DPG Spring-Meeting 2019, Regensburg, Germany (2019).
3. Philipp Weinert, Lukas Kesper, Julian A. Hochhaus, Ulf Berges, and Carsten Westphal, *Chemical investigation a of graphene/cobalt/platinum multilayer system on silicon carbide*, 17th DELTA User Meeting, Dortmund, Germany (2021).

4. Philipp Weinert, Lukas Kesper, Malte G. H. Schulte, Marie Schmitz, Sergio Valencia, Florian Kronast, Ulf Berges, and Carsten Westphal, *Microscopic investigation of the magnetic anisotropy in a graphene/cobalt/platinum multilayer system on silicon carbide*, HZB User Meeting 2022, Berlin, Germany (2022).
5. Philipp Weinert, Lukas Kesper, Julian A. Hochhaus, Robert Appel, Malte G. H. Schulte, Marie Schmitz, Stefanie Hilgers, Sergio Valencia, Florian Kronast, Mattias Kruskopf, Atasi Chatterjee, Ulf Berges, and Carsten Westphal, *Structural, chemical, and magnetic investigation of a graphene/cobalt/platinum multilayer system on silicon carbide*, Magnetism 2022, York, England (2022).

Appendix

Danksagung

Zum Schluss dieser Arbeit möchte ich einigen Personen danken, die mich wesentlich in den letzten Jahren unterstützt und begleitet haben.

Als Erstes danke ich Herrn Prof. Dr. Carsten Westphal für die wertvolle und angenehme Betreuung dieser Dissertation sowie für die Möglichkeit der Arbeit in seiner Gruppe mit der großen gebündelten Fachkompetenz und der nötigen Infrastruktur. Die vielen Gespräche auf fachlicher und nicht fachlicher Ebene waren immer wieder hilfreich und motivierend. Seine stetige Bereitschaft zur Unterstützung auf vielen verschiedenen Ebenen hat einen wesentlichen Anteil am erfolgreichen Abschluss dieser Arbeit.

Ebenso bedanke ich mich sehr bei Herrn Prof. Dr. Dr. Wolfgang Rhode für seine Bereitschaft, das Zweitgutachten für diese Arbeit zu übernehmen.

Der bereits erwähnten AG Westphal möchte ich nochmal einen besonderen Dank aussprechen. Die sehr gute Atmosphäre und viele gegenseitige Unterstützung durch alle Mitglieder der Gruppe haben das Arbeiten angenehm und produktiv gemacht. Insbesondere möchte ich Herrn Dr. Richard Hönig dafür danken, mich zu Beginn meiner Arbeit umfangreich und vielfältig an die Aufgaben meiner Arbeit herangeführt zu haben. Für die Mitarbeit während der externen Messwochen bei BESSY II, mit der besonders intensiven und hohen Arbeitslast, möchte ich mich bei Dr. Marie Schmitz, Dr. Malte Schulte, Dr. Lukas Kesper, Julian Hochhaus, Robert Appel und Stefanie Hilgers bedanken. Diese spezifische Unterstützung hat es erst möglich gemacht, einige der aufwändigen finalen Messungen an dem zuvor lange vorbereiteten System durchzuführen.

Weiter möchte ich mich bei Marius Alt, Julian Hochhaus und Stefanie Hilgers für das hervorragende Lektorat dieser Arbeit besonders bedanken.

Den Mitarbeitern von DELTA danke ich für den guten Betrieb und die stetige Beachtung der Wünsche von uns Nutzern. Für die gute und freundliche Zusammenarbeit hinsichtlich der Probenpräparation danke ich Frau Dr. Atasi Chatterjee und Herrn Dr. Mattias Kruskopf von der Physikalisch-Technische Bundesanstalt (PTB). Für die Bereitstellung der Infrastruktur für alle X-PEEM Messungen danke ich den Mitarbeitern der Berliner Elektronenspeicherring-Gesellschaft für Synchrotronstrahlung II (BESSY II) des Helmholtz-Zentrum Berlin (HZB). Besonders danke ich an dieser Stelle auch Herrn Dr. Florian Kronast und Herrn Dr. Sergio Valencia Molina für die Einarbeitung an ihrem Aufbau und die Unterstützung während der Messungen und Auswertung.

Zuletzt möchte ich mich besonders herzlich bei meiner Familie und meinen Freunden bedanken, die mir immer zur Seite standen, mich entlasteten und motivierten und so auch wesentlich zum Erfolg dieser Arbeit beitrugen.

Vielen Dank für all die vielfältige Unterstützung!